BORE IMPACT UPON VERTICAL WALL AND WATER-DRIVEN, HIGH-MASS, LOW-VELOCITY DEBRIS IMPACT

A DISSERTATION SUBMITTED TO THE GRADUATE DIVISION OF THE UNIVERSITY OF HAWAI`I IN PARTIAL FULFILLMENT OF THE REQUIREMENTS FOR THE DEGREE OF

DOCTOR OF PHILOSOPHY

IN

CIVIL ENGINEERING

DECEMBER 2011

by

Krystian Paczkowski

Dissertation Committee:

H. Ronald Riggs, Chairperson
Ian Robertson
David T. Ma
Marcelo Kobayashi
Kwok Fai Cheung

Acknowledgments

I would like to express my sincere gratitude to my advisor Professor H. Ronald Riggs for his continuous interest, support, guidance, and constructive criticism during this study. Without his help this study would not have been possible.

I appreciate the helpful suggestions and time of the members of my dissertation committee, Professors Ian N. Robertson, Marcelo H. Kobayashi, Kwok Fai Cheung, and David Ma.

I am also indebted to my colleagues, Volker Roeber, Abdulla Mohamed, Pablo Duarte Quiroga, and Jillian Santo for the help with data collection, valuable advice, and suggestions.

Finally, I would like to thank my family, especially my parents for their continuous support during last 6 years. Also I would like to thank my dear friends Steve and Monika Ward and Yoshi and Paula Takei. For all the countless ways you have helped and supported me, thank you!

The financial support provided by the Network for Earthquake Engineering Simulations (NEES) is gratefully acknowledged (grants #0530759 and CMMI-1041666).

Abstract

This dissertation proposes a method to predict the peak lateral force on a vertical wall from an impacting bore. The formula has been developed based on the analysis of data from large-scale experimental tests on bore impact. The lateral forces are much larger than traditional lateral loads on vertical walls. It is shown, the data indicate that the formula can be used for prototype scale following Froude scaling. Additionally, a computational tsunami bore generation study utilizing the Reynolds Average Navier-Stokes equations is presented. Three bore generating scenarios are reviewed and results are presented, providing guidance on how best to generate bores for further numerical studies.

In the latter part of the dissertation, the application of a simple one-dimensional model to obtain impact force magnitude and duration, based on acoustic wave propagation in a flexible projectile, is explored. The focus herein is on in-air impact. Based on small-scale experiments, the applicability of the model to predict actual impact forces is investigated. The tests show that the force and duration are reasonably well represented by the simple model, but they also show how actual impact differs from the ideal model. The one-dimensional model is extended to consider water-driven debris as well. When fluid is used to propel the 1-D model, an estimate of the 'added mass' effect is possible. In this extended model the debris impact force depends on the wave propagation in the two media, and the conditions under which the fluid increases the impact force are discussed. The results indicate that the model provides an accurate estimation of the peak impact force and its duration. For the tested scenario, the maximum impact force does not depend on the total mass of the debris.

Table of Contents

List of Tables

List of Figures

Chapter 1

Introduction

1.1 Background

Tsunami is a set of waves mostly caused by earthquake, underwater volcanic explosion, underwater landslides or a combination of those events. These phenomena can cause a massive shift and a vertical motion of the seabed, which results in a large volume of oceanic water being pushed in a vertical motion. The tsunami wave consists of a very large volume of water in motion with a low amplitude and long wavelength spanning up to several hundred kilometers. The tsunami wave speed in open water depends on the water depth and is often between 500 and 1000 km/h (310 to 620 mph). Because of the low amplitude in the open ocean, the waves are often not noticed by ship or airplane observations. When approaching sloping coastal areas, the amplitude increases as a result of shoaling. The large wave heights can create strong, damaging bores affecting land areas. Such bores have velocities on the order of meters per second, where impinging water appears as highly turbulent flow with high celerities [1, 2].

Numerous tsunamis have occurred throughout history, many resulting in catastrophic losses. One of the earliest recorded tsunamis dates back to the time of Alexander the Great and occurred in the North Arabian Sea in 325 B.C. Following historical resources, one of the most lethal tsunamis occurred in Lisbon, Portugal on November 1, 1755, killing approximately 90,000 people [3-5]. Another occurred in Indonesia on August 27, 1883, killing 36,000 people [6, 7] and in Japan, along the Sanriku coast on June 15, 1896, 27,000 people died and 10,000 buildings were destroyed by a tsunami [8]. In 1958, a very dramatic tsunami was generated by a landslide in the Alaskan Lituya Bay [9], where a 50 m wave was generated and ran up 525 m inside the bay valley. On May 23, 1960, a catastrophic tsunami struck Hilo on the island of Hawaii. Destructive waves caused significant damage to a large part of the business district, including 229 dwellings and 308 business buildings [1, 2], in which the loss was estimated at $20,000,000. On March 28, 1964, in Alaska, the destructive force of a tsunami resulted in 119 casualties and

$11,000,000 loss in overall damage [10]. Hawaii and the west coast of the United States were also affected. In more recent years, on September 2, 1992, another tsunami occurred off the coast of Nicaragua [11], causing significant damage along 220 km of shoreline. The tsunami noted in history as the most deadly occurred in the Indian Ocean, December 26, 2004, which resulted in more than 200,000 lives lost [12, 13] and covered many of the local islands with water. In Samoa, on September 30, 2009, a tsunami killed about 200 people and destroyed a significant amount of civil structures [14]. Shortly after, another tsunami, which caused significant damage, was generated along the coast of Chile, February 27, 2010. A very recent tsunami occurred in Japan along the coast of Tohoku, March 11, 2011. These few examples represent only a small fraction of all tsunami occurrences in the world.

These examples illustrate that tsunami is a real threat. Tsunami generating mechanisms happen several times a year. Recent research [15] showed many coastal areas are not prepared and sufficiently protected. Many communities are without sufficient evacuation routes. In such communities, it is important to have civil structures that can serve as safe evacuation sites. Recent events in the Pacific Ocean showed many hi-rise buildings, such as hotels, served as protection and evacuation points. None of these buildings were designed to accommodate such extreme loading from impinging masses of water. Most of these survived by chance, rather than by intentional structural design.

There is significant amount of work regarding wave impact on offshore structures, such as ocean platforms and piers [16-24]. However, there is little research on the effects of tsunami loading on buildings, bridges, and harbors including inland structures [15]. Herein, the flow resulting from a tsunami wave breaking will be referred to as a bore flow, because of its bore-like resemblance. One might argue the description is not very precise; however, because of its flow nature and characteristics it is widely used in the literature [10, 20, 25-29].

The fluid forces acting on structures include hydrostatic and hydrodynamic effects. Which kind of force is significant depends on the structure alignment, whether it is vertical or horizontal, submerged or above the water surface, and whether the highest

impact force is caused by the leading front of the water or by continuous water flow. Another interesting circumstance for consideration is the effect of floating debris, which can be transported by the bore. Such effects might change structural loading conditions dramatically.

The primary focus of the work herein is on three aspects:

- experimental bore flow analysis and its impact upon a vertical wall
- computational fluid dynamic modeling of tsunami impact forces
- development of design equations for tsunami forces on structures, including floating debris impact.

The goal is to broaden the understanding of interaction between the bore and the structures and have better insight into resulting structural forces from bore action and structural debris impact.

1.2 Outline

Chapter 2 presents a literature review of existing approaches, which provide different methods for fluid and debris impact force calculation. The chapter mainly focuses on the forces generated from tsunami or storm surge, as well as forces resulting from big waves on offshore structures, such as platforms, including horizontal members. Impact of floating debris on structures is also described. Chapter 3 provides an overview of a series of experiments, carried out by others, to quantify tsunami bore forces on vertical structures. Data include forces on and pressure distribution along a vertical wall. Based on these data, a design formula for maximum impact force is proposed and compared to existing approaches. Chapter 4 describes a numerical approach to estimate tsunami impact force utilizing Computational Fluid Dynamics. Different bore formation methods are described, results are presented, and a guideline for design of computational models is provided. In Chapter 5, an experimental setup for debris impact is introduced and a set of tests is described. A mathematical model for fluid driven debris impact upon structures is proposed. Chapter 6 summarizes equations proposed herein and provides conclusions of the study, outlining future research needs.

Chapter 2

Literature review

2.1 Overview

The literature provides relatively little information about tsunami wave forces acting on structural elements. However, there is a number of scientific publications related to ocean wave action on horizontal and vertical members in ocean structures. Particular attention has been given to forces acting on marine platforms exposed to large wave loads. In this section, tsunami wave characteristics and fluid impact upon structural elements are reviewed. Approaches that define wave loads on coastal and offshore constructions are described including also those that result from floating debris.

2.2 Tsunami bore development and generated structural forces

Focusing on tsunami references, Fukui et al. [27] is one of the first published papers describing the physics of tsunami that includes detailed theoretical explanation of tsunami waves, their characteristics, and conditions of creation. The authors conducted experimental analysis of tsunami action upon dikes. As a result, data to design dikes against tsunamis were obtained. Fukui explains that the broken onshore tsunami flow behaves as a progressive breaker wave, which resembles the behavior and shape of a bore. The paper states that after the wave breaks, the bore development most likely depends on the wave amplitude, reverse flow presence, and bed gradient changes. However, no clear explanation was provided that sufficiently describes the criterion of bore formation.

Wilson et al. [10] used the method of characteristics to estimate the bore velocity for the dry-bed condition as

$$u \approx 2\sqrt{g\,h} \tag{2.1}$$

where u is the velocity, g is the gravitational acceleration, and h is the bore elevation advancing on the dry bed. For the case with initial standing water,

$$u = \sqrt{gh}[(1 + d/h)(1 + h/2d)]^{1/2} \quad (2.2)$$

in which h is the bore height advancing into still water depth d. If $h = 6d$, then equation (2.2) is approximately the same as equation (2.1) i.e., equation (2.2) becomes $2.16\sqrt{g\,h}$.

Regarding the forces acting on structures, Reese and Matlock [1] provided an equation where the force magnitude is defined through fluid drag necessary to cause structural wall failure experienced during the 1960 Chilean tsunami, i.e.,

$$F = \frac{1}{2} C_d\, \rho\, A\, u^2 \quad (2.3)$$

which is the basic equation for drag force, where C_d is the drag coefficient, ρ is the density, and A is the impact surface area Bh, in which B is the structural width and h defines the flow depth. In the approach, it is assumed the calculated load is uniformly distributed throughout the depth required to cause the structural damage. A similar approach was used in [16, 30, 31]. Wilson [10] states that equation (2.3) is only valid if the structure is fully enveloped in the water flow. Hence, this approach may be most applicable to small objects. In the case of large structures, such as retaining walls and buildings under the influence of cascading water, a combined effect of hydrostatic and dynamic pressures should be taken into account.

Ramsden et al. [28, 29] obtained experimental forces resulting from broken solitary waves on a sloping beach [29] and bores traveling on top of a horizontal dry-bed impacting a vertical wall [28]. Solitary waves were generated with a hydraulic piston actuator. Bores and surges were created using a dam break setup with a pneumatic gate to create a water volume reservoir. The forces associated with bores generated from broken solitary wave were investigated in a 1/50 tilted wave tank. Based on [29] it was proposed that the highest forces on the wall occurs during reflection of a bore and could be approximated by the hydrostatic force. An empirical equation was obtained as a prediction for the maximum force on a vertical wall due to a bore impact. For all the experiments, the calculated force from maximum measured run-up on the structure (with assumed hydrostatic conditions) overestimated measured values.

Árnason [25] carried out a series of dam break experiments similar to [28, 29], in which the tsunami bore was traveling on dry-bed. The experimental setup involved a pneumatically operated gate retaining a water reservoir. Opening the gate generated water flow. Instrumented obstacles included cylindrical and square columns. To calculate the net hydrostatic force acting on a column, Árnason used the difference between force magnitude on the upstream and downstream face of the instrumented column. The calculated hydrostatic forces were compared to experimental force measurements.

Riggs et al. [32] described a project on tsunami effects on coastal areas. The goal was to develop the methodology and simulation tools for analysis and design of coastal structures. The project focused on three main aspects: run-up and inundation (including fluid velocities), sediment transport and soil scour, and fluid loading on structural elements. All the experiments were conducted at the O.H. Hinsdale Wave Research Laboratory [33] of Oregon State University (OSU), which included the Tsunami Wave Basin (TWB) facility as a part of the NSF Network for Earthquake Engineering Simulation (NEES). The TWB used piston type wave boards that can generate solitary waves, which were used to model tsunami waves. All the structural tests were performed with different solitary wave heights, where broken waves formed a turbulent bore, which always occurred in the transition area between the beach slope and the horizontal reef. Generated bores resembled well the broken tsunami wave conditions.

A Federal Emergency Management Agency (FEMA) guideline [26] provides guidance on tsunami force effects on vertical structural elements encountered in coastal structures. The guideline provides information on what forces should be considered in structural design, such as hydrostatic, buoyant, hydrodynamic, impulsive, debris impact, debris damming, uplift, and floor-retained water forces. All the described forces are based on post wave-break conditions, where the tsunami wave broke offshore and translates inland as surge or bore flow. Most of the equations can be found in more detail in the papers reviewed in other parts of this literature review. The document also introduced *impulse force*, which is described as the force caused by the leading edge of the tsunami bore as it impinges a structure. Based upon the experiments from [25, 28, 29], a comparison between dry-bed and initially flooded surges was made. The overshoot in

the force was observed and was found to be around 1.5. Therefore, for conservatism, the proposed impulsive force is based upon hydrodynamic force multiplied by an overshoot factor, i.e.,

$$F_s = 1.5\, F_d \,. \tag{2.4}$$

in which F_s is the impulsive force and F_d is the hydrodynamic force defined by equation (2.3). In equation (2.4), with equation (2.3), the momentum flux component is defined as $(hu^2)_{max}$. It should be noted that the maximum flow depth h_{max} and maximum flow velocity u_{max} at a site do not occur at the same time. The guideline also considers uplift forces on the elevated floors, where such forces are introduced when building floor levels are submerged.

In the literature, the fluid forces are separated into two categories, the horizontal and vertical forces. These will be further explained in the next two sections.

2.3 Horizontal member forces

This section reviews work on vertically acting forces on horizontal members.

One of the first works to provide the wave uplift force on a horizontal plate structure was published by French [20]. A wave generator in a narrow 610 mm channel created a solitary wave. The wave forces were generated upon a simplified test platform with an extended vertical face to prevent wave overtopping. A major part of the report described experimental aspects of the flow and the short duration pressure phenomena upon impact. A formula for the pressure was developed. The test setup involved a rigid horizontal plate with a traveling wave underneath the structure. This, however, does not represent well the tsunami wave conditions observed in coastal communities.

Wang [24] mentioned shoaling effects on wave-induced uplift pressures. In regard to tsunami waves, such effects have a large influence on flow formation, which results in strong bore creation. Waves while moving into shallow depth decrease in length and speed. The height of the wave initially decreases and then increases, resulting in wave breaking. Wang describes that when the wave enters a shallower water area, the shape of the wave becomes asymmetric.

Broughton and Horn [17] estimated the Ekofisk platform deck wave forces using a simple theoretical procedure. The prediction of the force impingement was based upon change in momentum at the time when the wave crest impacts the structure. Both horizontal and vertical force formulae were proposed, in which the squared velocity component of the momentum was defined as a combination of incident wave celerity c and water particle velocity u, such as $u \cdot c$.

Kaplan [21] introduced new mathematical models to determine the time histories of impact force on horizontal circular members and flat deck structures in offshore platforms. The proposed approach considered hydrodynamic inertial forces with the contribution of buoyancy and drag forces. The overall force on the flat rectangular plate was written as combined momentum with drag forces. The equation assumed a traveling wave crest inundated the deck, where the deck location exceeds the mean water level (MWL). Kaplan presented force as a function of time during the period of wave action. The vertical force was found for a theoretical sine wave. Additional considerations can be found in [34]. The theoretical vertical forces on a flat plate have not been verified by comparison to experimental data. In [22], Kaplan also introduced theoretical force analysis for the offshore platform deck subjected to a large incident wave. The force definition directly references to [21]. Similar to that paper, the approach is two-dimensional, but modified to include the effects of plate aspect ratios. The formulation combines momentum and drag forces.

Shih and Anastasiou [23] described a laboratory study of wave uplift forces on platform decks in shallow waters. Small and large flumes were used in their experiment. The experiment revealed that there was a large air entrainment underneath the platform deck. Therefore, the air strongly influences the fluid motion and ultimately force measurements. It was observed that the duration and the pressures during the impact were also highly governed by air, where the duration of the force increases with higher air entrainment. The authors pointed out a great variability in results and noticed that duration of the impact increased with increased air entrainment and the Froude scaling did not apply.

Bea et al. [16] introduced a formulation for the overall force acting on a deck structure consisting of buoyancy, slamming, drag, uplift, and inertia components. When the structure becomes submerged, the buoyancy, drag, and inertia forces are the only relevant components. Bea et al. [16] pointed out that the upward and downward deck forces can exceed the horizontal force. It should be noted that at the maximum drag force action (maximum horizontal velocity at the wave crest) the inertia force (acceleration at wave crest) is near zero. The authors defined hydrodynamic horizontal force as a drag force, similar to equation (2.3). A similar approach was used in [16, 26, 30, 31].

Douglas et al. [19] introduced a method to estimate wave loads on typical elevated U.S. bridges under storm wave conditions. Force formulations were introduced for horizontal and vertical forces. The authors note specific case-dependent design equations should be developed following comprehensive experimental tests, which will include different bridge configurations.

McPherson [35] is an extension of Douglas et al. [19] with overall structural forces separated into: hydrostatic force on top of the bridge, overall buoyancy of the bridge, and the buoyancy forces in between bridge girders resulting from entrapped pockets of air. The approach provided an improved force estimate compared to previously existing methods [16, 19, 21, 22].

An AASHTO [36] guideline provides a quasi-static vertical force formula, which is based on a numerical study. The maximum force acting on a bridge section with girders depends on the wave height, length, and period and its height above storm water level as well as storm water depth.

Cuomo et al. [18] discussed wave loads on jetties, which are pile supported piers with decks and beams. Tests were performed on a 1:25 scale model. Various configurations were tested to identify the effects of inundation, which resulted in a dimensionless equation for the deck force. During tests, for the same test configuration, variation in force magnitude and time-history shape was observed. The idealized, averaged force signal time history was presented.

2.4 Vertical members

French [20] also described characteristics of fluid forces upon a vertical wall. Noticeable high peak pressures were recorded. The laboratory test showed those peak pressures occur only during wave breaking at the wall. When the wave did not break or if it broke before hitting the wall, no significant peaks were observed. Instead, slow-varying pressures occurred. During the tests, trapped air along the wall was also observed. Experiments proved the highest pressure variations are a result of the air layer thickness. All measured pressures differed significantly.

Chan and Melville [37] studied the plunging wave pressure on a vertical wall. Associated impact kinematics and dynamics were investigated. The authors stated the breaking wave produced the highest forces on the wall. The paper does not introduce any specific formulation, but focuses on the wall placement to the wave break position. It was observed the air entrainment leads to higher pressures acting on the wall.

In Cooker and Peregrine [38], the main aim of the research was to investigate forces predicted by a two-dimensional, irrotational, inviscid numerical flow model. The authors indicated that the fluid compressibility effects on forces should be negligible. The researchers mainly focused on the characteristics of wave breaking impingement upon a structure. Using Froude scaling, the prototype pressures appeared significantly overestimated. One of the unexpected features of the flow were transient pressures acting on the wall during impact. Their magnitude was several times higher than hydrostatic pressure. Such characteristics might explain some of the numerical discrepancies.

In Peregrine [39], the author included trapped air entrainment. In case of rapid water motions, the pressures became very high which even exceeded about 10 times the hydrostatic pressure. The same conclusion of high magnitudes holds true for velocities. Similar to previous references, a great variability in pressure results was observed. The peak pressure timescales were very short. In laboratory conditions, the violent peak pressures act for about 1 millisecond with peak duration ranges from about 10 to 100 milliseconds. In two-dimensional wall model, oscillations in pressures were visible, which – author claims – are related to trapped air. The author drew the conclusion that none of the traditional water-wave theories can be used for proper peak estimation.

Trapped air study indicates even a small fraction of air volume in the water influences its compressibility with longer air entrapment with salt (ocean) water. At small scales a relatively significant difference was observed, such as pressures were reduced by 10%, which most likely is the effect of air bubbles. Three-dimensional effects were also considered. In comparison to two-dimensions, the forces and pressure acting on the wall are expected to be lower.

Cross [40] developed a simplified approach for wall force estimation in surge flows. His approach takes into account two cross-sections: one far away from the wall, where flow is not obstructed and the second one taking place right next to the structural wall with water build up. The author assumed a steady condition model, further explaining it does not fully apply in the near structural area, where the conditions are highly dynamic. For non–steady condition the force coefficient (C_F) was introduced, which for steady flow equals 1.0. For non–steady condition the work is largely based on Cumberbatch [41], in which the author focused on water wedge angle development. However, the non-steady condition is based on too many variables, which are not easy to define, therefore, it is not very practical. The reference equation that will be used in this document is

$$F = \frac{1}{2}\rho g h_b^2 + \rho h_b v_j^2 \tag{2.5}$$

in which ρ is the water density, g is the ground acceleration, h_b is the total bore height, and v_j defines incoming bore velocity.

Considering tsunamis and based on the experiments with sloping beach, flat reef, and a vertical seawall in front of the instrumented structure, Asakura [42] proposed

$$F_s = \frac{1}{2}\rho g (3h_j)^2 \tag{2.6}$$

where h_j defines the incoming water jet height traveling on top of a flat reef.

Wood and Peregrine [43] indicated that wave physical behavior is rarely two-dimensional. For near breaking wave action on wall structures, the three-dimensional pressure impulse model was proposed. The authors claim that the water depth does not influence the wall force. General conclusion was drawn that if the wave width is larger

than four times the height of the tested wall structure, the two-dimensional analysis might be employed. When water wave crest is smaller than twice the flume water depth, the three-dimensional analysis is required.

Fujima et al. [44] conducted hydraulic experiments to estimate tsunami wave force acting on rectangular onshore structures. The building models were placed at several distances from a shoreline. Wave pressures were measured with impact pressures showing large variability in results. The tsunami force was overestimated when integrating maximum wave pressure envelope over the surface under impact. The proposed approach is similar to the one proposed by Yeh [31], replacing the drag coefficient, C_D, with a constant. The experimental setup was similar to the one in Asakura [42]. The final form involves two equations, based on the maximum water inundation level and distance of the instrumented structure from the reef break. The equation, which applies the most to conditions under consideration in this dissertation, is

$$F = 1.3\rho h_j v_j^2 \ . \tag{2.7}$$

Recently, Nouri et al. [45] conducted experimental tsunami impact study on free standing structures. The results were compared to other previously conducted experimental studies [6, 25]. The circular and rectangular, hollow, plexi-glass columns were tested. The bores were generated with a dam break setup. Structures were located about 5 m downstream from the dam column. The authors verified the force due to turbulent continuous flow upon slender elements corresponds to the drag force and depends on the depth of the impoundment bore, which directly relates to the steeper bore slope.

2.5 Summary of literature review in terms of structural forces.

Most of the experimental studies used a two–dimensional domain [1, 10, 15-23, 25, 26, 28-31, 38, 42-44, 46], i.e. a wave flume. The experimental data showed high pressure variability on the instrumented structure [20, 38, 39, 43, 44]. The large fluctuations were attributed to entrapped air [23, 37, 39], which affects measured pressures [20, 37, 39]. Many of the proposed formulae are not suitable in structural design under generalized tsunami wave impact. Some of the calculation methods only apply to specific condition

or were not tested in wide range application. A few claim that for some conditions Froude scaling is not applicable [23, 39].

In terms of analytical force formulation, a common approach was to consider forces from momentum [16, 17, 21, 26, 40, 44] and drag [1, 16, 21, 26, 30, 31], with only a few considering hydrostatic forces [23, 40, 42].

The review shows that most of the approaches in the literature were not designed for bore impact resulting from a broken tsunami wave traveling on top of a wet-bed. Additionally, most of the existing literature only considers dry-bed conditions [25, 28, 29, 40, 42].

2.6 Debris impact.

A significant threat to structures in the tsunami inundation zone is impact from debris driven by the tsunami flow [47]; a proper characterization of these forces is especially important to life-safety related to vertical tsunami evacuation shelters [26]. Debris impact is also an important design consideration for fuel and chemical storage tanks, and port and industrial facilities, all of which may unavoidably be located in tsunami inundation zones. In addition, hurricane or flood-driven, water-borne debris pose similar threats. At port locations, there are often hundreds to thousands of containers. A standard 12.2 m (40 ft) container has an empty mass of 3,630 kg and a full mass of 30,500 kg; a full container would have a nominal draft of about 0.914 m. A reasonable, expected flow speed could be between 4.5 and 9.0 m/s. Hence, floating containers can pose a significant impact threat to structures in the path of the flow. To properly design structures to resist these demands it is necessary to quantify the impact forces generated by these events.

The debris impact area does not have many works in English. There are some in Japanese, however these are not accessible. Except those papers the debris impact is not a widely researched area with only a few significant references. Haehnel and Daly [48, 49] developed a one degree of freedom impact force model. Woody debris experimental tests were conducted impacting a rigid wall. Their approach assumes the impact force is a function of debris impact velocity, the mass of the debris, and the effective stiffness (combined stiffness of the projectile and structure under the impact). Assuming the

projectile impacting the structure is rigid, approach does not depend on its physical properties.

Matsutomi [50] provides a method to estimate the debris impact force due to simultaneous or near-simultaneous impact of multiple driftwood pieces accompanying tsunami inundation flow. The paper also investigates probability of collision occurrence.

Yeom et al. [51], recently published a computational study investigating drift container model collision with a rigid object. The results were compared to scaled down experimental study model, which is presented in the paper. Investigation showed the validity of the computational model as a possible analysis tool. Other publications include such works as barge collision on bridge piers [52-54], navigation locks [55], and impact of shipping containers on waterfront structures [56-58]. FEMA P646 [26] states that more comprehensive studies are required to quantify impact forces.

Nouri et al. [45] investigated experimentally tsunami impact on free standing structures. In the experiments a bore resulting from a dam break was used. Hollow rectangular and circular columns made out of acrylic plexi-glass were tested. The data collection frequency was 1000 Hz. The downstream distance between the dam gate and structure under impact was 4.67 m. Two different sizes of log were tested, 600 and 800 mm, with the same cross-sectional area (38 x 178 mm). Upon the impact a sudden force spike was recorded followed by a gradual increase in force time-history. In some cases second peak was visible, which consisted of up to 28% of the first peak. The impact duration exceeded the sound speed propagation in the timber element. Results also indicated the impact duration was independent of the log mass, which was not in the agreement with Haehnel and Daly [48, 49], where the authors stated the impact duration depends on the debris mass.

Recently, Hiraishi et al. [59] conducted experimental study on impulsive force of drift body due to tsunami flow. In the experiments, the maximum horizontal force on a vertical column was measured. The collision force was determined based on drift velocity and a projectile mass and an empirical equation was obtained, specifically

$$F = \alpha \frac{mv}{\Delta t} \tag{2.8}$$

in which α is a coefficient derived from the experiments, Δt is the impact duration time derived from the field test and equaled 0.01 sec, m is the mass, and v is the driftwood velocity and was about 75% of the tsunami flow velocity. The timber projectile length used in the experiments was 10 m and 1 m in diameter.

Code provisions for debris impact forces are based on basic rigid-body impact models and limited experimental data, but despite its importance there is no consensus how to define design impact forces. Debris impact is covered in several codes and design standards. ASCE 7 [60], the Coastal Construction Manual (CCM) [61], and FEMA P646 [26] focus on building structures, while AASHTO [62] focuses on vessel collision with bridge piers and a US Army Corps of Engineers (USACE) document [63] focuses on barge impact on navigation locks. Three typical approaches are used to obtain expressions for impact force: impulse-momentum, work-energy, and contact stiffness [31, 49]. Approaches that are based on a physics-based model assume rigid body impact, while the others develop empirical equations to fit experimental data. ASCE 7 takes an impulse-momentum approach involving two rigid bodies, which results in

$$F = \frac{\pi\, m_p v_f}{2\, \Delta t} \tag{2.9}$$

in which F is the impact force, m_p is the total mass of the projectile (i.e., the debris), v_f is the impact velocity, and Δt is the time to reduce the object velocity to zero. A Δt of 0.03 s is recommended. CCM takes a similar value for time duration.

FEMA P646 [26] follows the formulation proposed by Haehnel and Daly [48, 49], which is based on the impact of two rigid bodies with a contact stiffness between them. Their equation for impact force is

$$F = v_f \sqrt{k_c m_p} \tag{2.10}$$

in which k_c is a contact stiffness that must be determined experimentally. Similar equation is used in Eurocode [64], where the variables refer to the ship velocity, equivalent ship stiffness, and mass. FEMA P646 modified this equation by adding a force

amplification factor of 2.0 to include the ‘added mass’ effect, i.e., the increase in force from the presence of the water. There was no justification for the value selected. Some other manuals also include a force increase for the water inertia [62], although much less than double.

Work-energy for debris flow is not used in this country, although it can be shown that all three approaches are identical if certain assumptions are made [49]. AASHTO [62] considers work- energy for vessel collisions with bridge piers, but the force equations are based more on empirical data than on a physical model. The commentary points towards recent work [52], indicating that a more refined, analysis-based procedure is needed. Excluding the empirical, data-driven AASHTO and USACE equations, the presented approaches are all based on impact of rigid bodies. However, a shipping container impacting a concrete column or wall, or even a steel column, is not rigid compared to the structure it strikes. In fact, for a prototypical 68.6 cm square concrete column [65] being hit by a shipping container, the column is essentially rigid compared to the container (based on static stiffness). Furthermore, the application of rigid body impact theory is appropriate if the duration of impact is much larger than the natural period of the bodies [66]; this is not the case with the debris.

Chapter 3

Bore impact on a vertical wall

3.1 Overview

In this chapter a series of experiments to quantify tsunami bore forces on a vertical wall is described. The experimental setup is described. The wall force time-histories are presented. Based on the data, a design formula for maximum wall force resulting from bore impact is proposed and compared with existing formulas.

3.2 Small scale tsunami wave impact experiments

The US National Science Foundation (NSF) has funded a grant to improve the understanding of tsunamis and their threat to the built environment. The aspect of this initiative is the funding of the NSF Network for Earthquake Engineering Simulation (NEES), which includes Oregon State University's (OSU) Large Wave Flume (LWF). The LWF is 104 m long, 3.7 m wide, and 4.57 m deep. The wave-maker is a piston-type hydraulic actuator capable of producing regular, irregular, and solitary (tsunami-like) waves. The wave periods range from 0.5 s to 10 s. The piston has a maximum stroke of 4 m and a maximum velocity of 4 m/s. Further details on the experimental setup and instrumentation are presented by Santo and Robertson [67]. More information on the facility can be found at the OSU website [33].

The experimental setup is illustrated in Figure 3.1. The experiments involved a solitary wave propagating 'offshore' over a flat bottom, shoaling over a 1:12 beach slope, and onto a flat reef. A solid wall was located on the reef, 83 m from the wave maker. The beach slope terminated 2.36 m above the flume bottom. The beach and reef were made with smooth concrete though some experiments included a bed form on the beach slope as part of a parallel study on the effect of bottom roughness. The wave flume was 3.7 m wide.

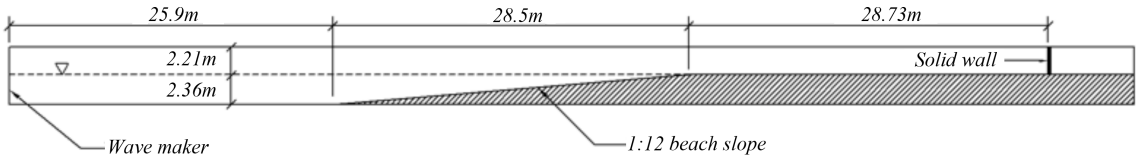

Figure 3.1. Beach slope and fringing reef with solid wall specimen.

A tsunami impacting a shoreline consists of several long period waves, and the largest wave is not necessarily the first wave. Hence, there is a good chance that there will be standing water on-shore from a previous wave, when a large wave hits. As a result, the water level in the wave flume was varied from 2.36 m to 2.66 m so as to change the still water level on the flat reef. For a water level of 2.36 m, there was no water on the flat reef. For the maximum water level of 2.66 m the still water on the flat reef was 30 cm deep.

The incoming solitary wave transformed to a turbulent bore/surge at the transition between the beach slope and the fringing reef. This bore/surge then impinged the structural test specimen, i.e., the wall. The characteristics of this bore were captured using a high-resolution video camera filming an 8 m length of flume in front of the test wall at 60 frames per second. The side wall of the flume was painted black for improved contrast with the turbulent bore. Post-processing of the video capture was used to determine bore height and velocity at mid-height of the leading edge. These results were validated by comparison with resistance wave gages and ultrasonic wave gages located along the side wall of the flume (Figure 3.2).

Figure 3.2 shows the instrumented wall installed in the wave flume. The lower 1.83 m height of wall was constructed using a 6mm thick aluminum plate reinforced by 200 mm deep aluminum I-beams spanning across the flume. The wall was attached to brackets mounted on the sidewalls of the flume by means of four load cells, identified as LC1 to LC4 in Figure 3.3. A flexible rubber seal was installed around the edge of the wall to prevent water from passing behind the wall. The seal did not provide any resistance against lateral loads on the wall. A 2.44 m high plywood extension was attached to the top of the aluminum wall to prevent any overtopping. All lateral load applied to both

aluminum and plywood walls was measured by the four load cells behind the wall. Plywood splashguards were also fitted to the top of the flume sidewalls in front of the test specimen to prevent water from exiting the flume.

Figure 3.2. View of instrumented aluminum wall and plywood extension to prevent overtopping

Thirteen FPG pressure sensors were installed along the vertical centerline of the wall as shown in Figure 3.3. Four Druck pressure sensors were installed adjacent to selected FPG sensors for the purpose of validating the pressure readings. The load cells and pressure sensors were monitored at 1000 Hz throughout each wave impact.

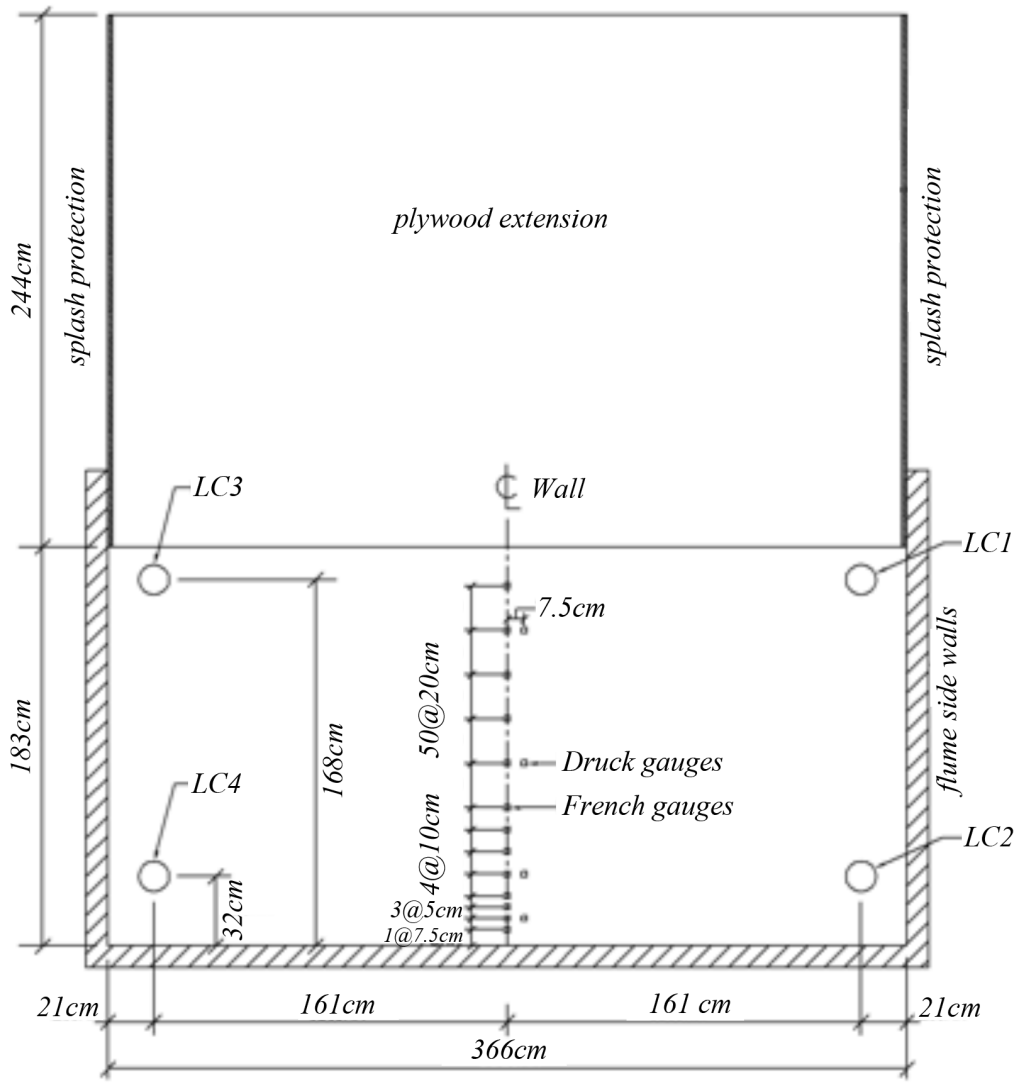

Figure 3.3. Wall instrumentation.

The wave maker generated solitary waves with heights varying from 0.10 to 0.50 times the offshore water depth. Solitary wave heights used in these experiments are listed in Table 3.1, together with the number of times each case was repeated (in parentheses). Each wave configuration was run between 2 and 4 times to ensure repeatability and quantify any variation in loading on the wall.

Although the dry bed case was also considered, the bore/surge is qualitatively different than when there is initial standing water. This results in different bore front build-up, where for small height waves a surge flow was generated. Such flow results in

different flow velocities and therefore different characteristics. Therefore, the focus herein is on the cases with initial standing water.

Table 3.1. Wave heights in cm and number of trials.

Water depth in flume d (m)	Still water depth on reef d_s (cm)	Ratio of wave height to water depth in flume							
		0.10	0.15	0.20	0.25	0.30	0.40	0.45	0.50
2.36	0	23.6 (4)	35.4 (2)	47.2 (4)	59 (2)	70.8 (4)	94.4 (4)	106.2 (2)	118 (4)
2.41	5	24.1 (4)	36.15 (2)	48.2 (4)	60.25 (2)	72.3 (4)	96.4 (4)	108.45 (2)	120.5 (4)
2.46	10	24.6 (4)	36.9 (2)	49.2 (4)	61.5 (2)	73.8 (4)	98.4 (4)	110.7 (2)	123 (4)
2.56	20	25.6 (4)	38.4 (2)	51.2 (4)	64 (2)	76.8 (4)	102.4 (4)	115.2 (2)	128 (4)
2.66	30	26.6 (4)	39.9 (2)	53.2 (4)	66.5 (2)	79.8 (4)	106.4 (4)	119.7 (2)	–

All data are available at https://nees.org/warehouse/project/624/ [68].

3.3 Experimental results

All the results are part of research published in [67, 69, 70] and were performed by researchers under supervision of I.N. Robertson. The experimental result plots presented here are only for the smallest and the biggest waves. Remaining results can be found in [67] and online repository [68]. Figure 3.4 and Figure 3.5 show time histories of the total lateral force on the wall, as measured by the load cells, from four bores produced by 24.1 cm and 120.5 cm high solitary waves, respectively, over a reef with 5 cm standing water. The time scale starts shortly prior to the first measurement of load on the wall. Note that the vertical scales differ to increase plot clarity. Wave trials designated with BS1 and BS2 involved different bed form roughness on the beach slope leading up to the reef. These bed forms were part of a parallel study investigating the effect of bottom roughness on wave breaking and bore formation. Bed form BS2 was a more pronounced roughness than BS1, leading to slightly lower wall forces, particularly for smaller incoming waves. The variation in time history between nominally identical incoming waves is also related to the turbulent nature of the leading edge of the bore as it propagates over the flat reef.

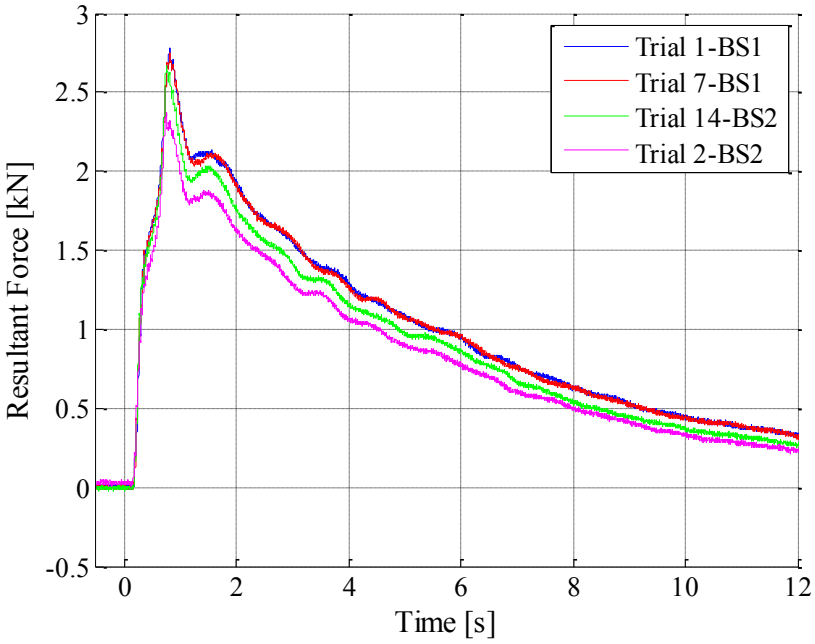

Figure 3.4. Force time history for 24.1 cm waves with 5 cm standing water on reef [67].

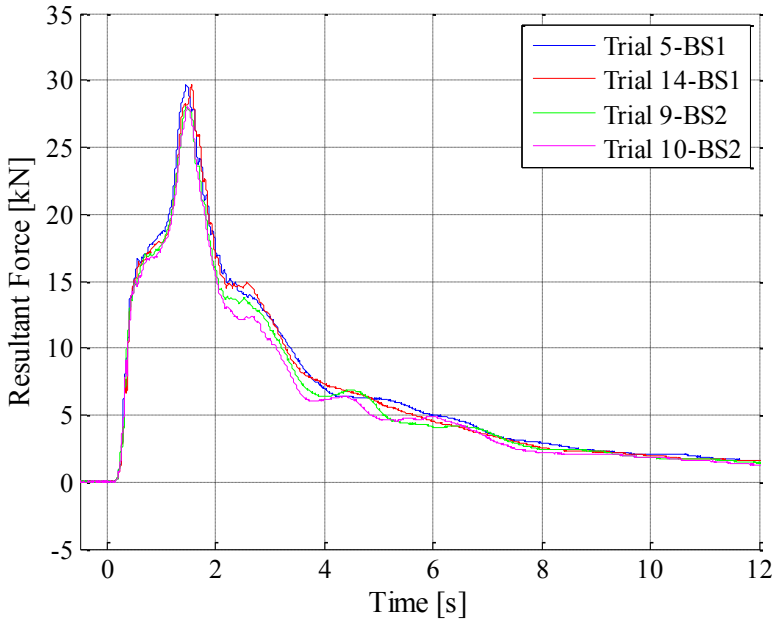

Figure 3.5. Force time history for 120.5 cm waves with 5 cm standing water on reef [67].

During the measurements one of the four load cells malfunctioned. As a result, for post-processing purposes, the data for the given load cell was replaced with a load cell

history from the same height, but opposite side of the wall, i.e. load cell 4 was replaced with load cell 2 data. The final result is verified through integration of the pressures, which gave good comparison with the load cell measurements as shown in Figure 3.6 and Figure 3.7.

Each time history is characterized by a steep loading ramp to approximately 2/3 of the peak load, which coincides with the incident bore being redirected up the face of the wall. The load increases more slowly until reaching a peak when the run-up collapses onto the incoming flow. The peak load is followed by a rapid decrease to a sustained, though fluctuating, residual lateral load. A reflective bore has now formed travelling away from the wall over the incoming flow. This residual load dissipates with time as the incoming flow decreases due to the relatively short wavelength of the solitary waves generated in the laboratory flume. During a tsunami this residual load would be expected to continue for a longer duration.

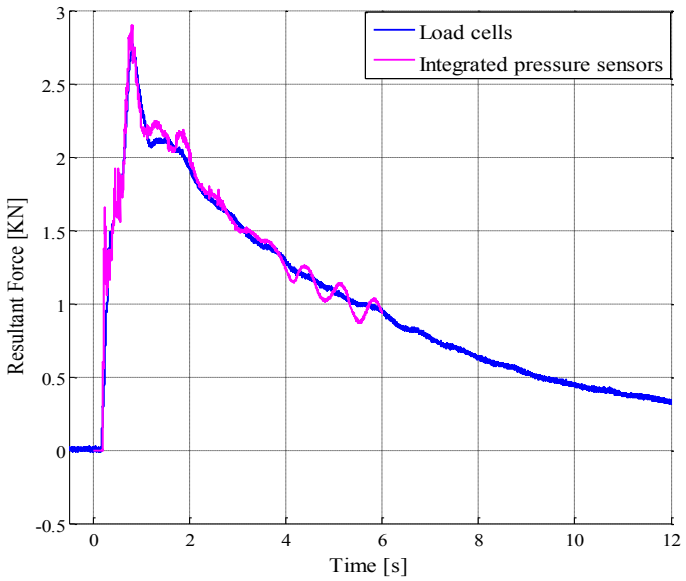

Figure 3.6. Comparison of load cell and integrated pressure for force for 24.1 cm wave with 5 cm standing water on reef [67].

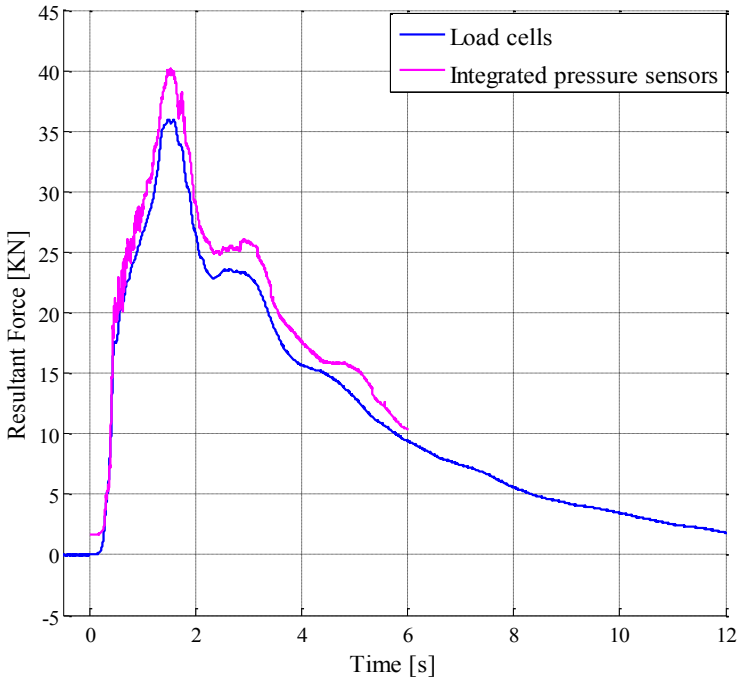

Figure 3.7. Comparison of load cell and integrated pressure for force for 106.4 cm wave with 30 cm standing water on reef [67].

Figure 3.8 and Figure 3.9 show the pressure sensor readings up the centerline of the wall at the peak lateral load for a typical 24.1 cm and 120.5 cm wave trial on top of 5 cm standing water level, respectively. Figure 3.10 and Figure 3.11 show the pressure sensor readings up the centerline of the wall at the peak lateral load for a typical 53.2 cm and 106.4 cm wave trial on top of 30 cm standing water level, respectively. The linear regression lines are shown for all sensors measuring significant pressure. For these cases, the linear pressure fit was approximately 0.8 times the hydrostatic pressure for the corresponding water height. The exception is the smallest wave with 5 cm standing water level, where the ratio was 1:1.

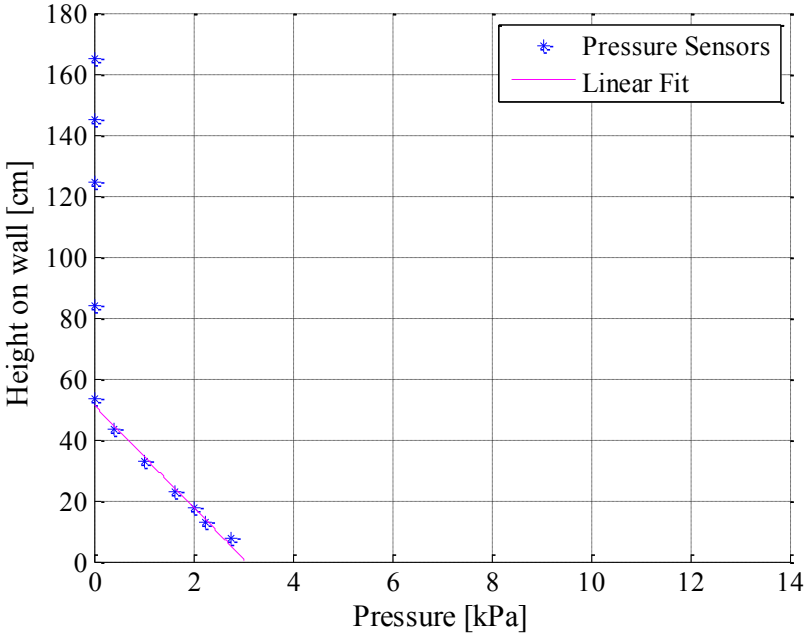

Figure 3.8. Typical wall pressure distribution at peak lateral load for 24.1 cm wave with 5 cm standing water on reef [67].

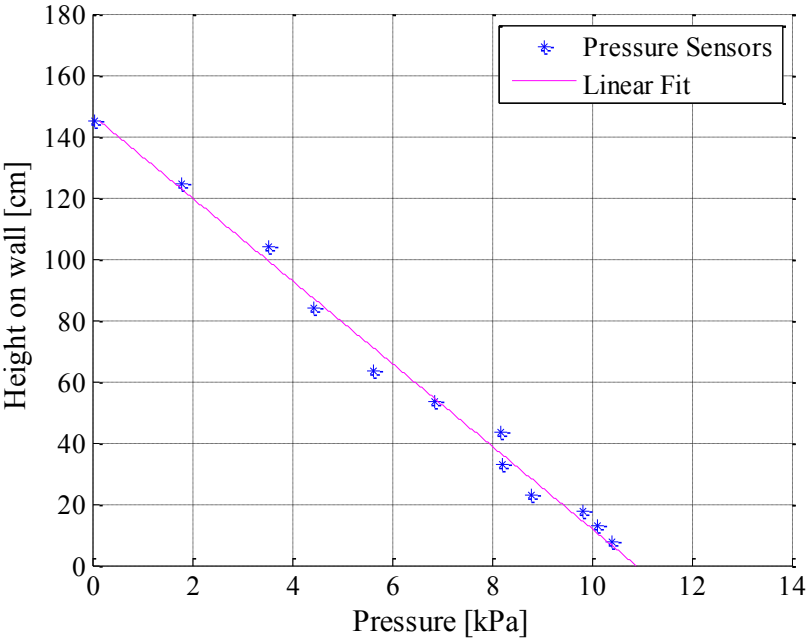

Figure 3.9. Typical wall pressure distribution at peak lateral load for 120.5 cm wave with 5 cm standing water on reef [67].

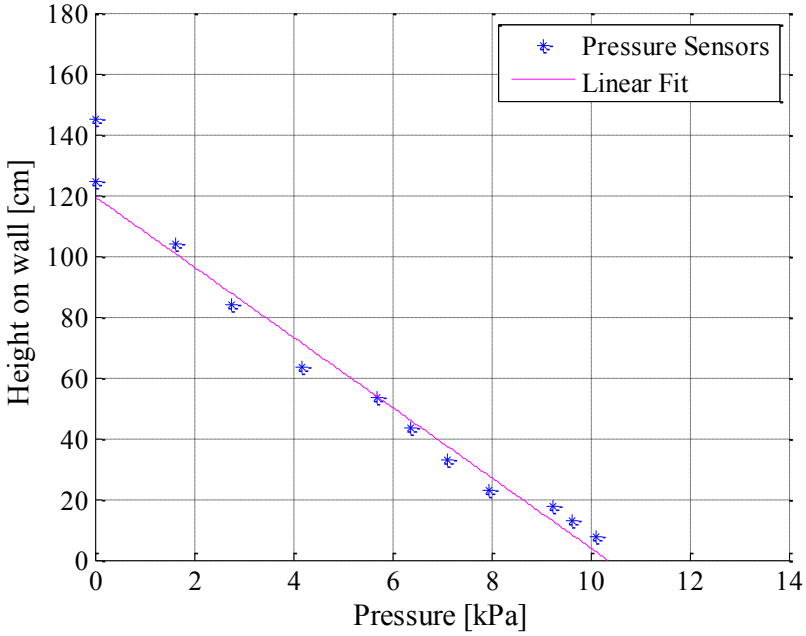

Figure 3.10. Typical wall pressure distribution at peak lateral load for 53.2 cm wave with 30 cm standing water on reef [67].

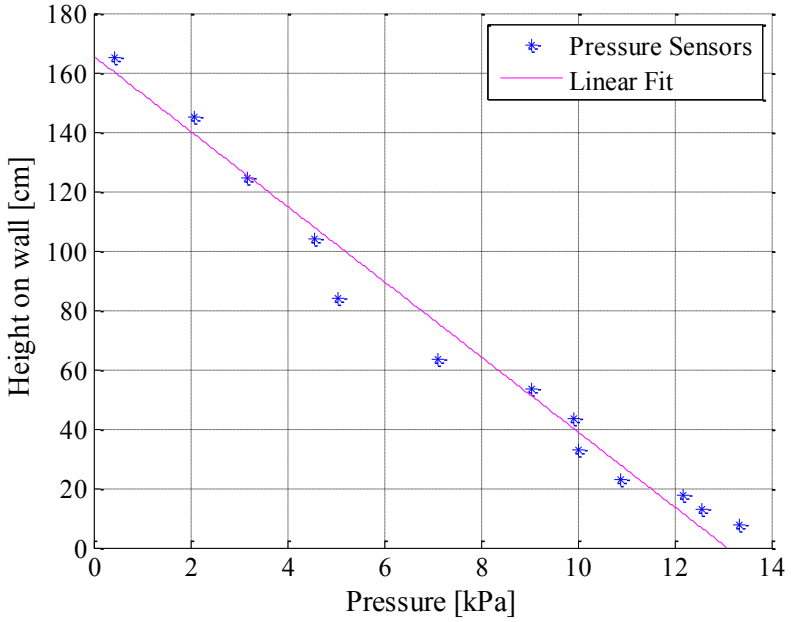

Figure 3.11. Typical wall pressure distribution at peak lateral load for 106.4 cm wave with 30 cm standing water on reef [67].

Figure 3.12 and Figure 3.13 show time histories of the total lateral force induced on the wall specimen for four bores produced by 53.2 cm and 106.4 cm high solitary waves, respectively, over 30 cm of standing water on the reef. The time histories show a similar trend to that observed for the 5 cm standing water condition.

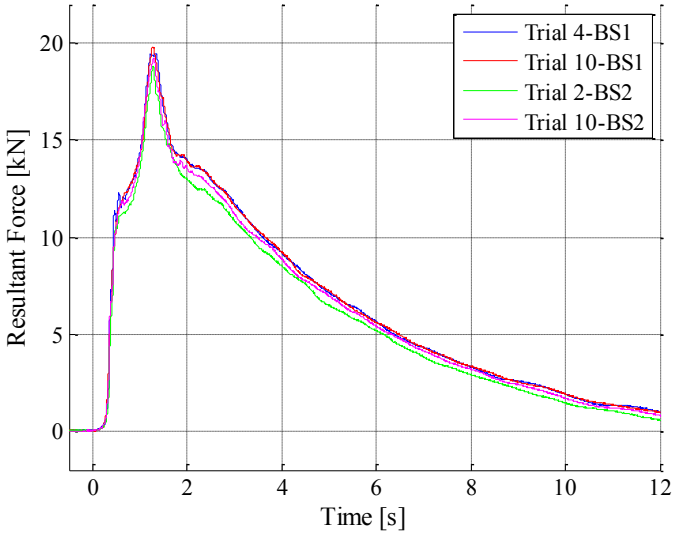

Figure 3.12. Force time history for 53.2 cm waves with 30 cm standing water on reef [67].

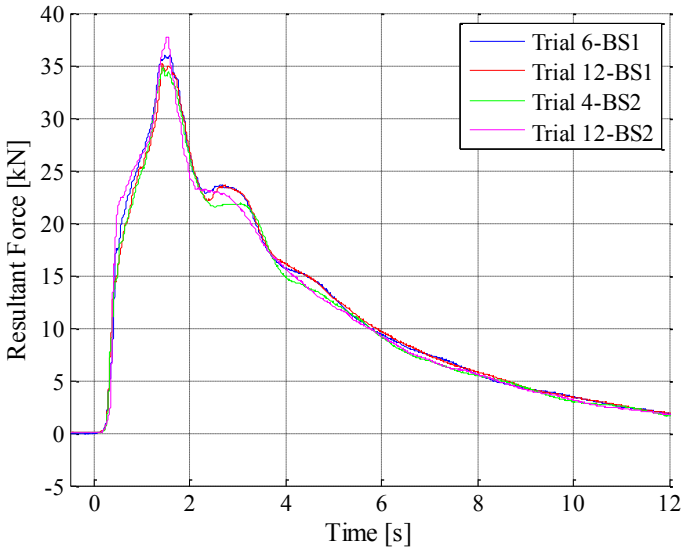

Figure 3.13. Force time history for 106.4 cm waves with 30 cm standing water on reef [67].

3.4 Froude scaling

In this section, the validity of Froude scaling applied to the impact force will be checked.

Figure 3.14 shows a schematic of a bore propagating on the reef. The bore depth, h_b, is the sum of the initial standing water level, d_s, and the jump height, h_j. Traveling at speed v_j.

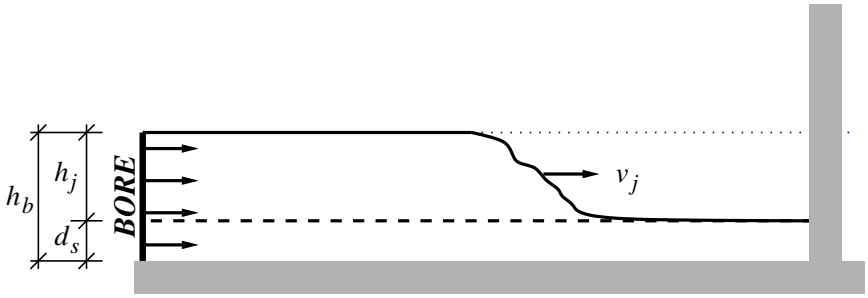

Figure 3.14. Tsunami bore characteristics.

Because a tsunami bore behaves as a gravity wave, it is commonly assumed that scaling from model to prototype follows Froude scaling. The Froude number is defined here in terms of the height of the incoming jump, h_j, and the jump velocity, v_j, i.e.,

$$Fr = \frac{v_j}{\sqrt{gh_j}} \tag{3.1}$$

The bore front velocity was measured by processing video of the moving front captured by a high-resolution camera [71]. Figure 3.15 shows the resulting Froude numbers for all experimental wave trials over the reef with 5, 10, 20 and 30 cm standing water. The inset in Figure 3.15 shows the mean as well as the minimum and maximum values for all waves at each of the standing water levels. Although there is some scatter in the data, it would appear that the incoming hydraulic jump has a Froude number of approximately 2.0 for all standing water depths.

Mohamed [71] suggested that hydraulic jump theory provides a good estimate for the incoming bore velocities. From hydraulic jump theory,

$$v_j = \sqrt{\frac{1}{2} g h_b \left[\frac{h_b}{d_s} + 1\right]} \tag{3.2}$$

or equivalently,

$$Fr = \frac{v_j}{\sqrt{g h_j}} = \sqrt{\frac{1}{2}\frac{h_b}{h_j}\left[\frac{h_b}{d_s} + 1\right]} \tag{3.3}$$

When equation (3.3) is plotted the velocity function follows the recorded experimental data fairly well (the solid line in Figure 3.15).

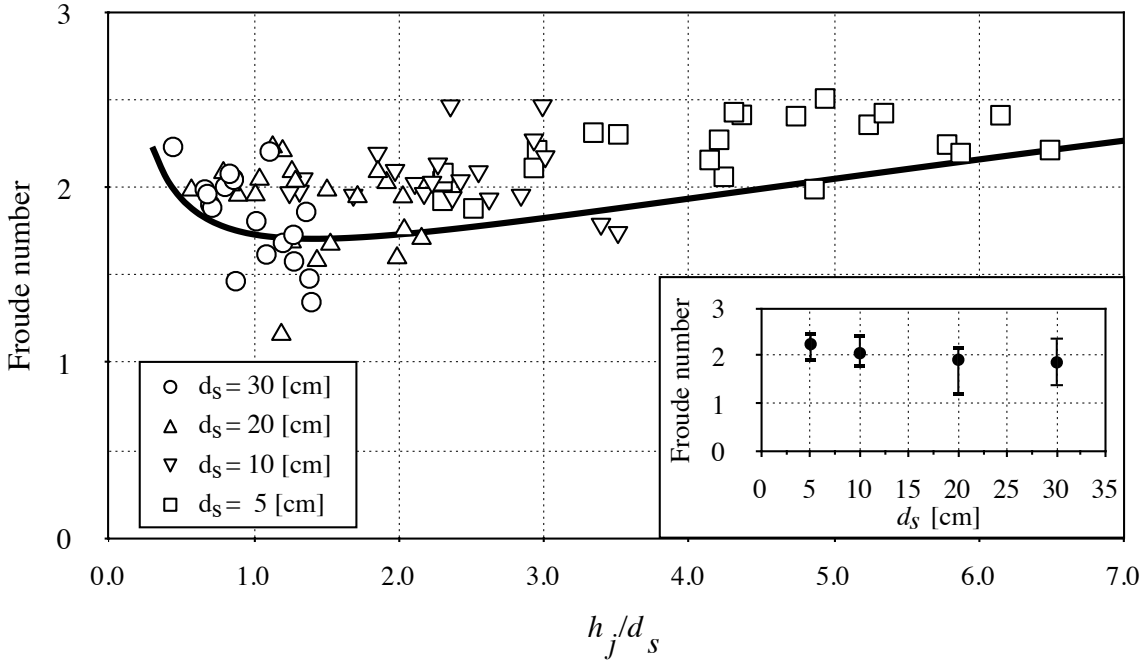

Figure 3.15. Froude number for all wave trials with predicted velocity depicted in thick black line. Inset plot shows average values for each standing water depth.

Froude scaling implies that the force on a prototype structure, F_p, can be determined from the force on the model structure, F_m, using

$$F_p = F_m \lambda^3 \tag{3.4}$$

where λ is the dimensional scale between prototype and model. For the two-dimensional condition tested in this study, the out-of-plane dimension was not scaled. Therefore, for the experimental data, Froude scaling reduces to

$$F_p = F_m \lambda^2 \tag{3.5}$$

All relevant dimensions must change by the same ratio, λ, for Froude scaling to apply; specifically

$$\lambda = \frac{h_{jp}}{h_{jm}} = \frac{d_{sp}}{d_{sm}} \tag{3.6}$$

where subscripts *p* and *m* refer to prototype and model, respectively. This means that both the standing water depth and jump height have to change by the same ratio. Given that the standing water depths were 5, 10, 20 and 30 cm, this implied available λ values of 1.5, 2, 3, 4 and 6. The jump heights were compared to find those pairs that matched one of these λ values within 5%. Matches were only found for λ values of 1.5, 2 and 3. Figure 3.16 shows the relationship between the ratio of maximum forces and λ^2 for these matching conditions. Although there is scatter about the one-to-one match line, which could be a results of air compressibility, these data appear to confirm that Froude scaling is appropriate for the maximum force applied by a tsunami bore to a solid wall, as discussed by others [72].

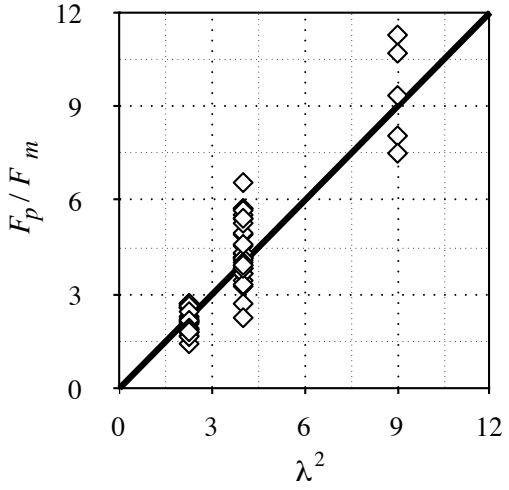

Figure 3.16. Verification of Froude scaling.

3.5 Derivation of design equation for vertical wall force estimation

3.5.1 Simplified model

The data for the wet-bed case have been used to develop a design equation for the maximum bore impact force on a wall. The equation is based on the simplified model shown in Figure 3.17. In addition to d_s and h_j, h_r is defined as the height of the reverse flow that results from the reflection of the incoming fluid. The sum of the heights defines the total ponding height, h_p. It is assumed that each of the three fluid layers has a uniform velocity, v_s, v_j and v_r, respectively.

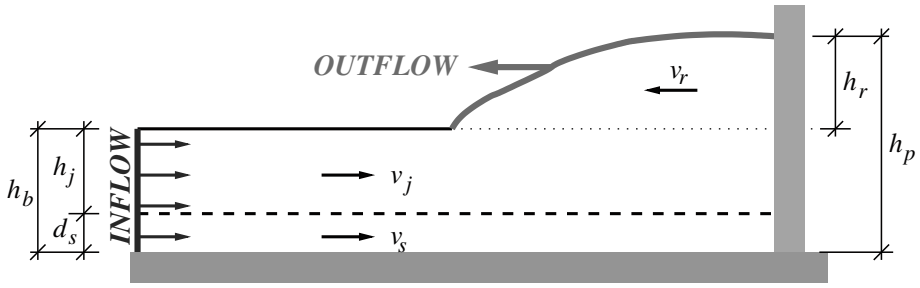

Figure 3.17. Schematic of bore impacting wall

3.5.2 Conservation of mass

It is reasonable to assume that the velocity in the initial standing water layer is some fraction of the incoming jump velocity, i.e.,

$$v_s = \alpha_s v_j \tag{3.7}$$

From the conservation of mass inside the control volume indicated by the fluid boundaries shown in Figure 3.17, and assuming an incompressible fluid,

$$v_j\left(h_j + \alpha_s d_s\right) = v_r h_r \tag{3.8}$$

The reverse velocity v_r can be expressed in terms of the Froude number of the reverse velocity, Fr_r, as

$$v_r = Fr_r\sqrt{gh_r} \tag{3.9}$$

Substitution of equation (3.8) into (3.7) results, after some manipulation, in the following expression for h_r:

$$h_r^{3/2} = \frac{v_j(h_j+\alpha_s d_s)}{Fr_r\sqrt{g}} \tag{3.10}$$

3.5.3 Momentum Equation

Assuming momentum accumulation within the control volume is zero, the one dimensional momentum flux can be written as

$$F = \sum(\dot{m}v)_{in} - \sum(\dot{m}v)_{out} - \int_{in} p\, n\, ds - \int_{out} p\, n\, ds \tag{3.11}$$

where F is the force per unit width on the wall, $\dot{m}$ is the mass flow rate per unit width, v is the velocity, p is pressure, and n is the sign of the normal to the control surface. If it is assumed that the pressure on the inflow boundary is hydrostatic and on the outflow boundary is atmospheric, equation (3.11) can be written as

$$F = \rho h_j v_j^2 + \rho d_s v_s^2 + \rho h_r v_r^2 + \frac{1}{2}\rho g h_b^2 \tag{3.12}$$

where $h_b = h_j + d_s$. Substitution of equation (3.7) into (3.12) and rearranging gives

$$F = \frac{1}{2}\rho g h_b^2 + \rho\left(h_j + \alpha_s^2 d_s\right)v_j^2 + \rho h_r v_r^2 \tag{3.13}$$

Using equation (3.8) and (3.9), the last term of equation (3.13) can be written as

$$\rho h_r v_r^2 = \rho\left[\frac{v_j(h_j+\alpha_s d_s)}{\sqrt{g}}\right]^{4/3} g\, Fr_r^{2/3} \tag{3.14}$$

The expression for force involves the parameters, v_j, α_s, Fr_r, d_s and h_j.

3.5.4 Vertical wall force equation

It can be assumed that a designer will be able to specify d_s and h_j as part of the design condition. The hydraulic jump equation, equation (3.2), is used to estimate v_j given d_s and h_j. It remains to specify for α_s and Fr_r. Considering all the data sets for d_s = 5, 10, 20, and

30 cm, the method of least–squares was used to obtain values for α_s and Fr_r. These values were 0.0 and 0.96, respectively. For simplicity and practical application, the values α_s = 0.0 and Fr_r = 1.0 are chosen here. The first value implies that as the jump portion of the water enters the domain, the still water velocity will always be 'zero'. Substitution of the values for α_s and Fr_r, and using equation (3.14), equation (3.13) simplifies to

$$F = \frac{1}{2}\rho g h_b^2 + \rho h_j v_j^2 + \rho g^{1/3}\left(h_j v_j\right)^{4/3} \tag{3.15}$$

Equations (3.2) and (3.15) provide a relatively simple approach to calculate impact force based on design input values for h_j and d_s (h_b=h_j+d_s) only.

3.6 Validation of vertical wall force equation

3.6.1 Overview

The equations for the wall force on a vertical wall, equations (3.2) and (3.15), are validated based on the experimental data and compared to existing models. The error in each case is calculated and a discussion of results is presented.

3.6.2 Alternative approaches

Equation (3.15) will be compared to several previously proposed equations. Cross [40] proposed

$$F = \frac{1}{2}\rho g h_b^2 + \rho h_b v_j^2 \tag{3.16}$$

Equation (3.16) results from the present approach if α_s = 1.0 and Fr_r = 0.0 (no reflection).

Asakura et al. [42] proposed

$$F = \frac{1}{2}\rho g (3h_j)^2 \tag{3.17}$$

based on experiments with a similar beach slope and flat reef configuration, but adding a vertical seawall a short distance in front of the test specimen.

Fujima et al. [44] recently published an approach similar to equation (2.3). The experimental setup was similar to Asakura et al. [42]. The final form involves two

equations, based on the maximum water inundation level and structure distance from the reef break. The equation, which corresponds the most to the experimental setup described in section 3.3, is

$$F = 1.3\rho h_j v_j^2 \tag{3.18}$$

3.6.3 Results

In this section the comparison between the different impact force equations is presented based on the data obtained in our experiments.

Figure 3.18 shows the predicted force from the proposed approach (equations (3.2) and (3.15)) Cross (equation (3.16)), Asakura (equation (3.17)), and Fujima (equation (3.18)). The solid black line defines the ideal trend on which the points would lie if the predicted results equaled the experimental results. For points below the line, the force is underestimated; for points above the line, the force is overestimated. Visually, it appears that the proposed approach in general lies most closely to the ideal trend line.

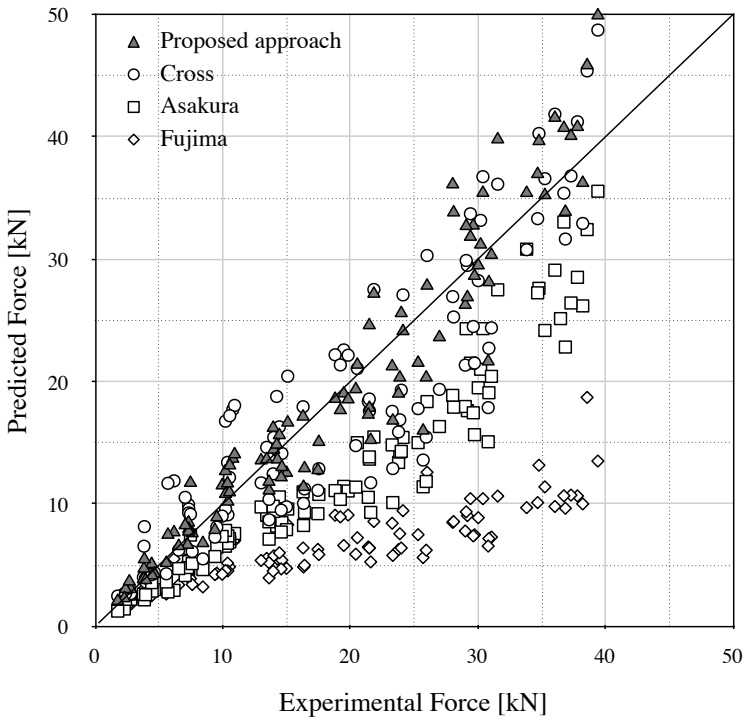

Figure 3.18. Predicted versus experimental force.

The percentage error is defined as the ratio between the absolute value of the error X and the predicted value P for the given trial, i.e.

$$E_{\%} = 100\frac{|X|}{P} \tag{3.19}$$

The percentage error is calculated for each data point. The final value presented in the plots is the average percentage value for all of the data points for each value of h_s, Figure 3.19. In general, the proposed method gives smaller average errors.

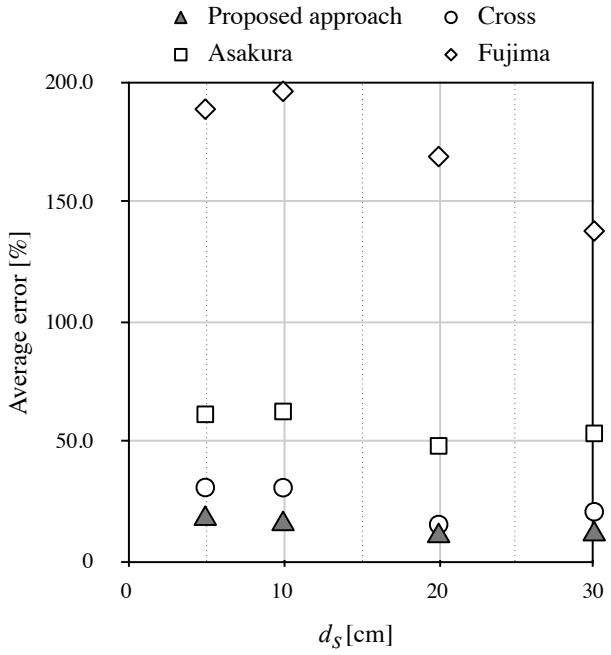

Figure 3.19. Average percentage error versus initial standing water level for results in Figure 3.18.

The arithmetic mean of the difference between measured and predicted value is shown in Figure 3.20.

Let $X_i = M_i - P_i$, where M is the measured force, then the standard deviation can be defined as

$$\sigma = \sqrt{\frac{\sum(X_i - \bar{x})^2}{N}} \tag{3.20}$$

where $\bar{x}$ is the mean value of all the X_i values and N stands for the number of samples in each case.

The quadratic mean is defined such as

$$RMS = \sqrt{\frac{\sum X_i^2}{N}} \tag{3.21}$$

Figure 3.21–3.22 show the standard deviation and quadratic mean of the error, respectively.

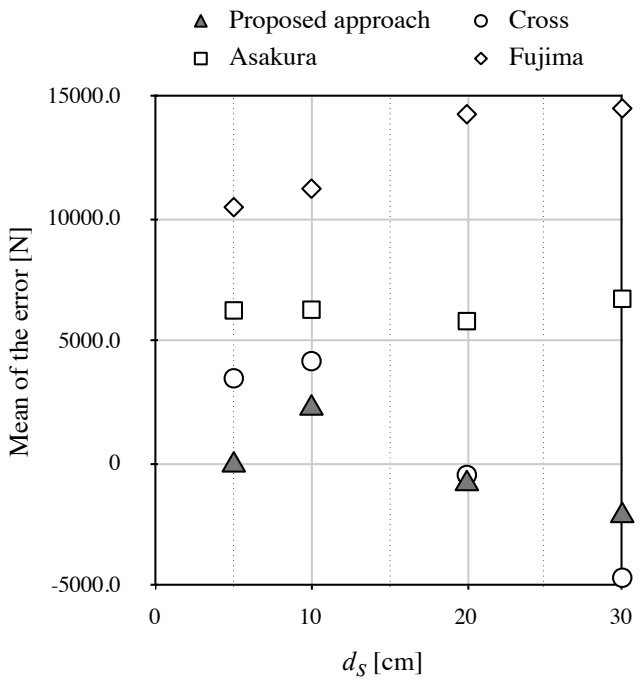

Figure 3.20. Mean of the error versus initial standing water level for results in Figure 3.18.

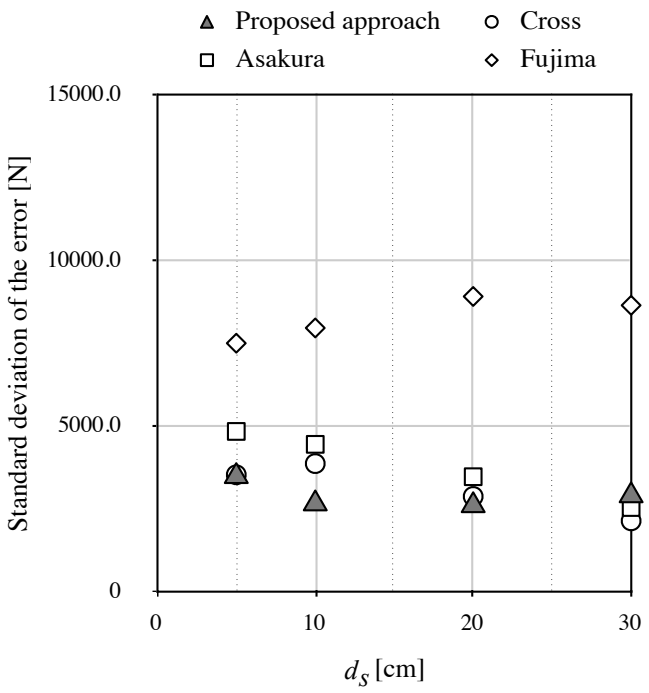

Figure 3.21. Standard deviation of the error versus initial standing water level for results in in Figure 3.18.

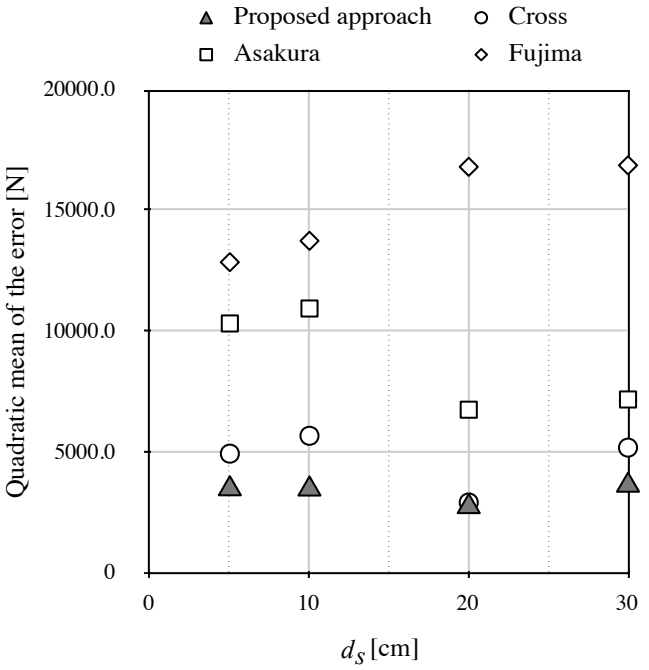

Figure 3.22. Quadratic mean of the error versus initial standing water level for results in Figure 3.18.

Another comparison of the predicted force from equation (3.11) and the experimental result is presented in Figure 3.23. The experimental data points are represented by symbols, whereas the curves are the predicted values. The predictions are quite good. Figure 3.23 also illustrates the variability in the experimental data. Although the incoming solitary waves were dimensionally very consistent, the transformation to a broken bore and the turbulence inherent in the bore resulted in variability in the measured force on the wall for nominally identical test conditions. For each of the still water depths, d_s, identified by the symbols in Figure 3.23, the vertical scatter indicates the variability in resulting wall force peak for bores with a similar jump height, h_j.

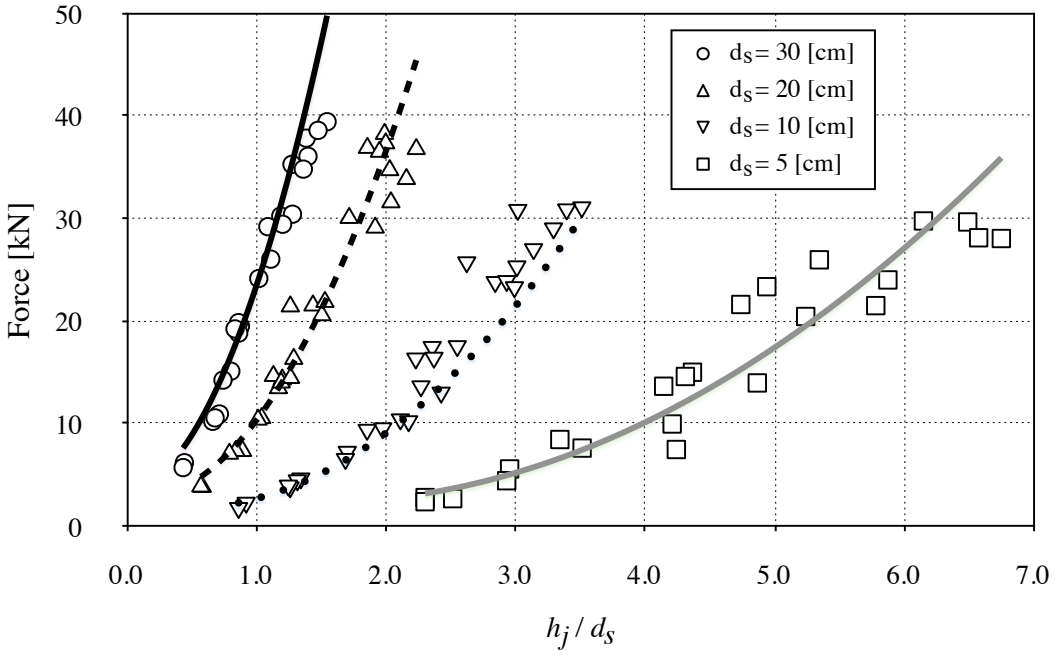

Figure 3.23. Variability and proposed approach match to experimental data.

Figure 3.24 plots the jump height for the range of ratios of solitary wave height to water depth in the flume. For each value of the ratio, the variability in each symbol, signifying the different standing water depths, indicates the variability in bore (jump) height for the same given conditions.

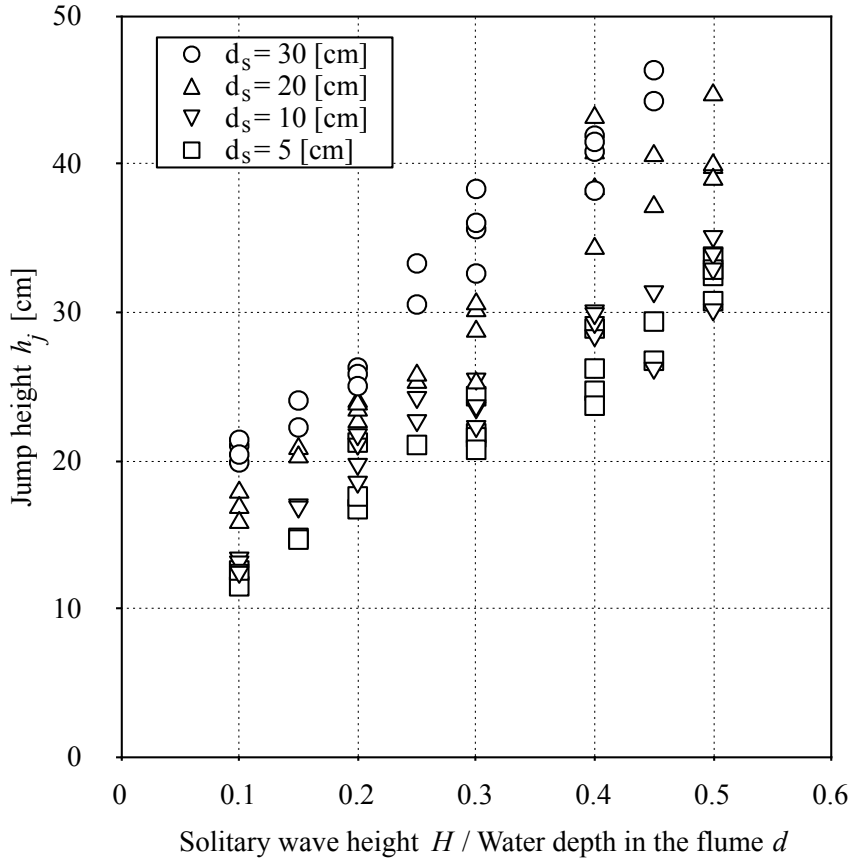

Figure 3.24. Bore height variability resulting from given solitary wave heights traveling over different standing water depths.

Chapter 4

Numerical modeling of tsunami bore impact

4.1 Overview

In the previous section, bore impact upon a vertical wall was described. In more sophisticated structural configurations under water impact, the proposed formula might not be a sufficient solution, i.e. if there are multiple structural elements with offset arrangement, walls with openings, etc. Conducting experiments is only viable for a limited number of scenarios, as they are expensive and time consuming. Computational fluid dynamics is a possible substitute for experimental tests. In this section, a two-dimensional Navier-Stokes computational modeling technique is presented to predict the magnitude of water impact forces on a rigid wall. Different numerical bore generation techniques are investigated and computed forces are compared to the experimental wall forces, presented in [67, 70] and reviewed in Chapter 3. The objective of this section is to provide a template for computational simulation utilizing Navier–Stokes equations of tsunami bore flow formation and its impact on walls.

4.2 Solution method

4.2.1 Tsunami bore flow characteristic and computational model requirements

When a tsunami approaches the shore, in a coastal area, the wave builds up and ultimately breaks, creating highly turbulent, high velocity bore or surge. As the wave propagates, a steep, highly air-entertained bore front is formed. Similar characteristics must be recreated in the computational model to predict accurately the impact force. Computationally, bores were created in three ways: 1) generating a solitary wave [73-75] and forcing it to break on a sloping beach, 2) using a constant velocity inflow boundary condition higher than any initial water depth, and 3) the typical dam break approach [45, 69-71, 76, 77]. The first scenario directly simulated the laboratory conditions. A dam break is also a solution previously tested and validated in literature. The constant inflow

boundary is a new approach. Practical computational solution to turbulent flow is achieved using Navier–Stokes equations with appropriate averaging of turbulent flow properties using two–equation models, i.e. κ–ε [78, 79], κ–ε RNG [80], and κ–ω SST [81, 82].

4.2.2 Governing equations of fluid dynamics

The Navier–Stokes equations are the equations of fluid mechanics governing fluid flows and are known in physics for a long time. Despite extensive research in this field, analytical solutions are limited to a very few cases because of the complexity of the equations. As computers became more advanced and accessible, the solutions to Navier–Stokes equations, using wide variety of numerical techniques, created the field of Computational Fluid Dynamics (CFD). The set of Navier–Stokes equations is used to obtain field variables, such as velocities and pressures. Before the computational process starts, the computational domain is split into smaller pieces. The assembly of many smaller elements called control finite volumes represents the whole domain. The solution is obtained at those discrete elements, which all together represent the full domain response. In case of unsteady flows, the discretization does not only happen in space, but also in time, where time stepping algorithms are used. The complexity of the solution is vast and increases with the dimensionality of the problem.

Based on coordinate system characteristics, there are two possible descriptions of flow field motion, the Lagrangian and Eulerian. The Lagrangian approach is based upon deformable system coordinates, where the coordinates of the domain follow the deformation of the continuous body within the domain, i.e. the fluid. The Eulerian approach is based upon fixed coordinate system, where the discretized domain is composed of control-volumes (CV). Each CV defines a fixed system, where the phases (i.e. water and air) within transfer continuously between control-volumes. In fluid problems with rigid solid boundaries, the Eulerian approach is usually more efficient; it does not require singular water particle tracking. Instead, within each domain cell the quantity transfer is calculated.

The Navier–Stokes equations are a set of partial differential equations, which define governing equations of fluid and are defined through conservation of mass and balance of momentum. The mass conservation equation states

$$\frac{\partial \rho}{\partial t} + \frac{\partial}{\partial x_j}\left(\rho u_j\right) = 0 \tag{4.1}$$

and the momentum balance is

$$\frac{\partial \rho u_i}{\partial t} + \frac{\partial}{\partial x_j}\left(\rho u_j u_i + p\delta_{ij} - \tau_{ij}\right) = 0 \tag{4.2}$$

in which u is the flow velocity, ρ is the fluid density, p is the pressure, δ_{ij} is the Kroneker delta, and τ is the total stress tensor, where for three dimensional domain $i,j=1,2,3$.

4.2.3 Turbulence modeling

Turbulence modeling is a major area of interest in current computational fluid dynamics. The wide variety of turbulence models and lack of information about their performance under different flow conditions contribute to the need of experimental studies, which verify the validity of computational simulations and limit the risk involved in the design process. Different turbulent models were tested and a verification of solutions compared to experimental data was conducted. The following subsections introduce Reynolds averaged Navier–Stokes equations and their extension to include turbulence effects using different turbulence models.

4.2.3.1 Reynolds Averaged Navier–Stokes equations

There are different accuracy approaches to model the turbulence. One of the most comprehensive is Direct Numerical Simulation (DNS). This approach solves Navier–Stokes equations over the whole range of turbulent scales. It is computationally the most expensive; it requires very high spatial and time discretization scale, which makes DNS unsuitable for most applications.

In terms of accuracy and efficiency of the solution, DNS is followed by Large Eddy Simulation (LES). It uses spatial filtering to separate large from small scales. The method

aims to reduce the range of turbulence scales, where small eddies are eliminated from the solution domain.

The most popular and relatively computationally-tractable solution for current engineering needs is based on a statistical approach towards turbulence where modeling involves Reynolds decomposition, hence its name Reynolds–Averaged Navier–Stokes (RANS) equations.

4.2.3.6 RANS statistical decomposition

The concept is based on separation of instantaneous flow variables, i.e. velocity *u*, into averaged and fluctuating components about chosen point in space, i.e.

$$\overline{u_i}(x,t) = u_i^0(x,t) + u_i'(x,t) \tag{4.3}$$

where *x* is a particle position (and can be a vector) and *t* its position in time. Applying the averaging in equation (4.3) to momentum balance, equation (4.2), and the continuity equation for incompressible flow, equation (4.1), the Navier–Stokes equations expressed in averaged form are

$$\frac{\partial}{\partial x_j}\left(\rho\overline{u_j}\right) = 0 \tag{4.4}$$

with the momentum balance

$$\rho\left(\frac{\partial\overline{u_i}}{\partial t} + \overline{u_j}\frac{\partial\overline{u_i}}{\partial x_j}\right) = \frac{\partial}{\partial x_j}\left(\mu\frac{\partial\overline{u_i}}{\partial x_j} - \rho\overline{u_i'u_j'} - \bar{p}\delta_{ij}\right) \tag{4.5}$$

in which the term $\overline{u_i'u_j'}$ is the Reynolds stress tensor and is the only term containing fluctuating variable u'. To correlate Reynolds stress tensor with mean flow variables and hence close the model equations, turbulence models are used.

4.2.3.3 κ–ε turbulence model

The standard κ–ε model is probably the most popular turbulence model found in the literature [78, 79]. It was initially developed to improve the application of turbulence length scales. The transport equations are solved for two quantities, for turbulent kinetic

energy κ and the dissipation rate of turbulent kinetic energy ε, which are both scalar quantities. The transport equation related to turbulence energy is given as

$$\frac{\partial(\rho\kappa)}{\partial t}+\frac{\partial}{\partial x_j}\left[\rho u_j\frac{\partial\kappa}{\partial x_j}-\left(\mu+\frac{\mu_t}{\sigma_k}\right)\frac{\partial\kappa}{\partial x_j}\right]=\tau_{tij}S_{ij}-\rho\varepsilon+\varphi_k \tag{4.6}$$

and the dissipation equation is

$$\frac{\partial(\rho\varepsilon)}{\partial t}+\frac{\partial}{\partial x_j}\left[\rho u_j\varepsilon-\left(\mu+\frac{\mu_t}{\sigma_\varepsilon}\right)\frac{\partial\varepsilon}{\partial x_j}\right]=C_{\varepsilon1}\frac{\varepsilon}{\kappa}\tau_{tij}S_{ij}-C_{\varepsilon1}f_2\rho\frac{\varepsilon^2}{\kappa}\varepsilon+\varphi_\varepsilon \tag{4.7}$$

where Reynolds stresses are

$$\tau_{tij}=2\mu_t(S_{ij}-S_{nn}\delta_{ij}/3)-2\rho\kappa\delta_{ij}/3 \tag{4.8}$$

S_{ij} is the strain-rate tensor and μ_t is the eddy viscosity defined as

$$\mu_t=C_\mu f_\mu\rho\frac{\kappa^2}{\varepsilon} \tag{4.9}$$

where C_μ is the model coefficient. The model requires a near wall treatment defined through a wide range of wall damping functions f_μ and f_2. The wall damping function incorporates wall non–slip effects on flow characteristics, where two main scalar (turbulence transport) quantities defined by the model are zero at the boundaries. The model utilizes a few emprical coefficients, which are C_μ= 0.09, $C_{\varepsilon1}$= 1.45, $C_{\varepsilon2}$= 1.92, σ_k= 1.0, and σ_ε=1.3. For a more detailed explanation, the reader is referred to Launder and Sharma [79].

The model, however, is only valid for fully turbulent flows. The eddy viscosity is determined from a single turbulence length scale. Therefore, the turbulent diffusion occurs only at a specific length scale whereas in reality all different kinds of motions contribute to the overall turbulent diffusion. The model does not perform well in cases where sudden pressure gradients and flow separation occurs [81]. The most noticeable weakness of the model is poor performance calculating adverse pressure gradients. The model seems to also show problems with numerical stiffness where the RANS equations are integrated through a viscous sub-layer, which is governed through a wall damping function, where some numerical issues tend to arise [81].

4.2.3.4 κ–ε RNG turbulence model

The κ–ε RNG model [80] in order to derive Navier–Stokes equations uses Re-Normalization Group (RNG) mathematical theory and essentially does not differ much from the standard κ–ε model. Contrary to a single scale of motion, the model attempts to include other scales of motion through a modified dissipation rate term ε. The main difference appears in the definition of turbulence coefficients, which are C_μ= 0.0945, $C_{\varepsilon 1}$= 1.42, $C_{\varepsilon 2}$= 1.68, σ_k= 0.7194, σ_ε=0.7194, η_0= 4.38, and β=0.012, where η_0 is one of the dissipation coefficients. The model is supposed to perform better in rotational flows.

4.2.3.5 κ–ω SST turbulence model

The κ–ω *SST* model [81, 82] solves the kinetic energy κ and turbulent frequency ω. Additionally, the eddy viscosity formulation is modified to account for transport effects that result from turbulent shear stress. The main feature of the model is a zonal weighting of the model coefficients. The zonal modeling uses the κ–ω model near solid walls and the standard κ–ε model near boundary layers and free shear layers. The switching is achieved with a blending function, where the blending process usually takes place in the wake region of the boundary layer and governs the model coefficients. It allows for more accuracy in near wall treatment. The model shows much better performance in a wall bounded, low Reynolds number flows, and in flows with adverse pressure gradients. The model does not employ damping functions, which leads to significant advantages in numerical stability. However, the model requires increased mesh resolution in near wall regions.

The kinetic energy equation is

$$\frac{\partial(\rho\kappa)}{\partial t} + \frac{\partial}{\partial x_j}\left[\rho u_j \kappa - (\mu + \sigma_k \mu_t)\frac{\partial \kappa}{\partial x_j}\right] = \tau_{tij} S_{ij} - \beta^* \rho\omega\kappa + \varphi_k \qquad (4.10)$$

and equation involving turbulence frequency is

$$\frac{\partial(\rho\omega)}{\partial t} + \frac{\partial}{\partial x_j}\left[\rho u_j \omega - (\mu + \sigma_\omega \mu_t)\frac{\partial \omega}{\partial x_j}\right] = P_\omega - \beta\rho\omega^2 + 2(1 - F_1)\frac{\rho\sigma_\omega}{\omega}\frac{\partial \kappa}{\partial x_j}\frac{\partial \omega}{\partial x_j} \quad (4.11)$$

in which the eddy viscosity is defined in terms of turbulent kinetic energy κ and specific dissipation rate of turbulent frequency ω. The F_1 is a weight function between two combined models and

$$P_\omega = 2\gamma\rho(S_{ij} - \omega\, S_{nn}\delta_{ij}/3) \approx \gamma\rho\Omega^2 \quad (4.12)$$

which is the approximated absolute value of vorticity. The model constants β^*= 0.09 and κ = 0. Remaining $\beta, \gamma, \sigma_\kappa, \sigma_\omega$ are found using the weight function φ such as

$$\varphi = F_1\varphi_1 + (1 - F_1)\varphi_2 \quad (4.13)$$

where φ stands for each of the sought coefficient symbols.

4.3 Computational model

4.3.1 Model overview

In the numerical solution process of RANS equations two different codes were used, Fluent [83] and OpenFOAM [84]. Fluent, however, did not exhibit good computational performance and during the research a switch was made to OpenFOAM, which showed improved performance and control over the model. In general, explicit time schemes were avoided due to their instability. The second-order implicit differencing scheme was used with upwind flux-difference method. The size of the maximum time step was limited through simulation stability and numbers of sub-iterations. In OpenFOAM the limit was governed through maximum value of Courant number limit (< 1.0) through the whole computational domain.

4.3.2 Domain and boundary conditions

The domain creation usually starts with its boundary geometry within which the flow solution is obtained. In the next step, the domain is divided into smaller elements, which create control-volumes to which the appropriate set of non-linear algebraic Navier–

Stokes equations are assigned. In the last step preceding the solution, the initial and boundary conditions are assigned.

For each of the simulations, three different domains were tested. All of the domains were two–dimensional. The domain sizes ranged from 35,000 to 1,200,000 cells, where consecutive refinements of the basic mesh were in the range between those numbers. The latter number was for the most refined mesh.

Every domain had to be refined along the boundary portion in order to capture boundary layer effects. Additionally, the meshes along the portion of the interface between water and air had to be refined to assure proper interface formation. It was especially demanding task for the full size meshes, which required quite significant refinements.

The meshes were created with such accuracy that the same grids were used among different turbulence models. Because of the high pressure fluctuations during the fluid impact upon the wall [38, 39], the level of grid refinement along the instrumented part was quite significant.

The following boundary conditions were assigned:

- inlet – a constant velocity at the inlet boundary with zero pressure gradient,
- outlet – a fixed pressure boundary with zero velocity gradient was used,
- wall – a no-slip wall boundary condition; the velocity of the fluid at the wall equals to the velocity of the wall (zero) with pressure gradient equal zero gradient; same boundary condition was used to model moving wall section.

A sample domain with all the boundaries is shown in Figure 4.1.

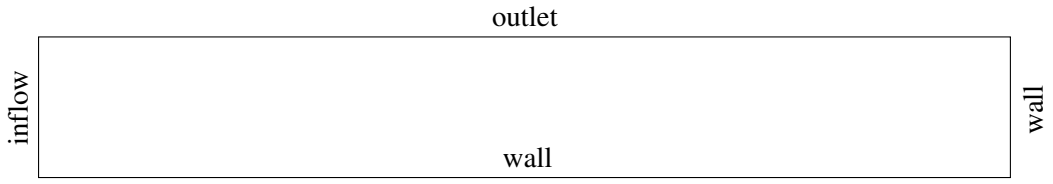

Figure 4.1. Boundaries.

4.3.3 Tsunami bore generation

Different methods of bore formation were investigated. In the following sections, three methods are described. The first method involved a wave paddle, which mimicked the wave paddle used in the experiments [73-75, 85]. The second method involved constant velocity and bore height inflow boundary condition. The last approach utilized well-known dam break scenario [6, 25, 27-29, 71, 86]. The validity of each model was based on its ability to predict the approaching bore height, its velocity magnitude, and vertical wall force time histories.

4.3.3.1 Wave paddle model

To reproduce the results of the experimentally tested conditions, a wave tank model was created. The Tsunami Wave Basin (TWB) described in [69] was used, Figure 4.2. A solitary wave model is frequently used to model a tsunami wave. Here, the Goring and Raichlen wave-maker theory [85] adapted by Hughes [87] was used. The same wave generating paddle functions were used at the TWB facility. For this model, Fluent was used for the numerical simulation.

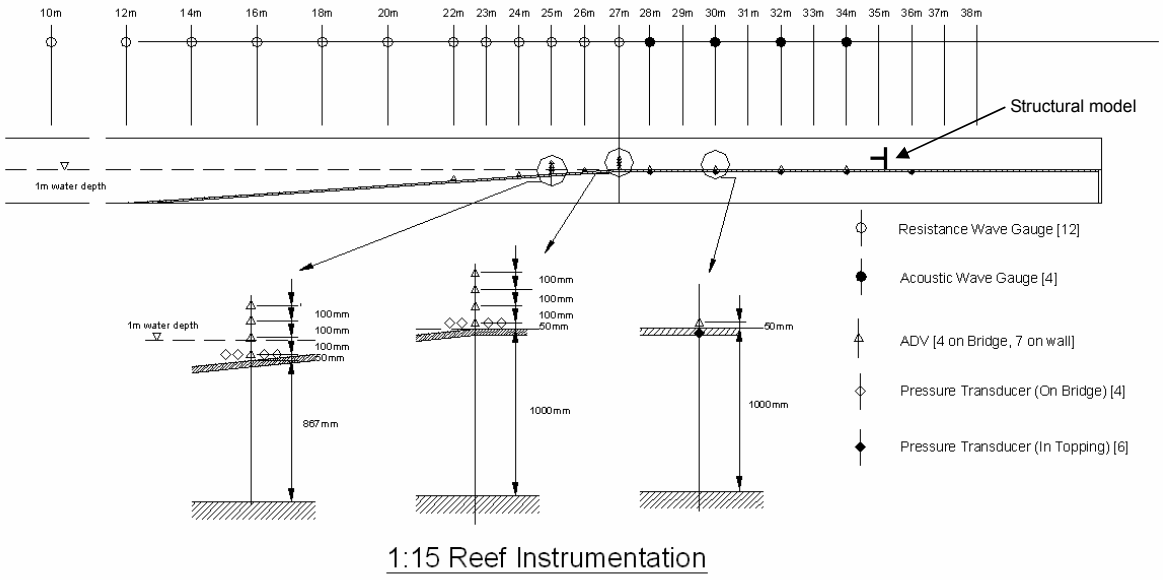

Figure 4.2. TWB beach slope and fringing reef with instrumentation.

In the wave paddle formulation [85] it is assumed beneath long waves the horizontal velocities are constant, therefore the velocity vector $u(x,z,t) \approx \bar{u}(x,t)$, where $\bar{u}$ stands for the average water velocity. Comparing averaged water particle velocity at the wave-maker board surface to wave board speed, it is possible to obtain the wave board displacement function

$$\frac{dX_0(t)}{dt} = \bar{u}(X_0,t) \tag{4.14}$$

where $X_0(t)$ denotes wavemaker displacement and $\bar{u}(X_0,t)$ is given as

$$\bar{u}(X_0,t) = \frac{C\,\eta(X_0,t)}{d+\eta(X_0,t)} \tag{4.15}$$

in which c is wave celerity, $\eta(x,t)$ is the water wave surface elevation, and d represents still water depth. For $x=X_0$, which is the position of the moving wave board, it was assumed the surface elevation might be represented by a wave height and phase angle function $\Phi = \kappa(Ct - X_0)$, which defines

$$\eta_0(X_0,t) = Hf(\Phi) \tag{4.16}$$

Substitution into equation (4.15) results in the wave paddle velocity

$$\frac{dX_0(t)}{dt} = \frac{C\,Hf(\Phi)}{d+Hf(\Phi)} \tag{4.17}$$

The solitary wave profile is given over the time range between $-\infty$ and ∞ as

$$\eta(x,t) = H\,sech^2(\Phi) \tag{4.18}$$

where

$$\kappa = \sqrt{\frac{3H}{4d^3}} \tag{4.19}$$

and

$$C = \sqrt{g(d+H)} \tag{4.20}$$

For solitary wave the function in equation (4.17) is $f(\Phi) = \mathrm{sech}^2(\Phi)$, which substituted into implicit wave equation results in

$$X_0(t) = \frac{H}{\kappa d} tanh(\Phi) \tag{4.21}$$

Using Newton iteration, the time-dependent wave board trajectory is obtained, which after necessary operations the iterative equation for paddle displacement is obtained as

$$X_0^{i+1} = X_0^i - \frac{X_0^i - \frac{H}{\kappa d} tanh\left[\ \kappa(Ct - X_0^i)\right]}{1 + \frac{H}{d} sech^2\left[\kappa(Ct - X_0^i)\right]} \tag{4.22}$$

From the above relations, two important properties can be derived: the maximum and minimum paddle displacement is

$$S = \sqrt{\frac{16\,Hd}{3}} \tag{4.23}$$

and time stroke duration is

$$t_f \approx \frac{1}{\kappa C}\left(3.8 + \frac{H}{d}\right) \tag{4.24}$$

The dimensions of the computational domain were the same as TWB. The wave paddle movement in the form of User Defined Function (UDF) was applied to 1.0 [m] water depth and 0.2 m wave height with paddle movement. Figure 4.3 shows comparison and the overlap between the three different wave paddle routines.

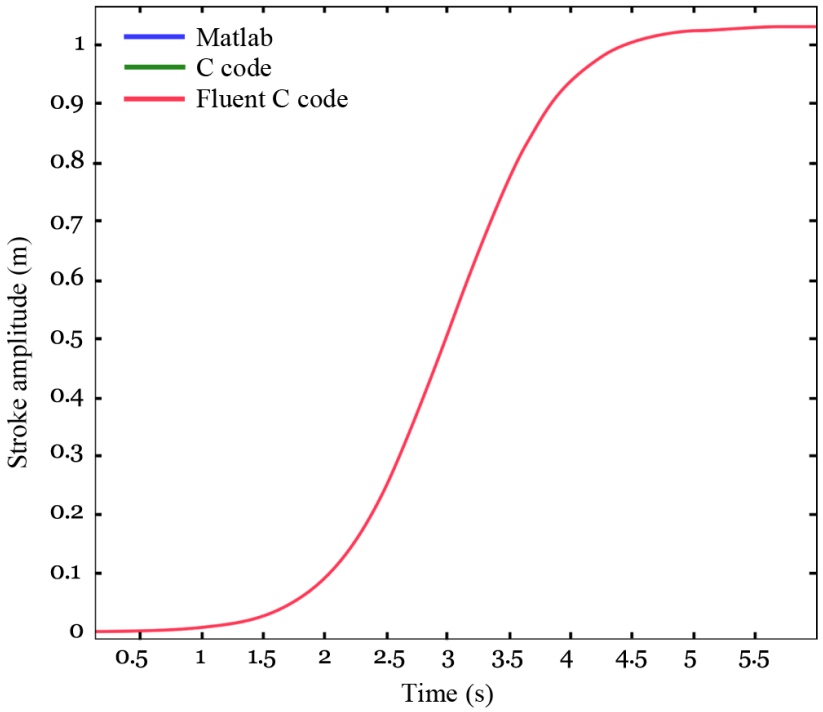

Figure 4.3. Wave paddle movement for wave height 0.2 (m) and water depth 1.0 (m). Overlapping results for three different codes: Matlab, C, and Fluent C routine.

4.3.3.2 Constant velocity inflow

Based on the assumption of shallow water wave theory, which states the velocity along the flow height is constant, similar to [85], and in order to save computational time the domain size was reduced from Figure 4.4 to Figure 4.5, by removing the deep offshore and sloping beach parts, leaving the reef part, on top of which the developed tsunami bore traveled towards the instrumented structure. The two quantities that matter the most in this case are the bore height and velocity. Assuming they can be modeled properly, the same forces upon the structure under impact should be obtained as in the case of a bore generated by the wave paddle.

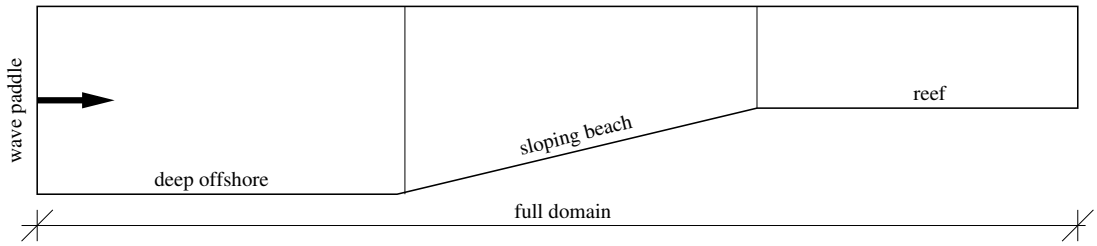

Figure 4.4. Full size domain with three sections.

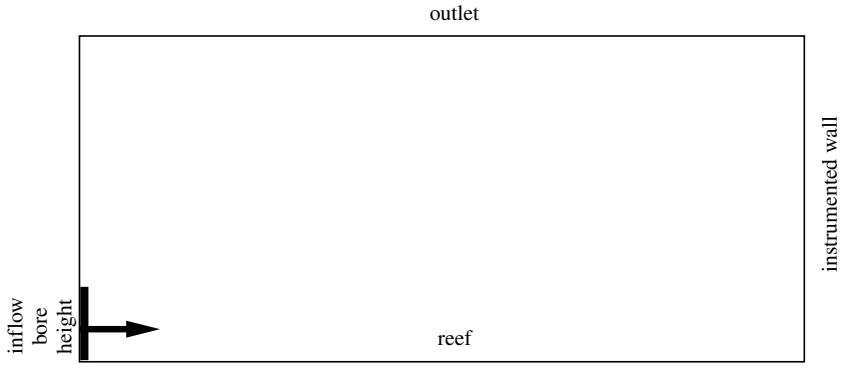

Figure 4.5. Reduced domain, the flat reef portion of the full domain with bore inflow boundary condition, which represents projected incoming bore height.

4.3.3.3 Dam break

In the literature [6, 25, 27-29, 71], a popular method to generate a broken tsunami flow is a dam break. In this work a domain of required size was also created with appropriate length and height to sustain a long lasting bore flow. To generate the desired bore height the necessary dam height had to be defined, which was obtained from the hydraulic jump theory described in [71, 86].

4.4 Results

4.4.1 Overview

In this section, the results for the three approaches to generate bores discussed in section 4.3.3 are presented. The approaches are: the breaking of a solitary wave, a constant inflow velocity boundary, and a dam break. Calculated water flow characteristics and loads are presented and discussed.

4.4.2 Tsunami Wave Basin (TWB) domain with solitary wave break

The full domain resembled the experimental configuration used in TWB. The original tests were performed in 2.16 m wide flume channel with 1:5 and 1:15 beach slopes in the mid section, Figure 4.2 and Figure 4.4. The computational model was defined in two-dimensional space. Therefore, all the results were calculated for a unit tank width. The computational model involved numerically defined wave paddle, which was implemented through dynamic mesh update technique with a cell collapse method along the paddle boundary. While the wave paddle moved, it crossed neighboring cell volumes. To eliminate numerical grid errors, cell shapes had to adapt as the paddle was shrinking their volume, finally, causing their collapse and elimination from the computational domain. The reef portion over which the bore propagated was flat. The generated incoming solitary wave broke at the end of the beach slope and transformed into a turbulent bore, which propagated along the flat reef and impacted the structural wall. The location of the wall was 35 meters from the paddle.

4.4.2.1 Wave paddle movement routine and domain response

To eliminate possible errors the influence of the height of the computational domain was tested. The paddle movement was tested with turbulent κ - ε model. In this test, the full tank domain was reduced; it only included deep offshore part. A solitary wave of 0.2 m in height was modeled with 1 m standing water. Two domains were tested: one with a height equal to the wave paddle height of 3 m, and the second with the height of three times the paddle height. As expected, until the time instance at which the wave breaking occurred, the results were similar to the theoretical values. Both models generated similar solitary wave characteristics, with similar wave height, Figure 4.6, and wave travel

velocities, Figure 4.7 and Figure 4.8. The domain height did not have any significant influence on the solitary wave formation using moving mesh technique. In smaller domain, there were some field velocity differences with increased air velocities, however, without any significant effect on the water volume. These differences were expected. No visible pressure buildup effects were visible, Figure 4.9. It was concluded that it is acceptable to model the wave tank with a height equal to the level of the expected wave or bore height. The benefit is a reduced computational effort because of the smaller domain.

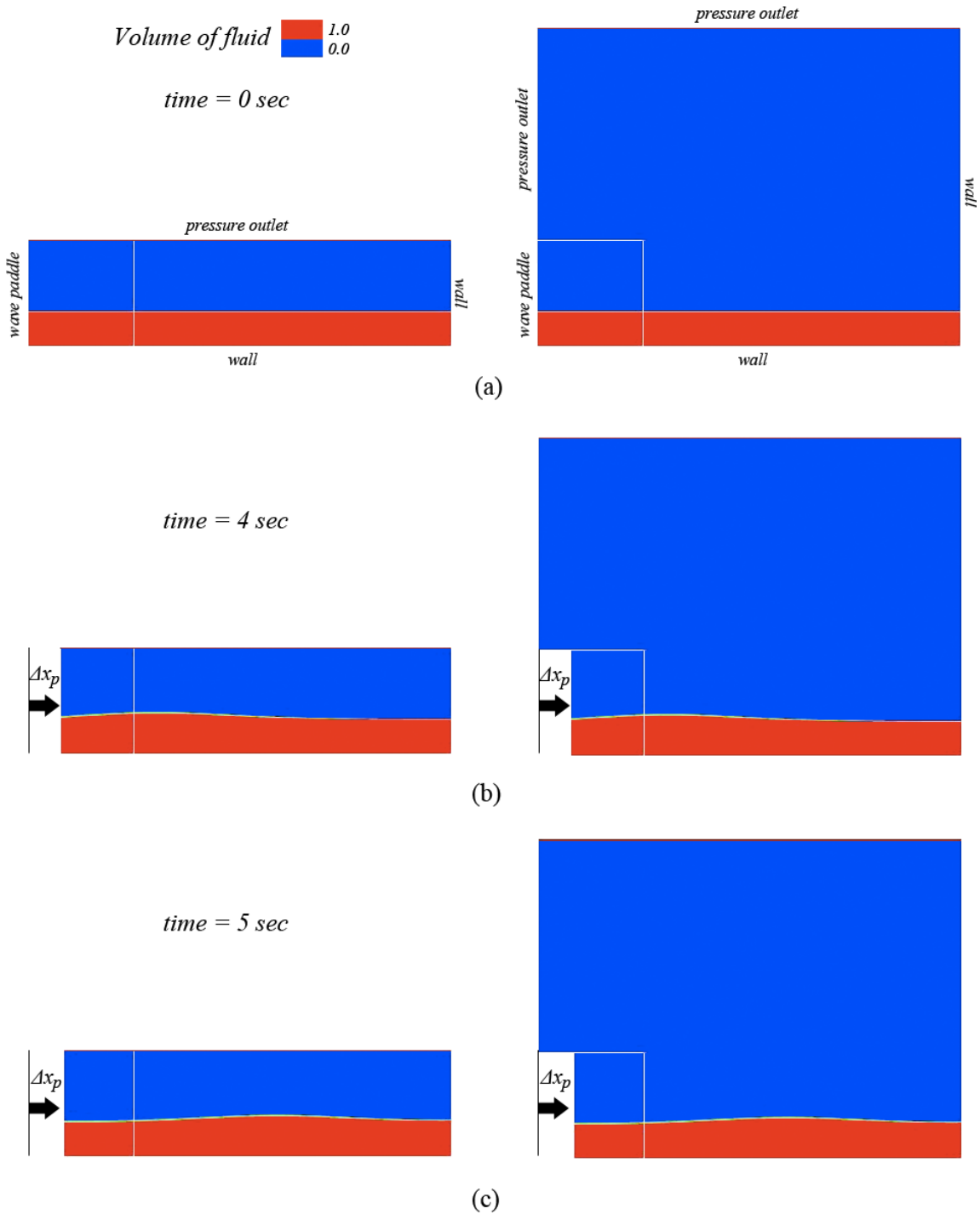

Figure 4.6. 3 m and 9 m high tanks: wave paddle movement and 20 cm solitary wave development; (a) at 0 sec time, boundary conditions are indicated; (b) at 4 sec time; (c) at 5 sec time, fully developed wave form.

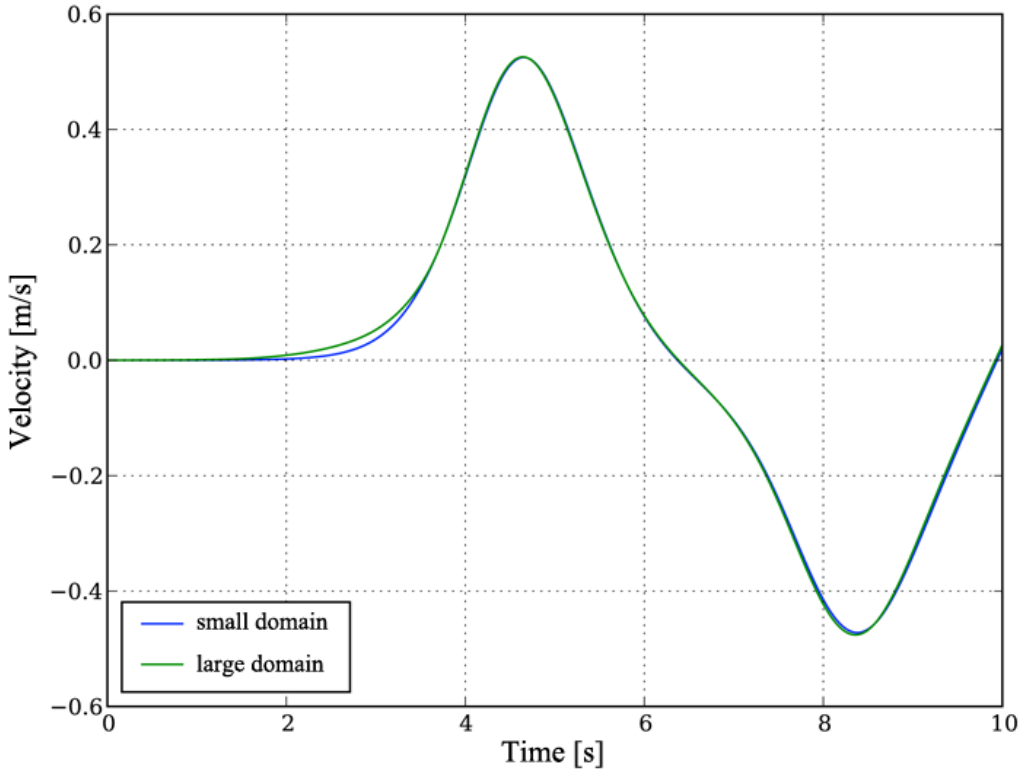

Figure 4.7. Average velocity time-history over the height of the probing line at x = 6 m and y = 0 – 1.2 m; x defines length of the tank starting from the paddle and y defines the height of the tank from its bottom; The negative velocity results from wave reflection from the end wall and wave return.

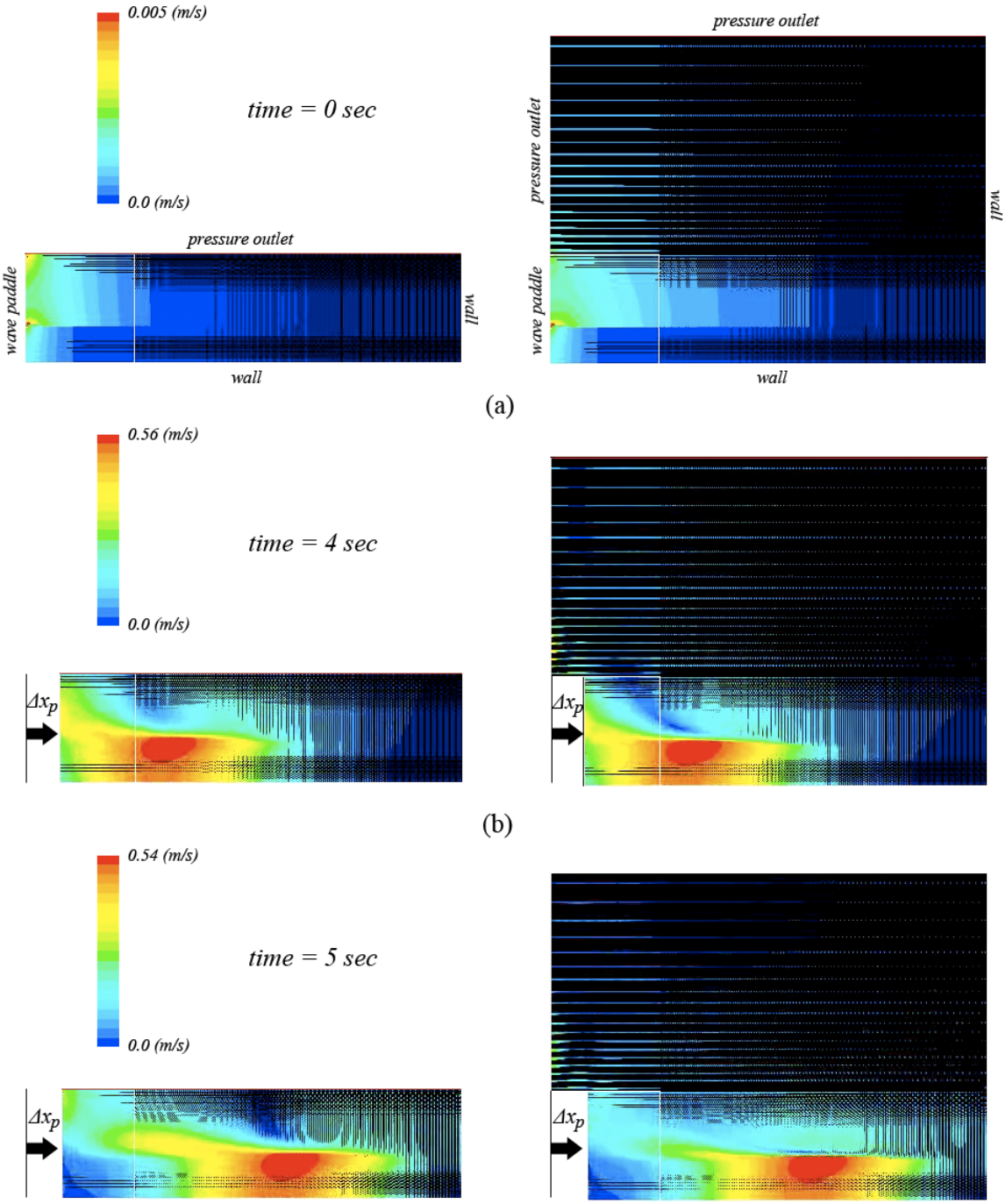

Figure 4.8. Velocity profiles corresponding to Figure 4.6; black color indicates domain cells; (a) at 0.04 sec time, boundary conditions are indicated; (b) at 4 sec time; (c) at 5 sec time, fully developed wave form.

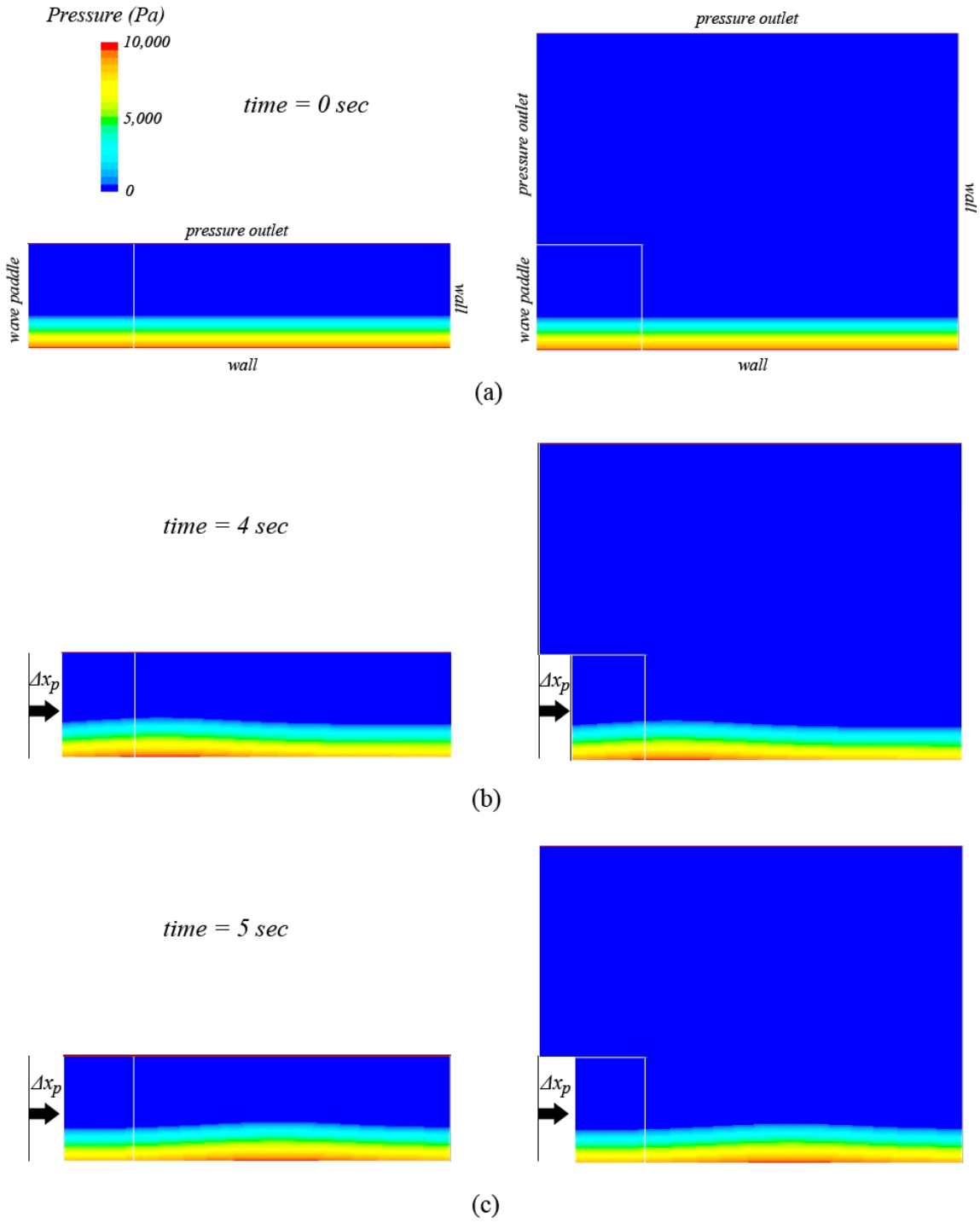

Figure 4.9. Pressure distribution in Figure 4.6; (a) at 0 sec time, boundary conditions are indicated; (b) at 4 sec time; (c) at 5 sec time, fully developed wave form.

4.4.2.2 Full TWB tank computational domain

From the TWB experimental results [69], only two wave heights were investigated, 20 and 40 cm solitary waves. Sixty centimeter waves were not simulated because the bore impact resulted in overtopping of the instrumented wall and therefore the recorded loads were likely incomplete. Two initial water levels were used, dry-bed (no standing water, 1 m from the bottom of the tank) and wet-bed (10 cm standing water, 1.1 m from the bottom of the tank). Two beach slopes were used, 1:5 and 1:15. The example of 1:5 computational domain is presented in Figure 4.10. On the left side of the tank the wave paddle movement zone is indicated, which was separated from the rest of the domain with an interface. Interface was used to limit the mesh deformation to the wave paddle portion of the tank, so not the whole grid is compressed at each time step. The interface is a surface or line between two interconnected smaller domains, i.e. paddle movement area and full tank domain. Computational tests showed the use of an interface in Fluent has an effect on overall results; computational quantities in order to be transferred from one side of the interface to the other require additional update routine. However, in terms of one-dimensional water volume propagation (solitary wave moving to the right) does not affect the wave formation, therefore, it is assumed correct to be used. One of the disadvantages of using an interface is that it extends the computational time required to solve the problem.

Figure 4.10. Wave paddle computational grid; 1:5 beach slope with dry-bed.

The paddle movement was imposed in the same way as in the previous section for the small domain. Three different computational grids were used in the simulations, namely: *Base1-I*, *Base1-II*, and *Base1-III*. The mesh at the end of the tank, to the very right, represented the instrumented vertical wall and was refined to capture all of the possible pressure scales, Figure 4.11. The most basic mesh had 101,534 cells. Subsequent meshes represented consecutive refinements. The most refined grid had 826,214 cells. All three

meshes were conformal. The paddle movement zone had a constant cell number grid section.

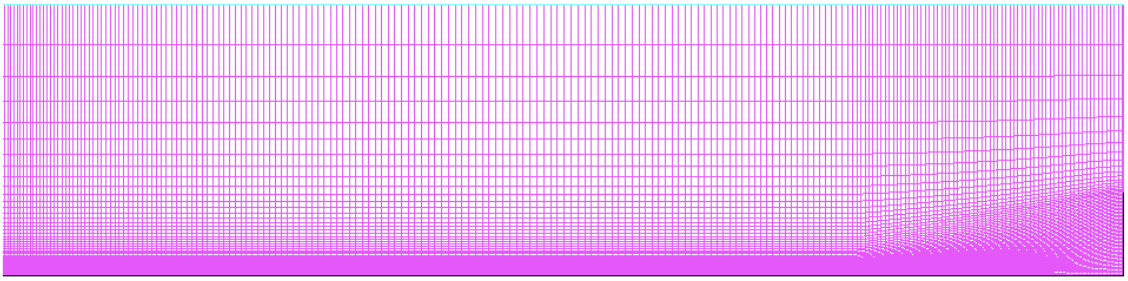

Figure 4.11. Basic computational grid, Base1-I.

Two turbulence models were tested, κ–ε and κ–ω SST. As expected, the wave propagation along the deep offshore portion was the same, there is no turbulence and essentially the same problem is solved. The differences in the models appeared in the beach slope section, where traveling wave energy starts to dissipate due to the frictional effects with non-slip boundary and resulting wave build-up. In the TWB experimental results, for almost every trial, except dry-bed trials for 1:5 beach slope, clear wave breaking was visible. The κ–ε model was not able to reproduce this phenomenon well, despite refined mesh regions around the wave break area, Figure 4.12a–g. For the given tested meshes and obtained results, the κ–ω SST model performed better, Figure 4.12h–n, with visible wave break generation. In κ–ε model, a very smooth wave to bore transition indicates the level of Reynolds averaging must be high. κ–ω SST model was able to capture bore formation well with wave break characteristics as expected. Unfortunately, there was no experimental video recording showing the bore front profile formation; therefore, a direct comparison to computational data was not possible. This leaves the topic open for further research.

Based on the obtained results, in subsequent simulations, the κ–ω SST turbulence model was used.

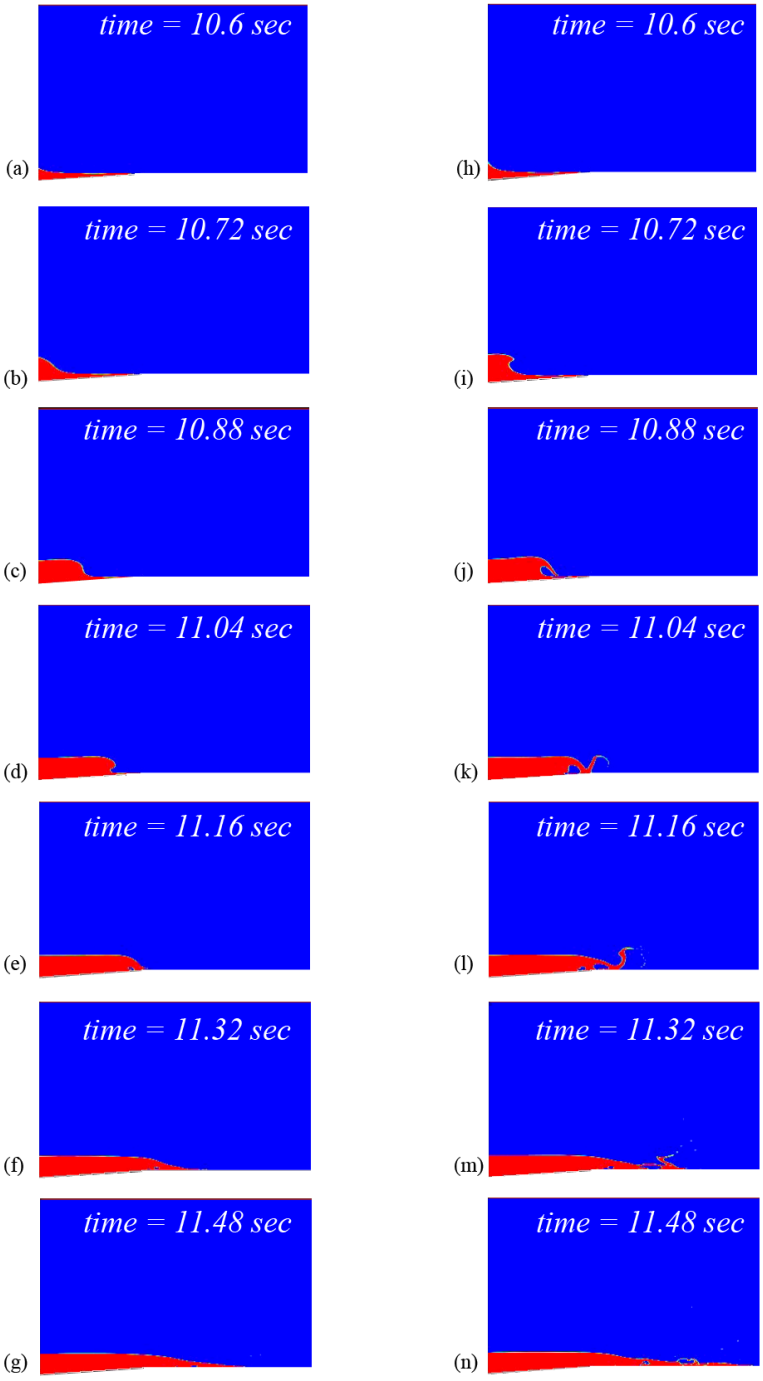

Figure 4.12. Computational model wave break section; dry-bed with 20 cm solitary wave. Figures (a)–(g) represent κ–ε turbulence model. Figures (h)–(n) represent κ–ω SST turbulence model, Base1-III grid.

All of the numerical models for those cases with clear wave break were able to reproduce wave break locations very similar to those observed during the experiments at the transition point between the beach slope and the flat reef portion, Table 4.1 and Table 4.2.

Table 4.1. Wave break location; dry-bed.

Dry-bed (water level 1.00 m)	Beach Slope	1:5 slope		1:15 slope	
	Wave height (m)	Experimental location (m)	Numerical location (m)	Experimental location (m)	Numerical location (m)
	0.2	surge		26.8	25–26
	0.4			24.1	24–25

Table 4.2. Wave break location; wet-bed.

Dry-bed (water level 1.10 m)	Beach Slope	1:5 slope		1:15 slope	
	Wave height (m)	Experimental location (m)	Numerical location (m)	Experimental location (m)	Numerical location (m)
	0.2	22.4	22–23	27.3	26–27
	0.4	22.2	22	25.5	25

The biggest difficulty was a correct modeling of a wave break phenomena, which directly affects bore flow characteristics. As the wave breaking occurred, compressibility effects most likely influence the results [23, 37, 39], resulting in not fully realistic bore formation and further wall impact.

For the available experimental data and numerically tested conditions, it is visible, to accurately model wave breaking a more accurate study is required. Additionally, during the wave breaking, three-dimensional effects might affect the bore development; in the experimental setup, the sides of the flume were constrained with concrete walls. In reality, the air entrapped under the breaking wave is free to escape through the sides of wave. Further study of this phenomenon would be very time consuming and require significant computational resources. This was not the objective of this study, where simple two-dimensional model was investigated.

The numerical velocity time history shape, Figure 4.13, differed from those observed experimentally, Figure 4.14, including maximum and average velocity values, Table 4.3–4.6.

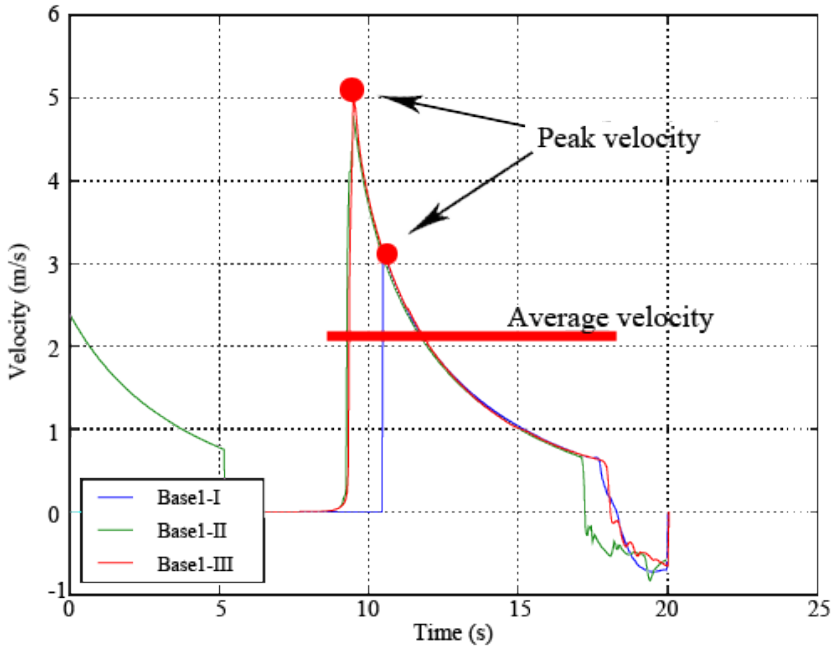

Figure 4.13. Sample recording from the numerical simulation at a test point, x=30 m.

Figure 4.13 depicts velocity measurements read at the sample point, which was placed 2.5 cm above the flat reef level and at 30 m location from the initial wave paddle location. The figure indicates two velocity levels. The peak velocity is the maximum-recorded flow velocity during the bore propagation over the flat reef. The descent velocity is the flow velocity at the middle of the decay of the numerical bore velocity plot. As can be seen, the velocity decayed exponentially.

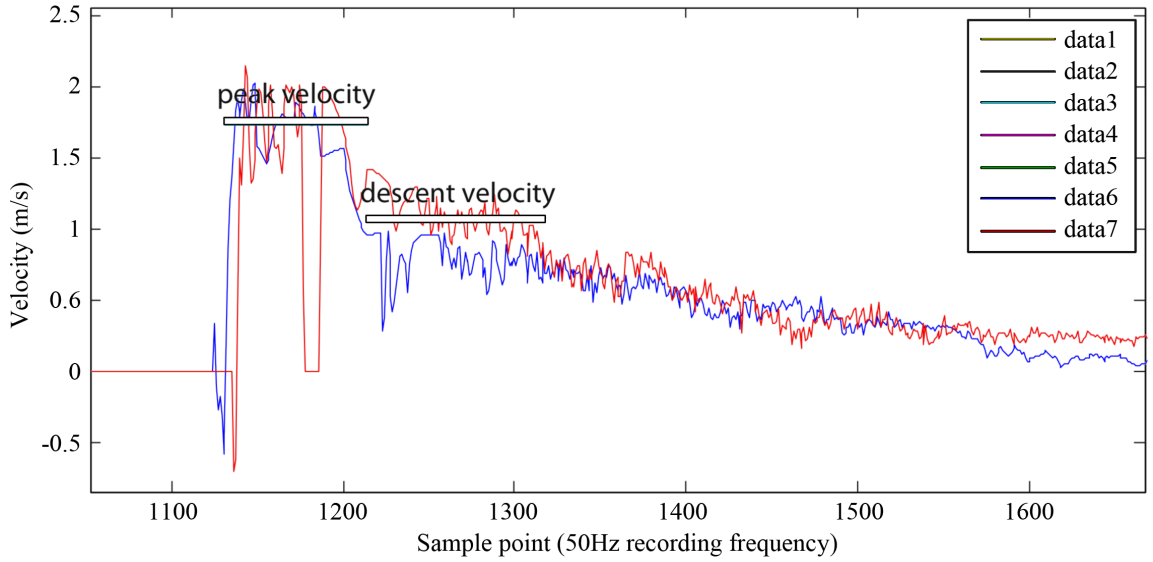

Figure 4.14. Sample experimental ADV measurement from two locations along the flume; for 1:5 slope, ADV @ x_1=27 m and x_2=32 m; for 1:15 slope, ADV @ x_1=30 m and x_2=32 m, i.e. data6 and data7.

Figure 4.14 depicts two samples from different Acoustic Doppler Velocimeter (ADV) measurements during the experiments. The figure indicates two sustained velocity levels, peak velocity and descent velocity. The peak velocity indicates maximum recorded sustained average velocity during the bore propagation over the flat reef. The descent velocity indicates the velocity measured at the bore location right after the leading bore front passed, which is smaller than the peak velocity. Comparing Figure 4.13 to Figure 4.14 it is apparent that the time history shapes differ quite significantly. This indicates the desired bore characteristics were not obtained in the simulations.

Results in Table 4.3–4.6 indicate the smaller the waves the less turbulence occurs. The more the turbulence, larger variation in results was expected. The less turbulence, the more overlap in results. Hence, the consistency of results between different meshes is comparable resulting in very similar velocities (0.2 m waves). The bigger the waves (0.4 m) results start to be less consistent even with highly refined mesh resolutions (>800,000 cells). Such behavior indicates that during the flow a lot of turbulence must occur and the pressure variability scale must be very small. Interestingly, except for the dry-bed, 1:15

slope, Base1-II grid, the numerical peak velocities were approximately 1.7 times the value of the descent average velocities.

Table 4.3. Velocity results comparison between TWB experiments and CFD; dry-bed with 1:5 beach slope.

Dry–bed water level 1.00 m	1:5 slope					
Wave height (m)	Experimental results (m/s)			Numerical results (m/s)		
	Peak velocity	Descent velocity	Average velocity[1]	Grid	Peak velocity	Average velocity
0.2	2.25	1.3	1.9	Base1-I	3.3	1.9
				Base1-II	3.35	1.9
				Base1-III	3.4	1.95
0.4	2.4	1.5	–[2]	Base1-I	3.1	1.88
				Base1-II	4.7	2.7
				Base1-III	5.1	2.9

(1) Average velocity extracted over the length of the bore front, from the very bottom tip of the leading edge to the top of the bore front [71].
(2) Results were not recorded correctly.

Table 4.4. Velocity results comparison between TWB experiments and CFD; dry-bed with 1:15 beach slope.

Dry–bed water level 1.00 m	1:15 slope					
Wave height (m)	Experimental results (m/s)			Numerical results (m/s)		
	Peak velocity	Descent velocity	Average velocity[1]	Grid	Peak velocity	Average velocity
0.2	1.9	1.2	–[2]	Base1-I	5	2.8
				Base1-II	4	2.2
				Base1-III	3.9	2.2
0.4	2.5	1.44	–[2]	Base1-I	–[2]	–[2]
				Base1-II	1.4	1.0
				Base1-III	1.6	1.0

(1) Average velocity extracted over the length of the bore front, from the very bottom tip of the leading edge to the top of the bore front [71].
(2) Results were not recorded.

Table 4.5. Velocity results comparison between TWB experiments and CFD; wet-bed with 1:5 beach slope.

Wet–bed water level 1.10 m	1:5 slope					
Wave height (m)	Experimental results (m/s)			Numerical results (m/s)		
	Peak velocity	Descent velocity	Average velocity[1]	Grid	Peak velocity	Average velocity
0.2	2.1	1.4	2	Base1-I	0.8	0.4
				Base1-II	1.1	0.7
				Base1-III	1.4	0.7
0.4	2.8	1.8	2.2	Base1-I	1.0	0.7
				Base1-II	1.4	0.7
				Base1-III	1.45	0.6

(1) Average velocity extracted over the length of the bore front, from the very bottom tip of the leading edge to the top of the bore front [71].

Table 4.6. Velocity results comparison between TWB experiments and CFD; wet-bed with 1:15 beach slope.

Wet–bed water level 1.10 m	1:15 slope					
Wave height (m)	Experimental results (m/s)			Numerical results (m/s)		
	Peak velocity	Descent velocity	Average velocity[1]	Grid	Peak velocity	Average velocity
0.2	1.8	1.0	–[2]	Base1-I	–[2]	–[2]
				Base1-II	–[2]	–[2]
				Base1-III	1.8	0.9
0.4	2.2	1.65	–[2]	Base1-I	–[2]	–[2]
				Base1-II	1.6	0.9
				Base1-III	2.3	1.4

(1) Average velocity extracted over the length of the bore front, from the very bottom tip of the leading edge to the top of the bore front [71].
(2) Results were not recorded.

In numerical simulations, interesting flow characteristics in terms of fluid velocities were observed in the standing water section during bore propagation over the flat reef. The still water section did not progress with the bore jump velocity, which traveled on top of the still water. Instead, its velocity was between 0 and 50% of the jet of the bore,

Figure 4.15. This indicates and justifies proposed approach in Chapter 3 that the main impact comes from incoming bore jump.

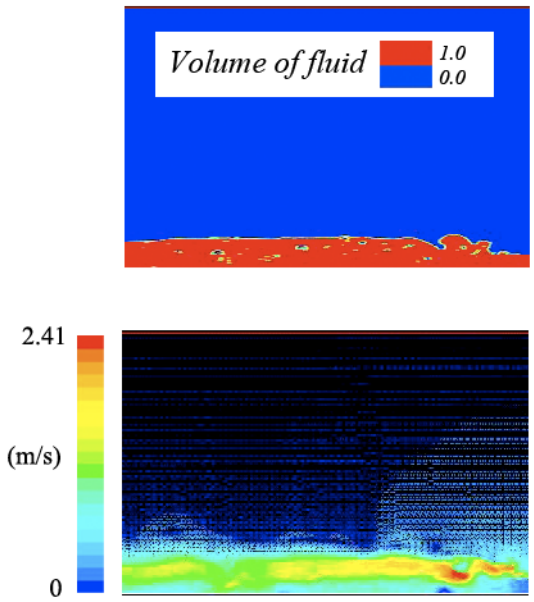

Figure 4.15. Comparison between volume of fluid and domain velocity during the bore flow run along the flat reef portion (10 cm standing water simulation) , Base1-III grid.

As a result of not correctly developed velocities, the measured wall forces did not fully resemble the time histories and maximum measured loads recorded during the experiments.

Similarly, as was done with velocities, a few different sustained force levels could be seen. The peak force indicated the maximum measured force. The shelf force indicated first sustained shelf during the fluid impact plot rise. Upon completion of the water ponding at the wall structure, a small force descent was also observed and was termed the average descent force, Figure 4.16.

Numerical force measurements for different meshes were more consistent than numerical bore velocities. Most of the force plots occurred almost at the same time with very similar force values. However, the forces were different than those in experiments. All the runs for four simulated cases (dry-bed and wet-bed with 20cm, 40cm waves) are presented in Figure 4.17–4.20. The overall results are shown in Table 4.7 and Table 4.8.

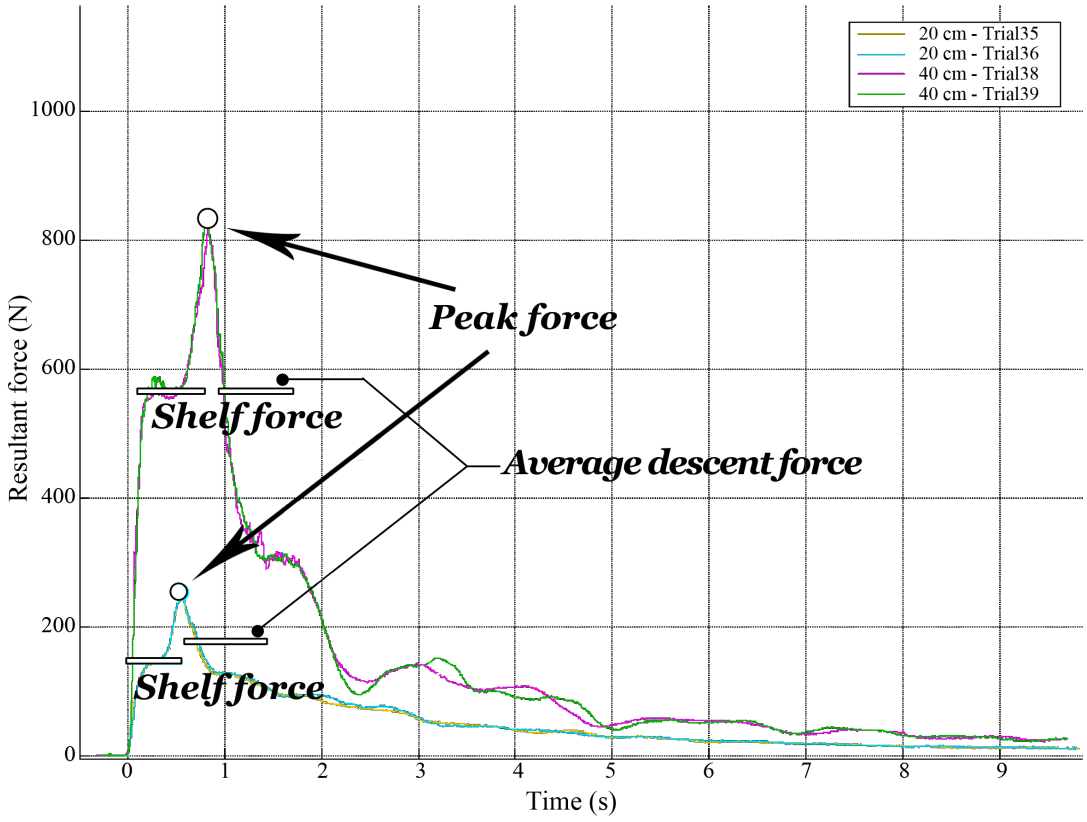

Figure 4.16. TWB experimental wall forces; 20, 40, and 60 cm wave trails, dry-bed.

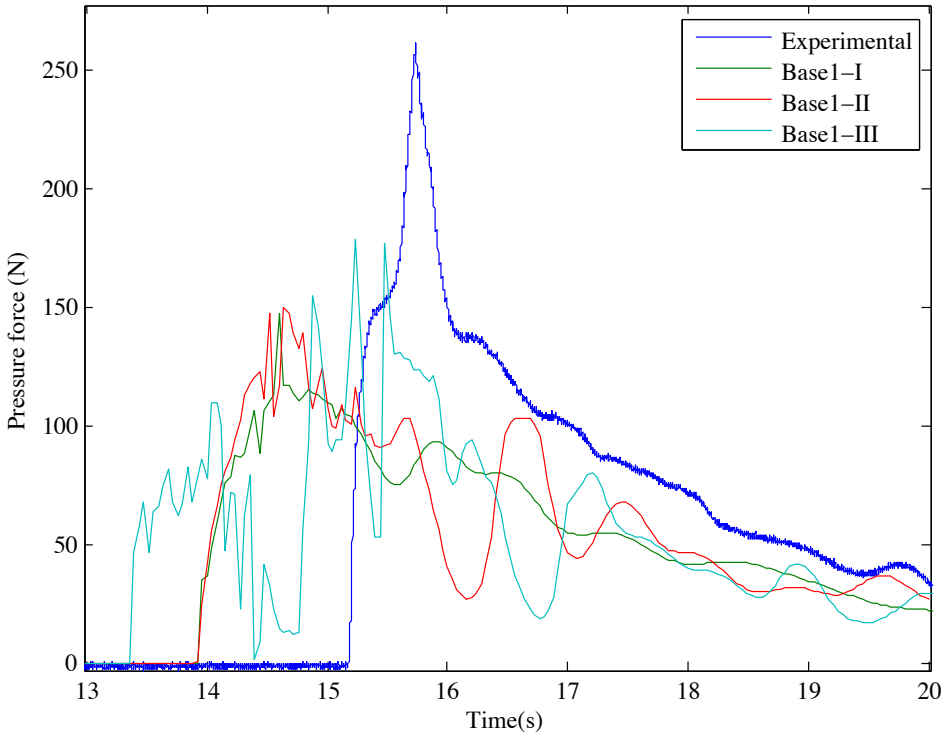

Figure 4.17. Computational TWB domain; dry-bed, 20 cm broken wave.

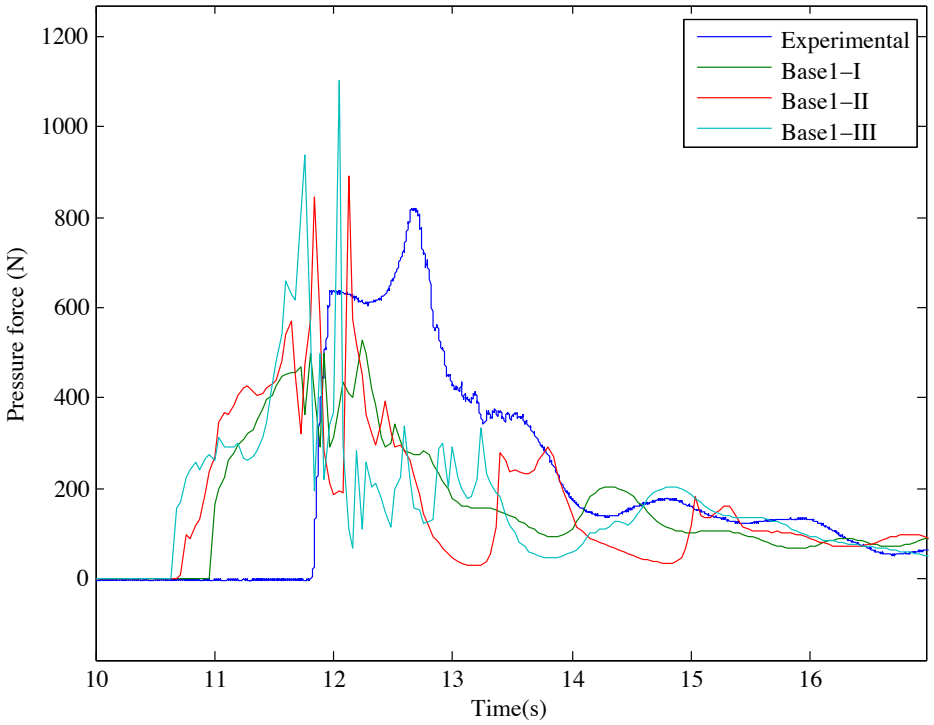

Figure 4.18. Computational TWB domain; dry-bed, 40 cm broken wave.

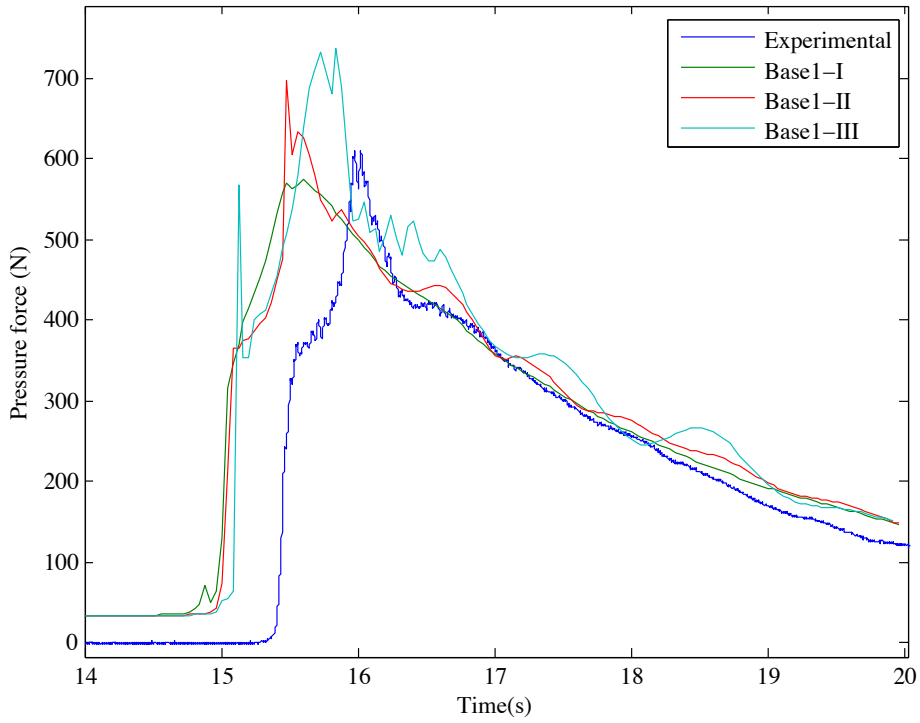

Figure 4.19. Computational TWB domain; wet-bed, 20 cm broken wave.

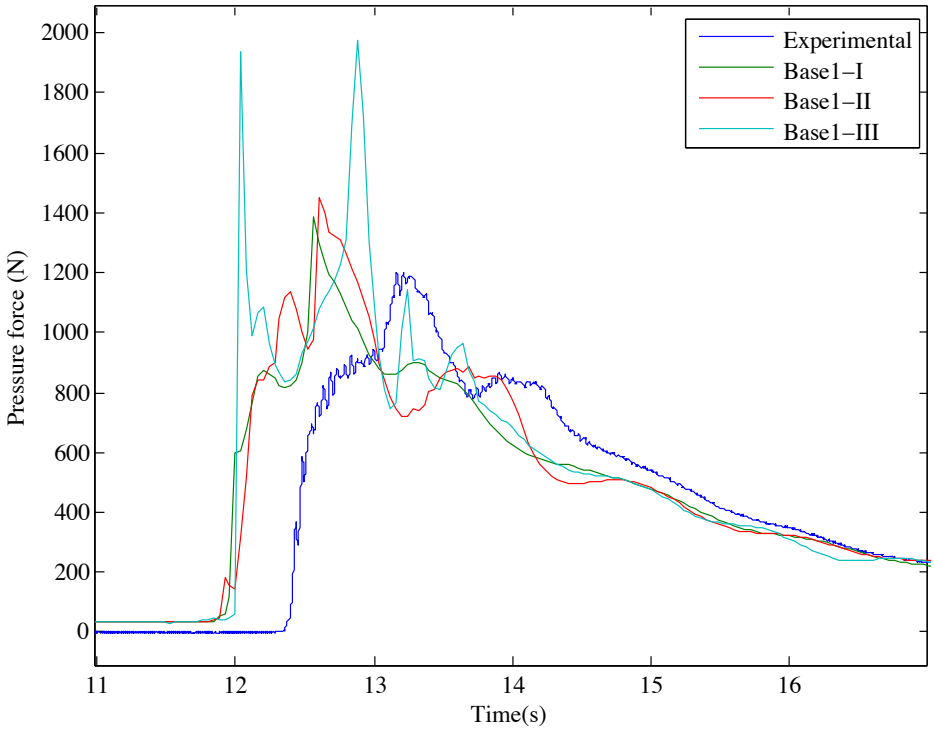

Figure 4.20. Computational TWB domain; wet-bed, 40 cm broken wave.

Table 4.7. Numerical force results, dry-bed with 1:5 slope.

Dry-bed	Experimental results (N)			Numerical results (N)		
Wave height (m)	Peak force	Descent force	Average force	Grid	Peak force	Average force
0.2	250	180	~200	Base1-I	120	70
				Base1-II	150	100
				Base1-III	180	110
0.4	820	585	~580	Base1-I	550	300
				Base1-II	900	400
				Base1-III	1100	550

Table 4.8. Numerical force results, dry-bed with 1:5 slope.

Wet-bed	Experimental results (N)			Numerical results (N)		
Wave height (m)	Peak force	Descent force	Average force	Grid	Peak force	Average force
0.2	610	430	~470	Base1-I	580	365
				Base1-II	700	430
				Base1-III	740	450
0.4	1180	840	~840	Base1-I	1400	750
				Base1-II	1450	750
				Base1-III	2000	800

The full wave breaking with transformation into bore and its progression, followed with wall impingement is presented in Figure 4.21–4.23. Volume of fluid, velocity, and pressure fields are shown, respectively.

4.4.2.3 Wave paddle closure

The modeling process requires multi level consideration. To accurately reproduce experimental flow characteristics and capture small pressure time scales, a very high computational effort is required. It does not only involve extended hardware resources, but also a good software management with multiple parallel software licenses and high grid resolution. Available computational resources with Fluent did not allow achieving the desired task. Nonetheless, a few useful observations were made. A new software package OpenFOAM was adopted and different bore modeling techniques were utilized, which are described in more detail in the next subsections. Results indicate, to reproduce experimental force time-histories, a more refined study is required.

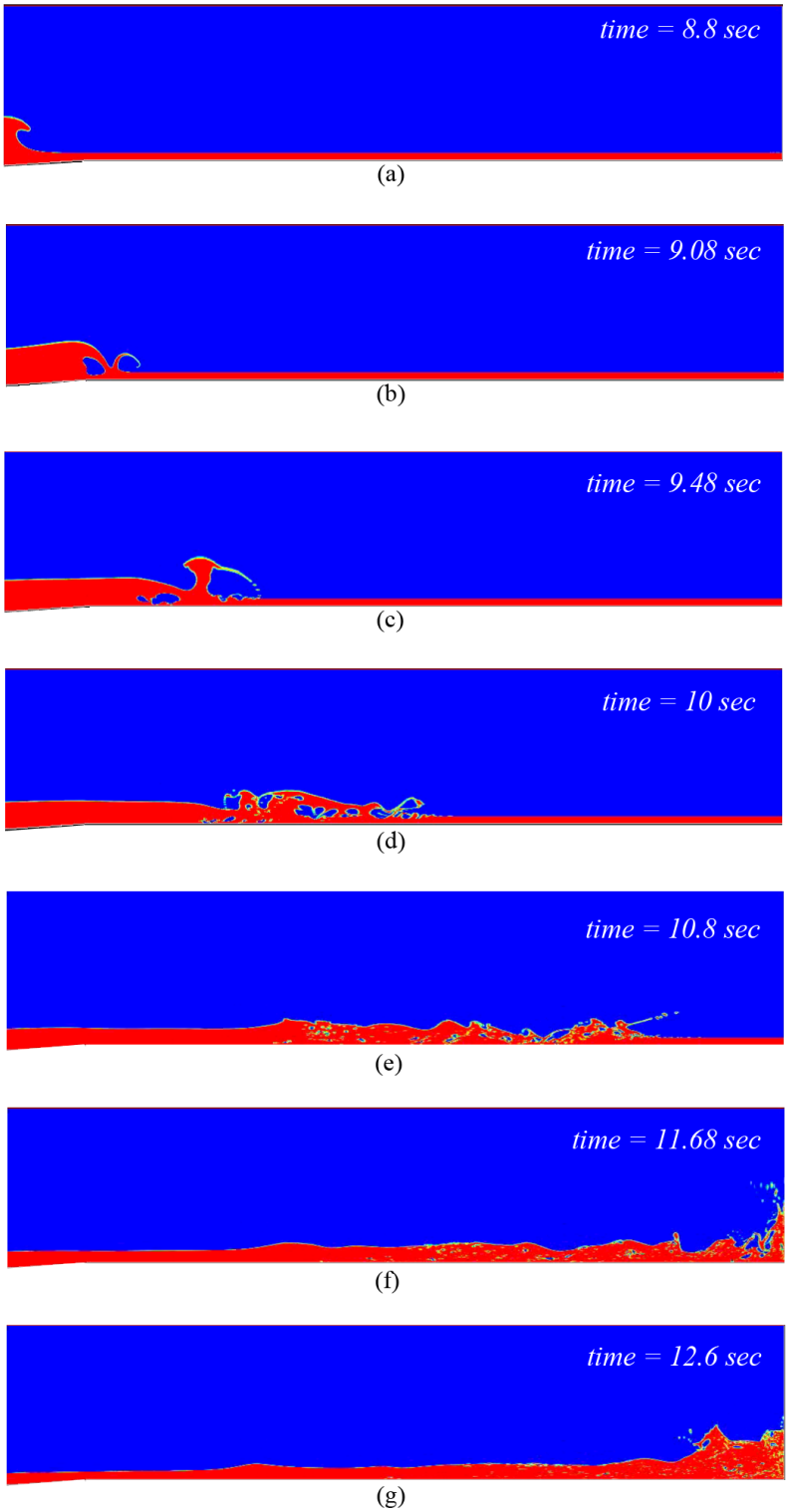

Figure 4.21. TWB computational domain: volume of fluid field; 1.10 m standing water, 40 cm wave, Base1-III grid.

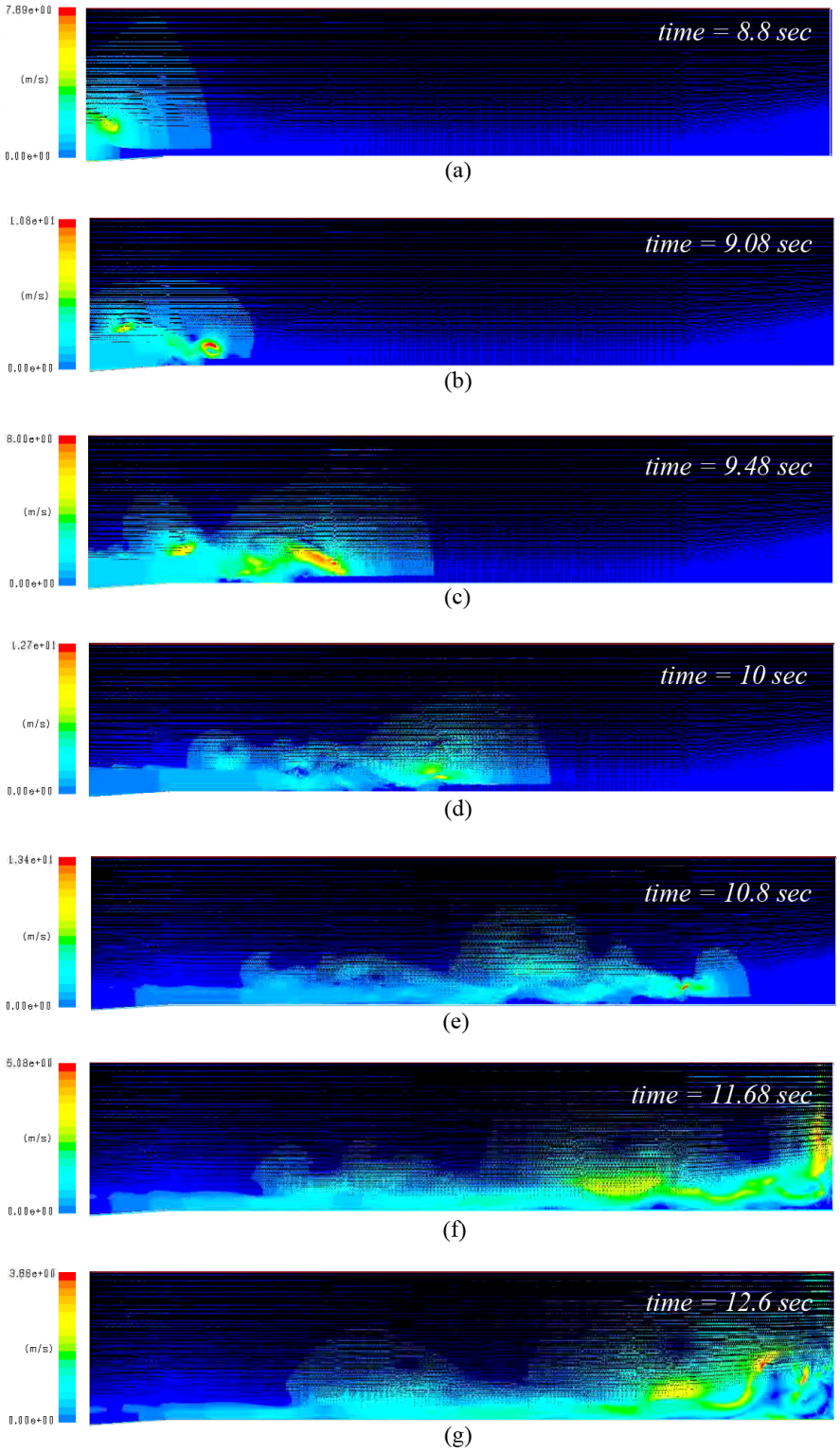

Figure 4.22. Velocity profile (m/s) for Figure 4.21; 1.10 m standing water, 40 cm wave, Base1-III grid.

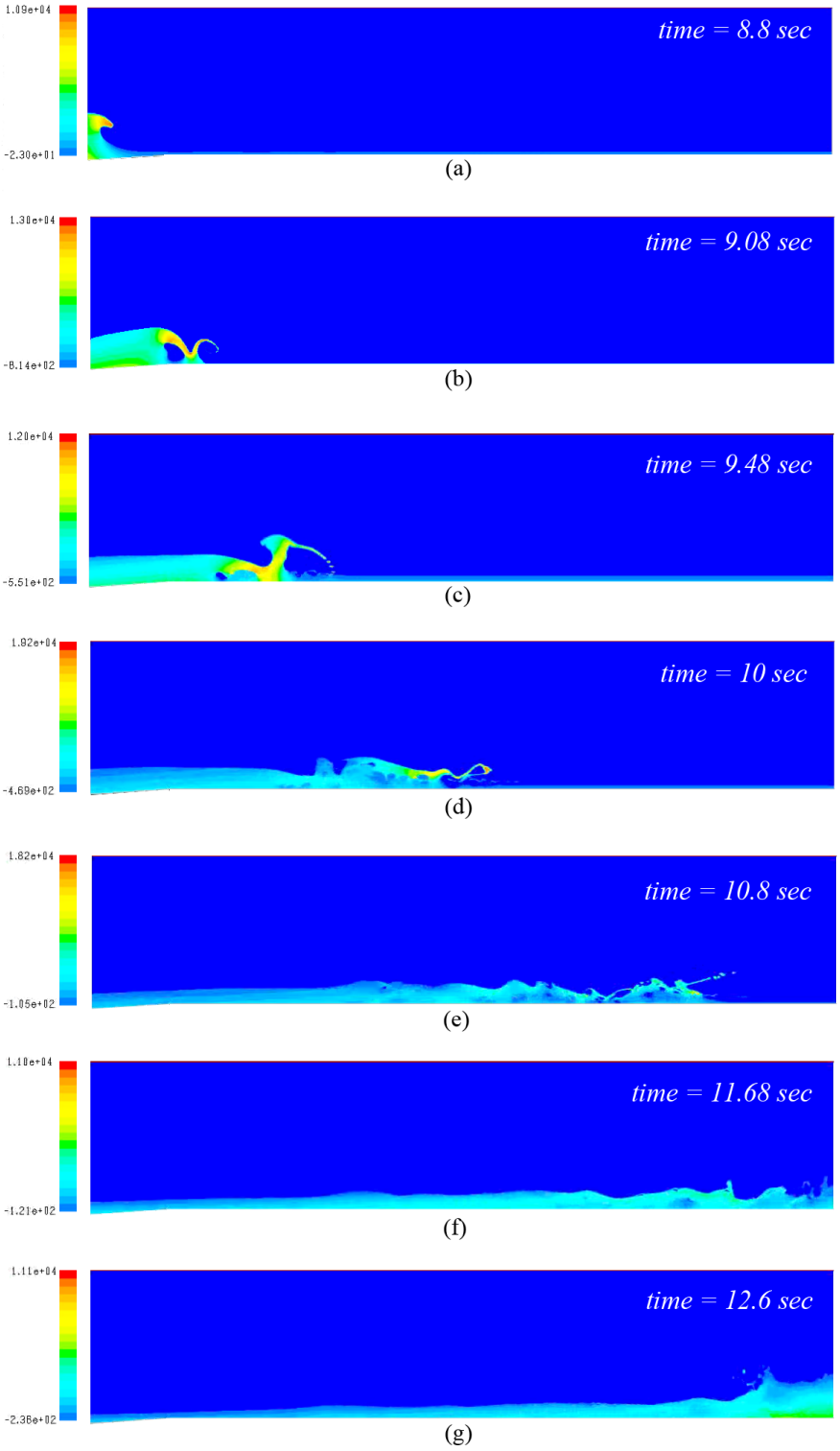

Figure 4.23. Pressure (Pa) distribution for Figure 4.21; 1.10 m standing water, 40 cm wave, Base1-III grid.

4.4.3 Constant inflow boundary

4.4.3.1 Bore generation

Results from the full domain failed to provide good wall force correlation with the experimental data. Fluent's solitary wave model was very computationally demanding and failed to model bore flow correctly. Instead of modeling pre-bore conditions, the domain was simplified to only model the formed bore. The domain was limited to the flat reef portion. The domain was 3 m long and 0.61 m high and represented the end reef section of the experimental flume tested in TWB [69]. The length of the domain was 5 times the height of the instrumented wall. An assumption was made that the simulation starts from the point at which the bore was stabilized. The speed through the depth of the bore was constant and equaled to the average experimental velocity of the bore [71]. The grid consisted of 35,109 elements. All three turbulence models, κ–ε [78, 79], κ–ε RNG [80], and κ–ω SST [81, 82], were tested. Maximum cell aspect ratio was 20 and occurred in cells along the wall boundary (the tank bottom, y=0, and the end wall, x=0, Figure 4.24). Note, the computational domain used in the study had reversed configuration compared to Figure 4.5.

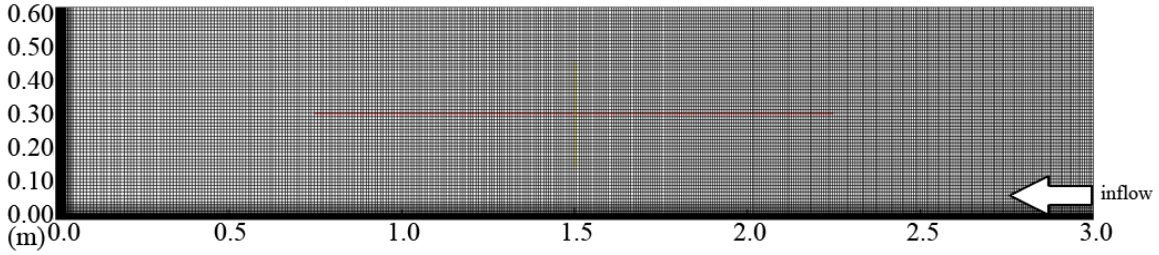

Figure 4.24. Computational TWB small reef domain.

The same domain was tested between two different CFD codes, Fluent and OpenFOAM. To verify the models and limit discrepancies, the explicit solution method was used with a time-step of 0.0001 sec. The time-step was well within the Courant number limit less than 1.0, which for the middle of the domain was approximately 0.021. For each of the turbulence models the simulations used the same mesh and the same boundary conditions. An additional two cases with OpenFOAM included a refined mesh and a decreased time-step, which was 0.00005 sec. Some of the cases in OpenFOAM

were disadvantaged; they were run on the same machine during the same time, therefore thread management slowed the computational process. The overall simulation time was 4 sec. The machine used with Fluent was PC, Intel Core Duo 3.0 GHz. OpenFOAM cases ran on Apple hardware with Mac OS X system and Intel Core2 Duo 2.16 GHz processor. Computational processor time units (CPU) used for the calculations are presented in Table 4.9. The constant inflow velocity was 1.88 m/s, which corresponded to the 0.2 m broken solitary wave in TWB.

Table 4.9. Computation time results.

	Fluent	OpenFOAM
κ–ε	7 days	16 hours
κ–ε RNG	7 days	12 hours
κ–ω *SST*	7 days to reach 3 seconds	11 hours
κ–ω *SST* *Δt=0.00005 sec*	–	22 hours
κ–ω *SST* *140,436 cells*	–	3.5 days = 84 hours

Computational time results indicate advantage of OpenFOAM over Fluent. Computational time results for Fluent exceeded those for OpenFOAM by 10 to 15 times. Similar result for the volume of fluid model with even greater difference (20 times) was observed in [88].

Looking at the force–time histories, all of the Fluent models show the initial fluid impact on the wall occurs approximately at the same time, 1.1 sec, which is not correct, Figure 4.25. The defined inflow velocity was 1.88 m/s, which for 3 m long domain, Figure 4.24, should give approximately initial impact time at 1.6 sec. Also, κ–ε for OpenFOAM did not give a good impact time prediction. However, κ–ω model showed a correct impact time, Figure 4.26. To some extent, the bad result could be blamed on a low mesh resolution. From observed numerical peaks, Fluent's results could be improved increasing sub-iteration number within each time step (20 was used), but this would elongate computational process significantly, which already was long enough, Table 4.9.

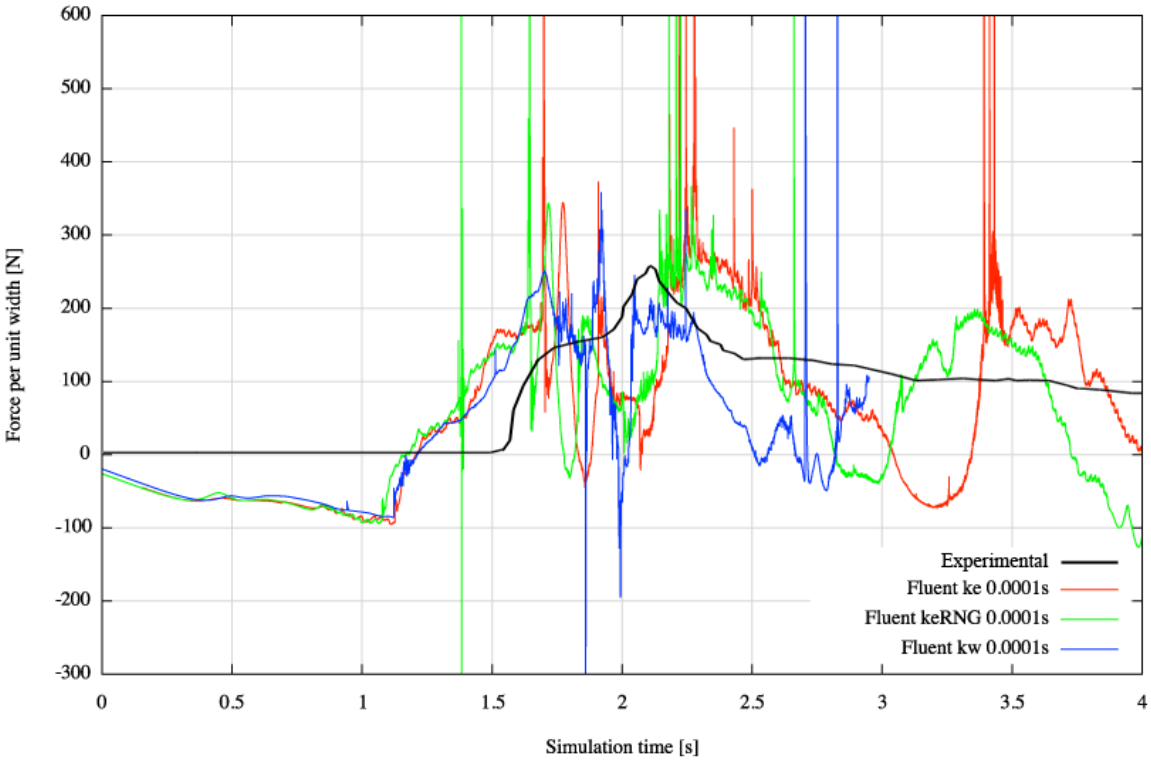

Figure 4.25. Fluent force history measured at the instrumented wall.

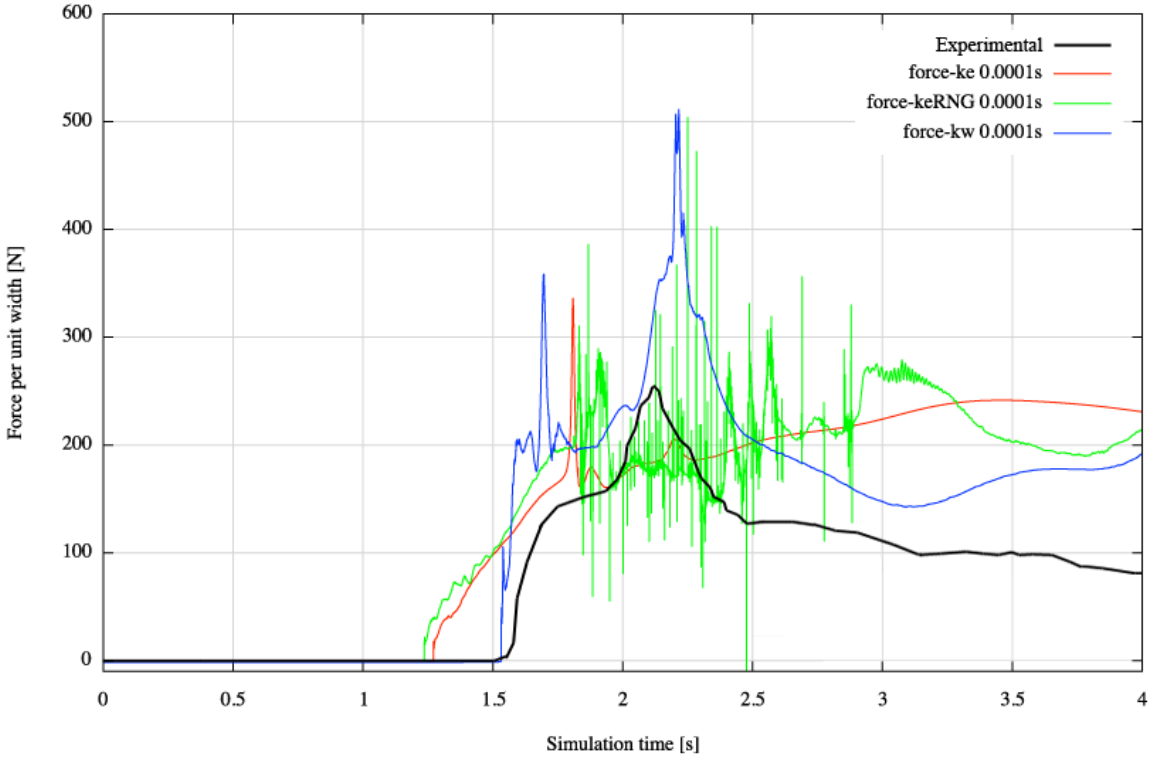

Figure 4.26. OpenFOAM force history measured at the instrumented wall.

All of the κ–ε models showed a large discrepancy in the expected initial force increase observed in the experimental results (Figure 4.2) for 20 cm waves. As the first force peak builds up (time equals approximately 1.7 sec), Figure 4.25–4.26, the water right after the impact collapses back towards the incoming bore flow and reaches a maximum water level next to the wall, Figures 4.32–4.34. This time range should be a good reference for any numerical variation in κ–ε models. Additionally, Fluent models showed quite unrealistic initial negative pressure at the wall surface with additional few negative peaks during the fluid build up, which is clearly incorrect, Figure 4.25. The overall time histories are also not correct. For the constant inflow, no sudden force decrease should be visible as the water kept entering the domain. After the first peak, it was expected the load would drop, as is the case in OpenFOAM results, Figure 4.26, and was also visible in experimental results, Figure 4.16. The model that performed the best was κ–ω SST with OpenFOAM code. It provided relatively smooth force representation and time-history indicating the most probable scenario, Figure 4.26. However, the resulted smooth representation can be a result of relatively coarse mesh resolution. The wall impact occurred approximately around the expected time at 1.5 sec. From all of the simulations, the time-history of the load represents the experimental results (Figure 4.16) most nearly. Nonetheless, the maximum force was overpredicted, 350 N (first peak) compared to 180 N (260 N times 0.7 m width of the experimental wall). Fluent results also indicate that the κ–ε model implementation does not handle the turbulence well, which is indicated through high numerical noise along the recorded time frame after the impact. Mild slopes within both codes, for the κ–ε model, also indicate the formed bore shape must not have been correct, which resulted in a gradual force increase. The other possible source of errors is different volume of fluid implementation in both codes, which describes the liquid phase distribution and defines the interface position between two phases across the finite volumes. Fluent code implementation uses Geo-reconstruct scheme [83], whereas OpenFOAM uses interfaceCompression scheme [84].

Figures 4.27–4.34 show volume of fluid plots of the bore propagation generated through constant inflow boundary and its impact upon the instrumented wall for both of the codes.

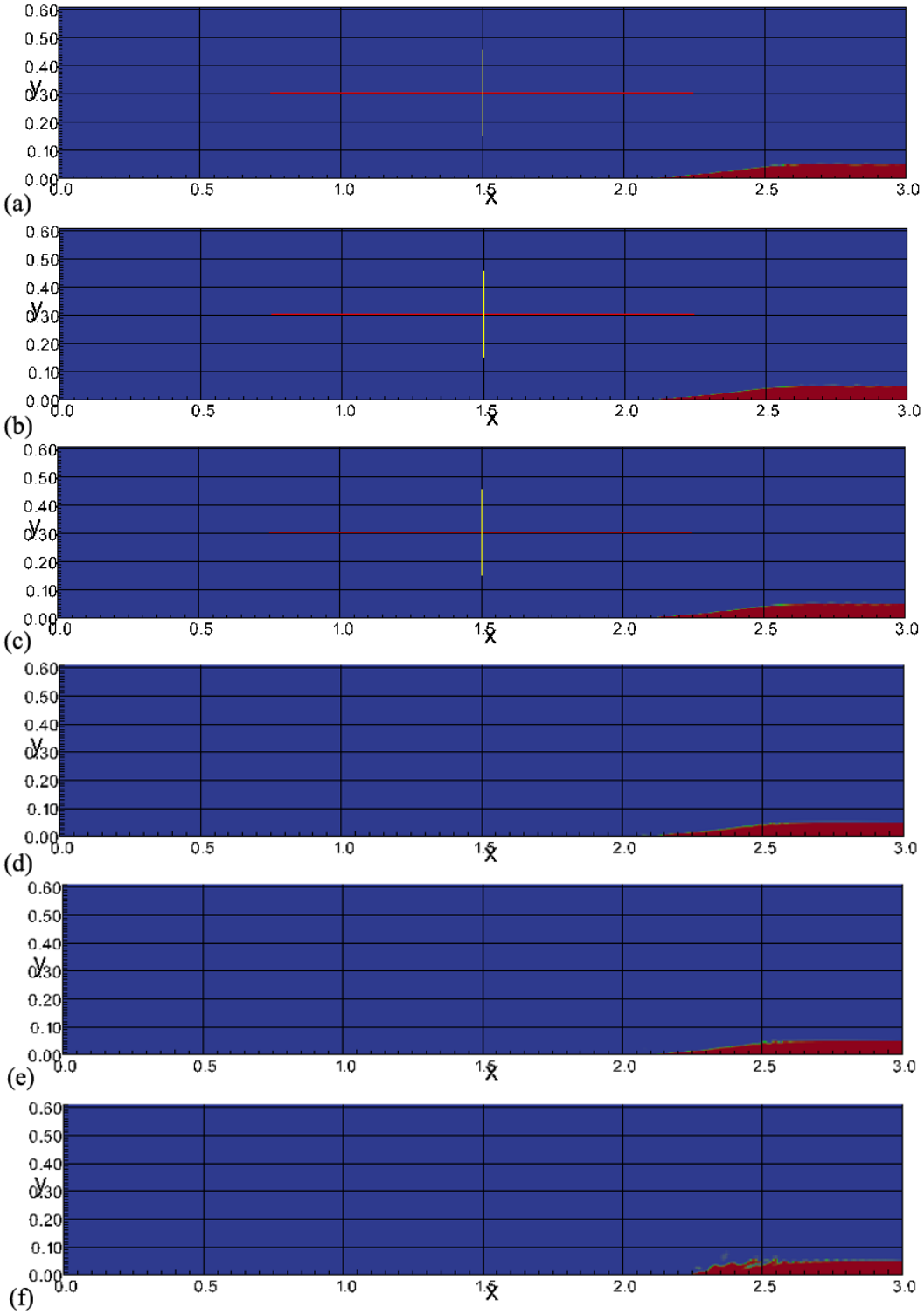

Figure 4.27. Comparison between different numerical models, simulation time 0.35 sec: (a) Fluent κ–ε; (b) Fluent κ–ε RNG; (c) Fluent κ–ω SST; (d) OpenFOAM κ–ε; (e) OpenFOAM κ–ε RNG; (f) OpenFOAM κ–ω SST.

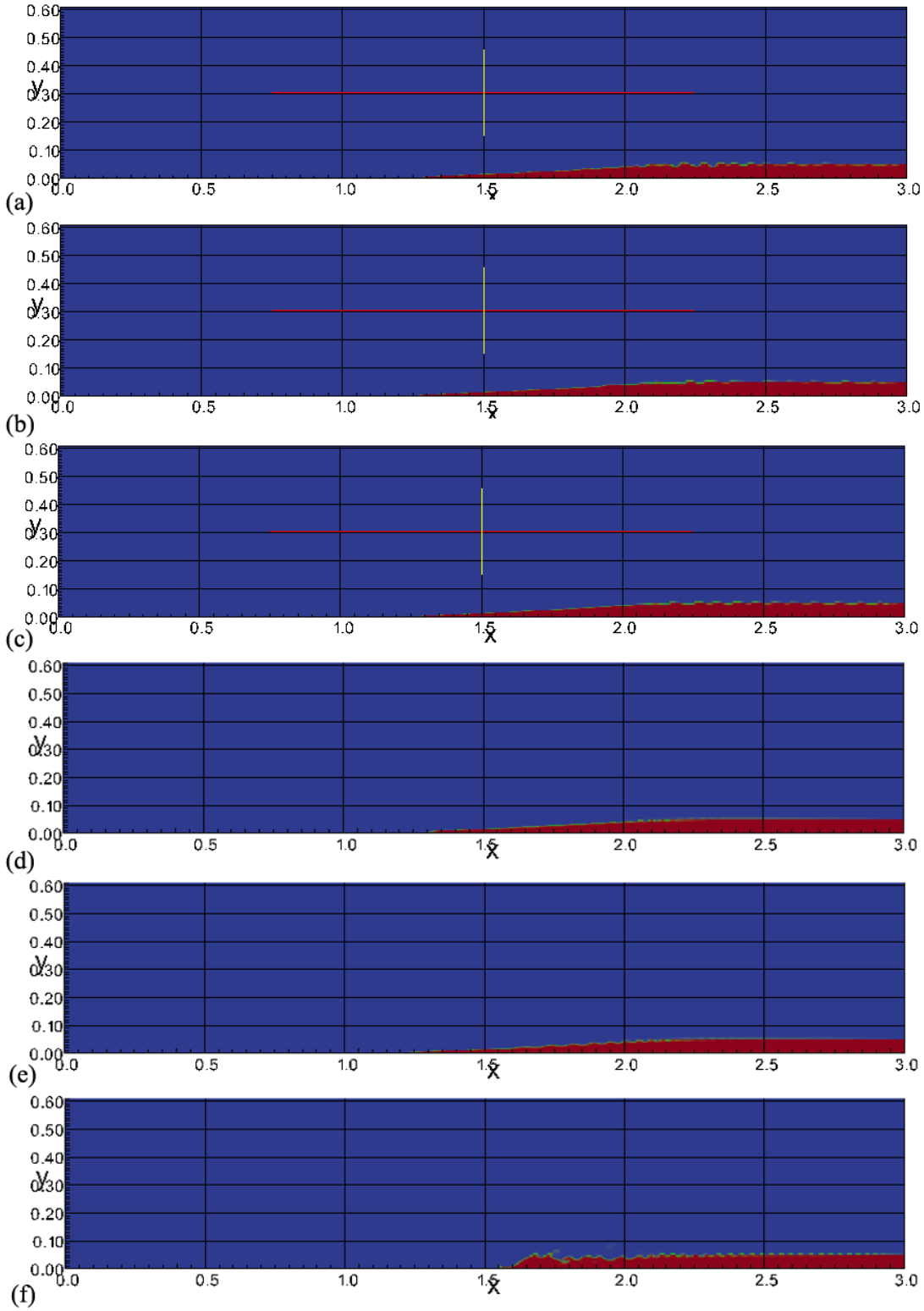

Figure 4.28. Comparison between different numerical models, simulation time 0.7 sec: (a) Fluent κ–ε; (b) Fluent κ–ε RNG; (c) Fluent κ–ω SST; (d) OpenFOAM κ–ε; (e) OpenFOAM κ–ε RNG; (f) OpenFOAM κ–ω SST.

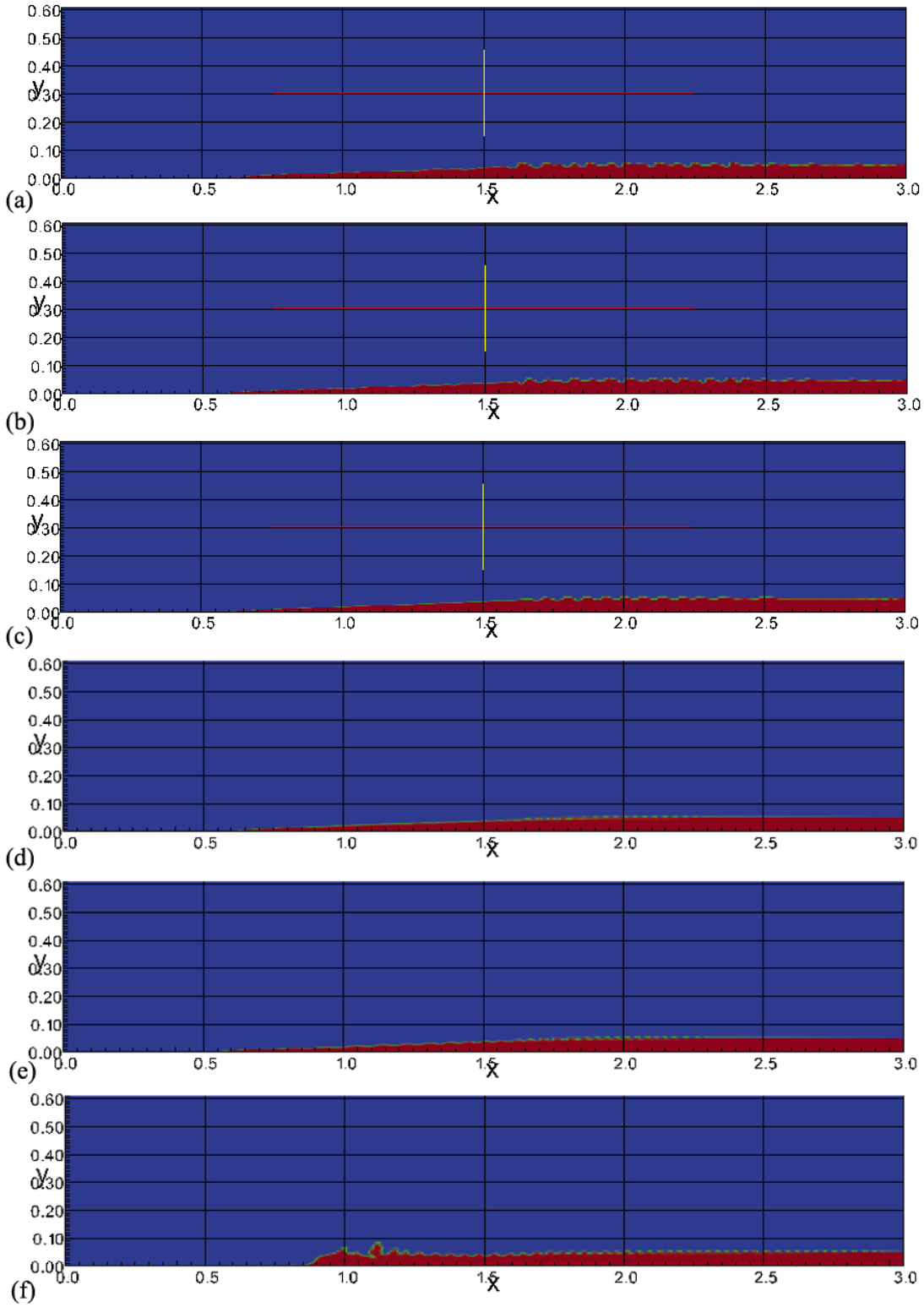

Figure 4.29. Comparison between different numerical models, simulation time 1.0 sec: (a) Fluent κ–ε; (b) Fluent κ–ε RNG; (c) Fluent κ–ω SST; (d) OpenFOAM κ–ε; (e) OpenFOAM κ–ε RNG; (f) OpenFOAM κ–ω SST.

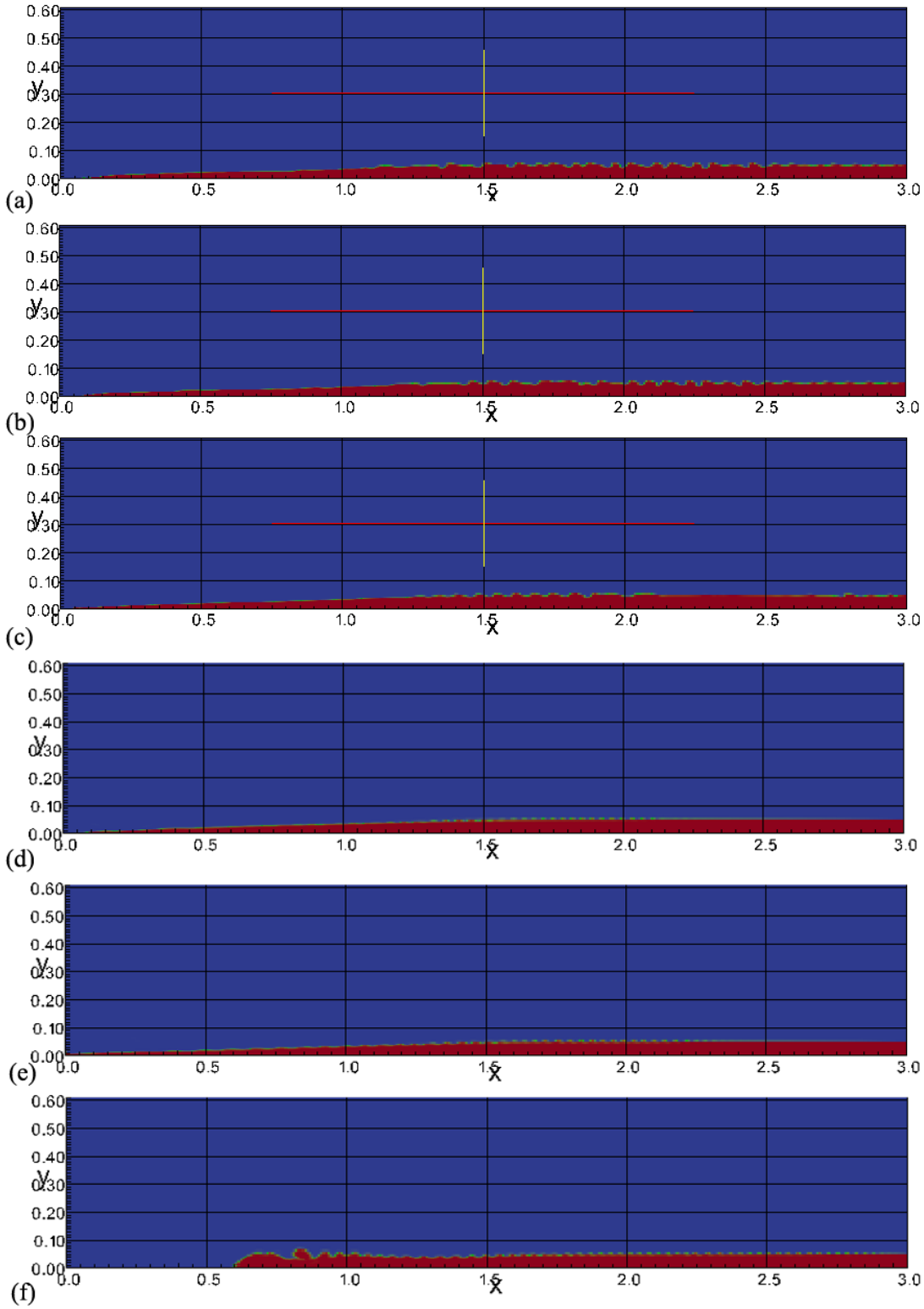

Figure 4.30. Comparison between different numerical models, simulation time 1.25 sec: (a) Fluent κ–ε; (b) Fluent κ–ε RNG; (c) Fluent κ–ω SST; (d) OpenFOAM κ–ε; (e) OpenFOAM κ–ε RNG; (f) OpenFOAM κ–ω SST.

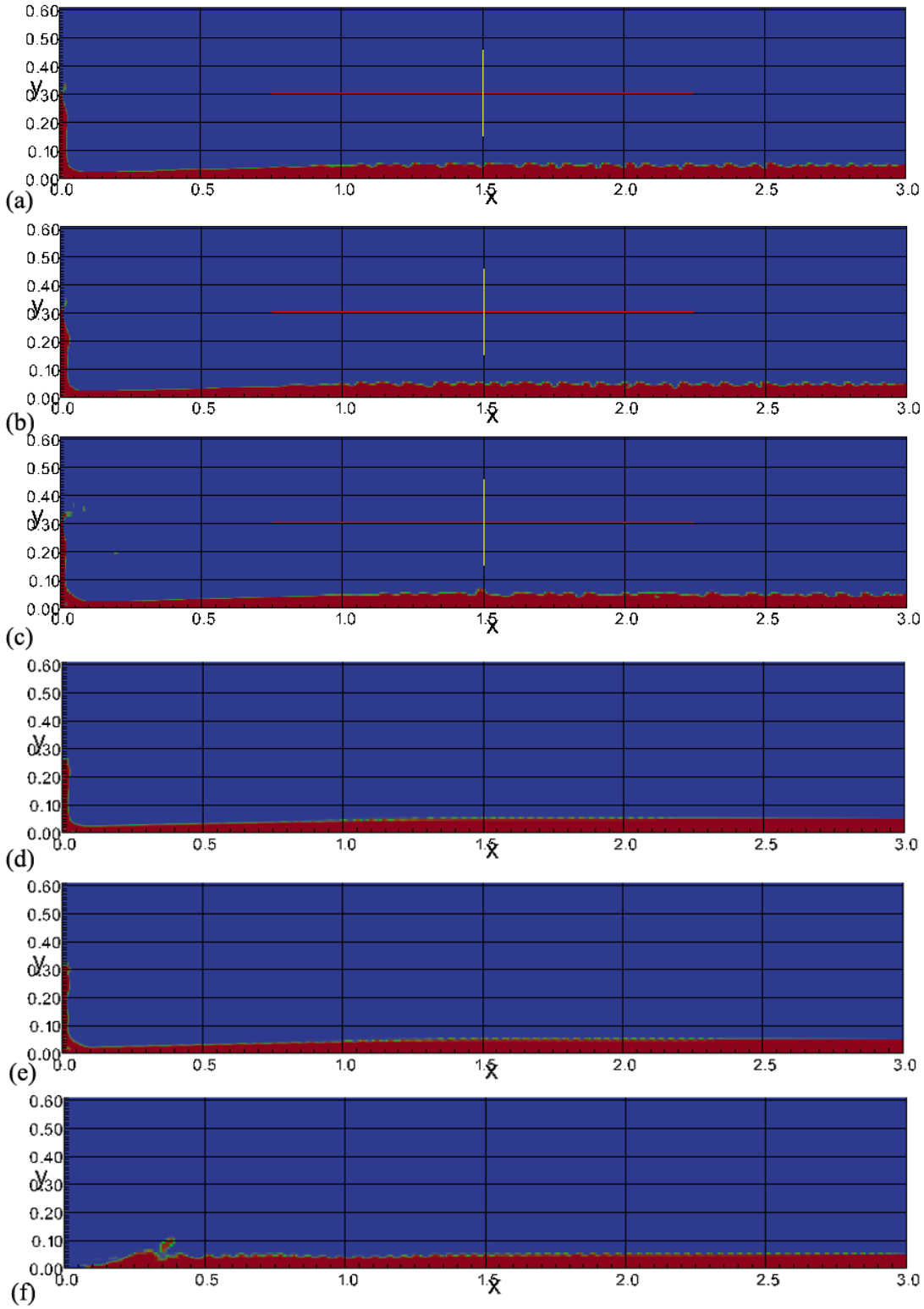

Figure 4.31. Comparison between different numerical models, simulation time 1.5 sec: (a) Fluent κ–ε; (b) Fluent κ–ε RNG; (c) Fluent κ–ω SST; (d) OpenFOAM κ–ε; (e) OpenFOAM κ–ε RNG; (f) OpenFOAM κ–ω SST.

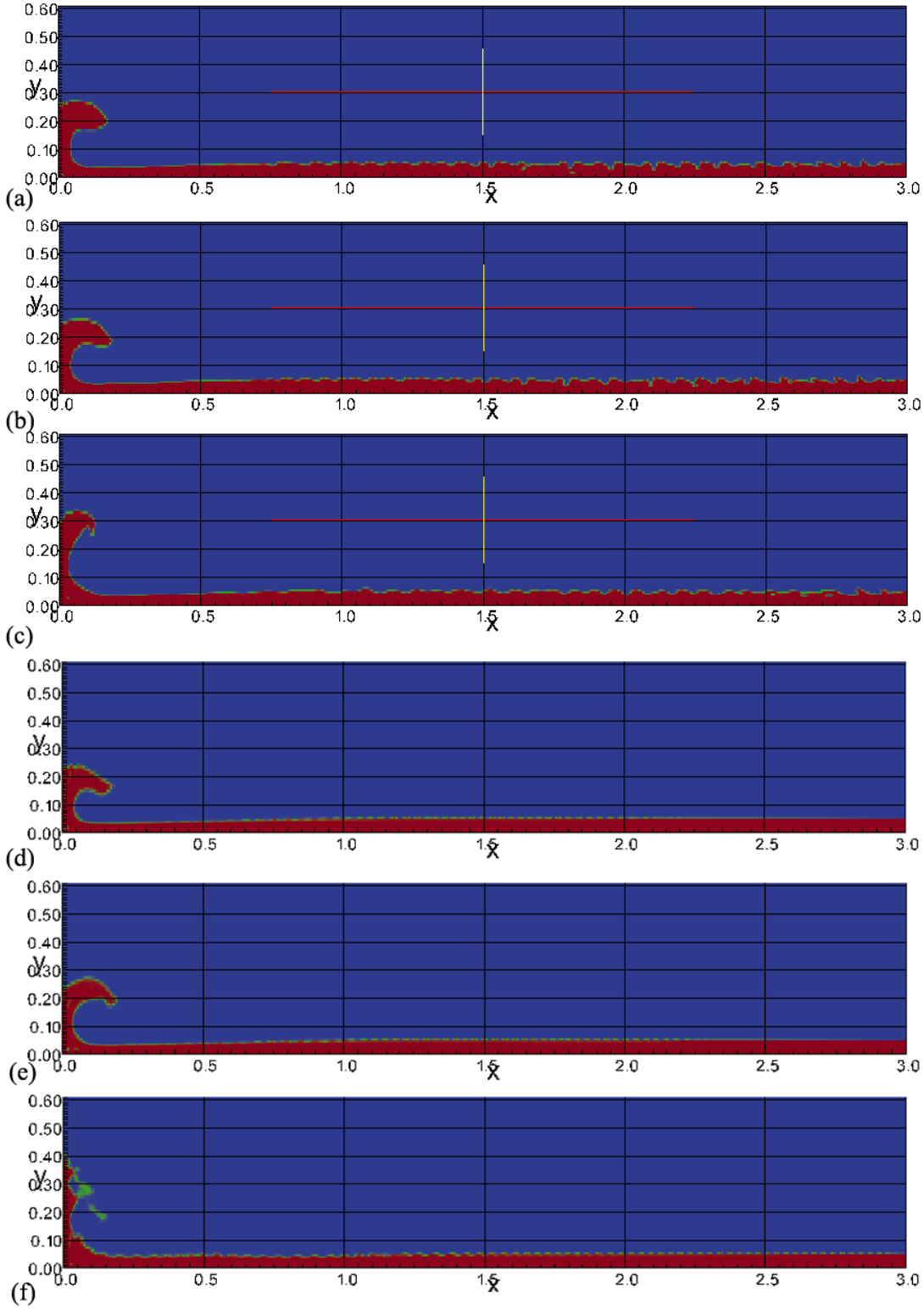

Figure 4.32. Comparison between different numerical models, simulation time 1.75 sec: (a) Fluent κ–ε; (b) Fluent κ–ε RNG; (c) Fluent κ–ω SST; (d) OpenFOAM κ–ε; (e) OpenFOAM κ–ε RNG; (f) OpenFOAM κ–ω SST.

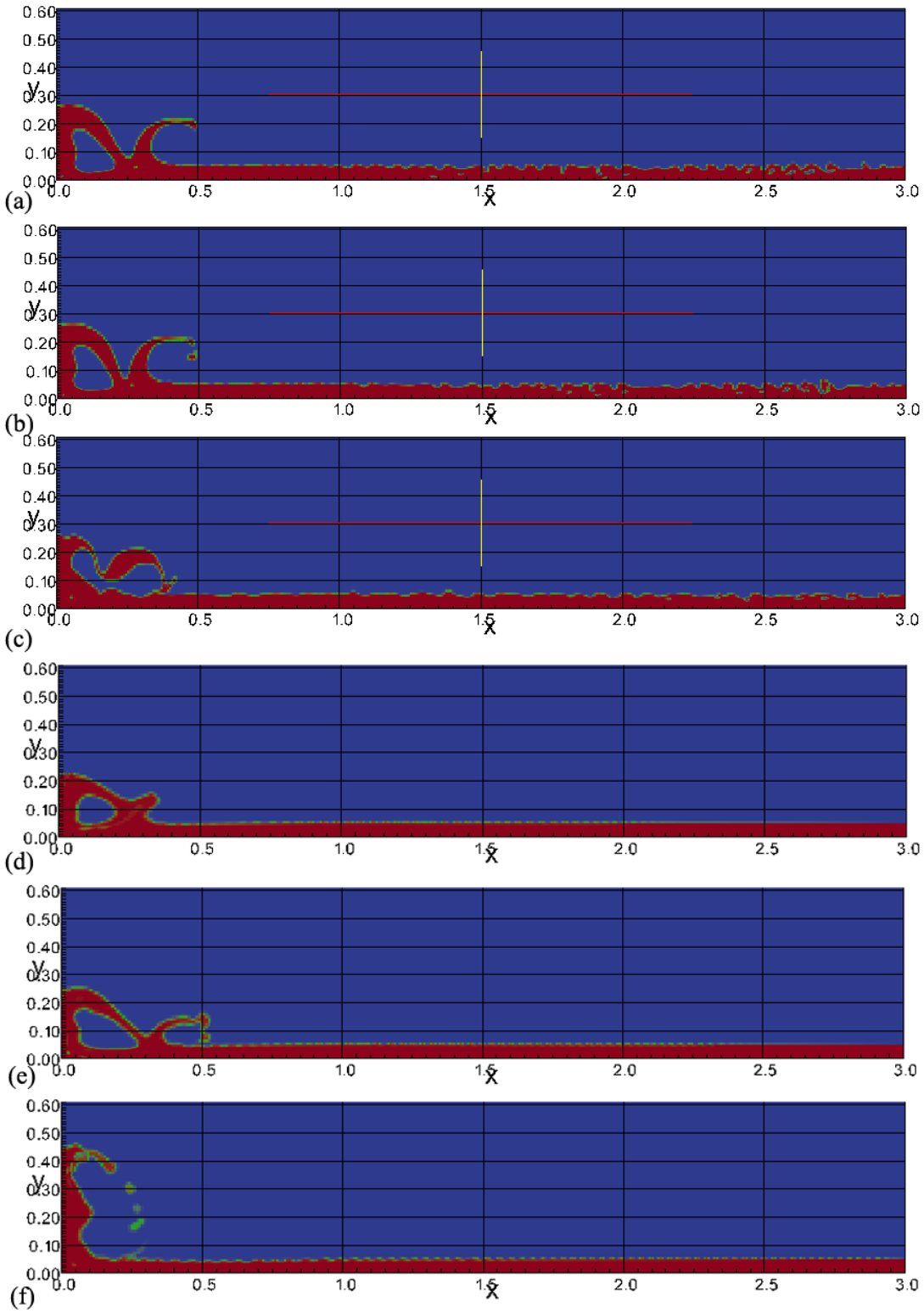

Figure 4.33. Comparison between different numerical models, simulation time 2.0 sec: (a) Fluent κ–ε; (b) Fluent κ–ε RNG; (c) Fluent κ–ω SST; (d) OpenFOAM κ–ε; (e) OpenFOAM κ–ε RNG; (f) OpenFOAM κ–ω SST.

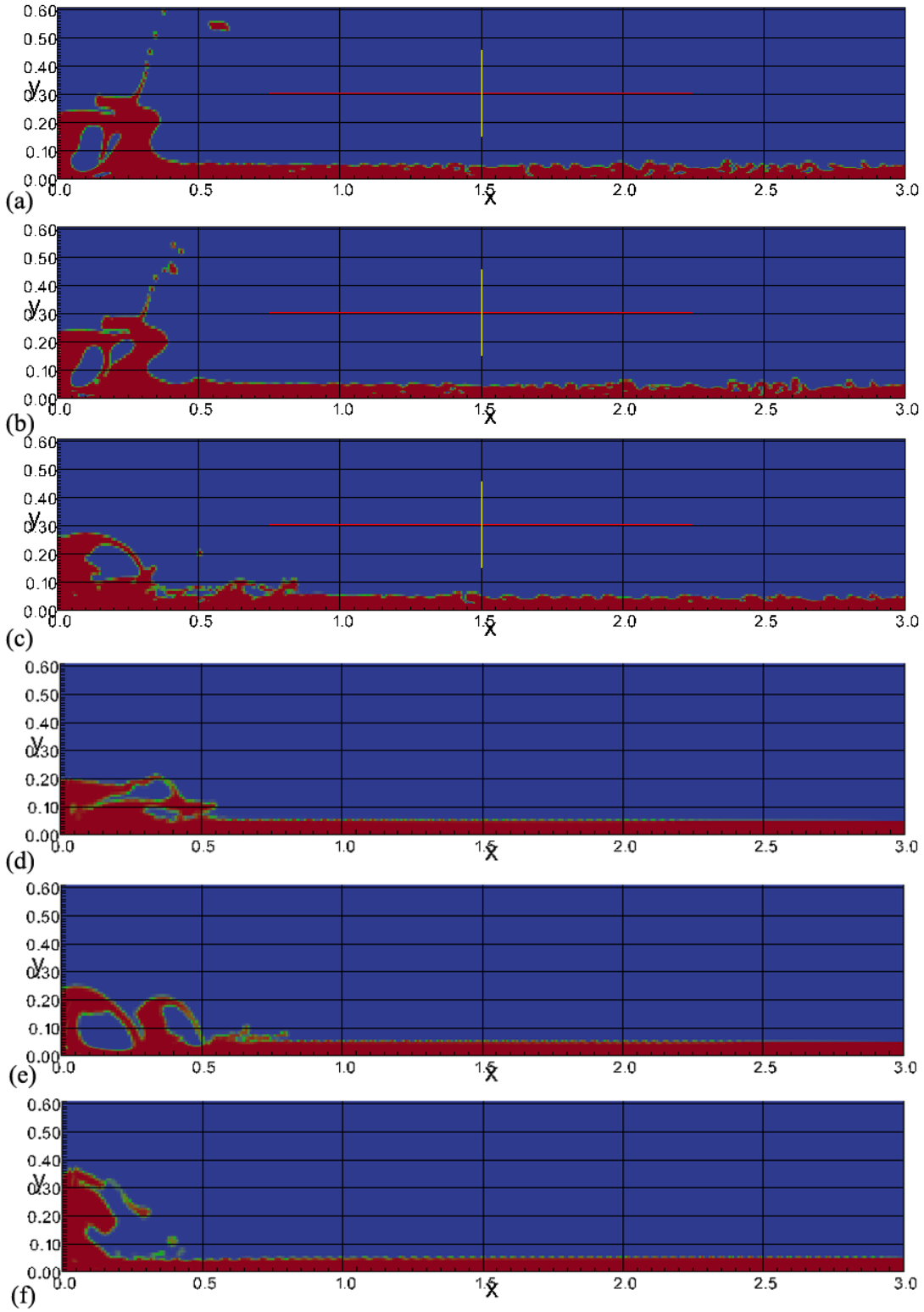

Figure 4.34. Comparison between different numerical models, simulation time 2.25 sec: (a) Fluent κ–ε; (b) Fluent κ–ε RNG; (c) Fluent κ–ω SST; (d) OpenFOAM κ–ε; (e) OpenFOAM κ–ε RNG; (f) OpenFOAM κ–ω SST.

Figure 4.35 shows results for two additional κ–ω SST solutions: using 0.00005 sec time-step and for the refined mesh in each direction with 0.0001 sec time-step. Results indicate that further refinement of the mesh and decrease in computational time step should provide more accurate result, eliminating overestimated force values and more accurate force response. Overall, the constant inflow boundary condition is in some way a better model of tsunami bore. The constant inflow boundary does not stop, but continues to generate incoming bore as is the case during tsunami, where the wave is very long and provides a constant feed of water. The numerical results were compared to the experiments with single – relatively short – solitary wave, which provides only single force peak. Following further mesh refinements, it can be seen a constant water inflow generates consecutive peaks in each of the cases despite of the used computational code. In most of the cases the consecutive peak had values larger than the first peak.

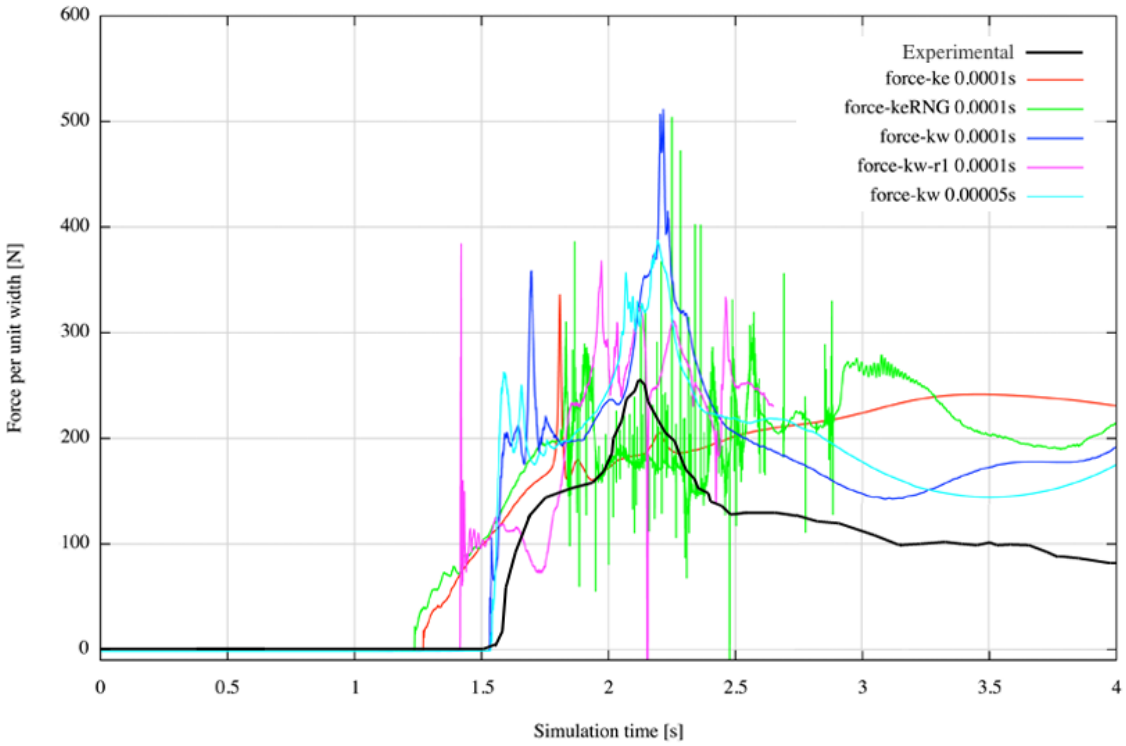

Figure 4.35. Computational TWB small reef domain.

The study described herein presents only a rough comparison between two codes. Results do not present a verification of experimental results, but only set a preliminary definitions for a chosen approach to model incoming tsunami bore. Based on discussed observations, the code of choice for further investigation was OpenFOAM.

4.4.3.2 Large Wave Flume (LWF)

Experiments in the Large Wave Flume (LWF) were also simulated. The domain, similarly to the TWB domain, represented only the flat reef end section of the setup described in Chapter 3. The two-dimensional domain had an instrumented wall height of 4 m and the 18 m flow length. The modeled case was also for the dry-bed condition with the 12.7 cm high bore resulting from 0.354 m solitary wave with 4.35 m/s inflow velocity (water reaching the wall in approximately 4.14 sec). The domain consisted 37,664 cells, Figure 4.36. Only the κ–ω SST turbulence model was used. Force results are presented in Figure 4.37. The experimental force recording frequency was 1000 Hz.

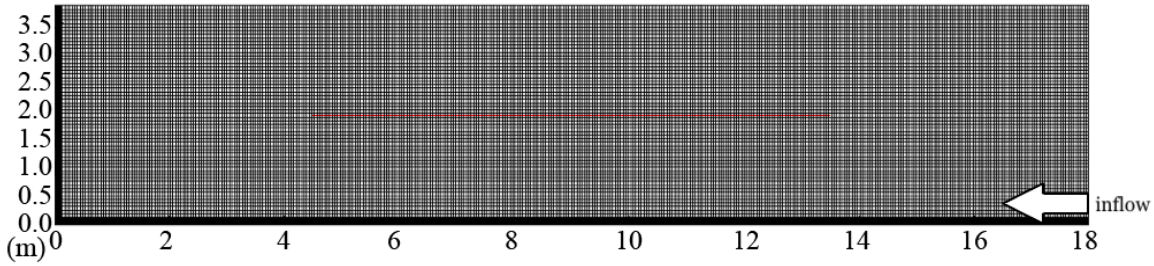

Figure 4.36. Computational LWF small reef domain.

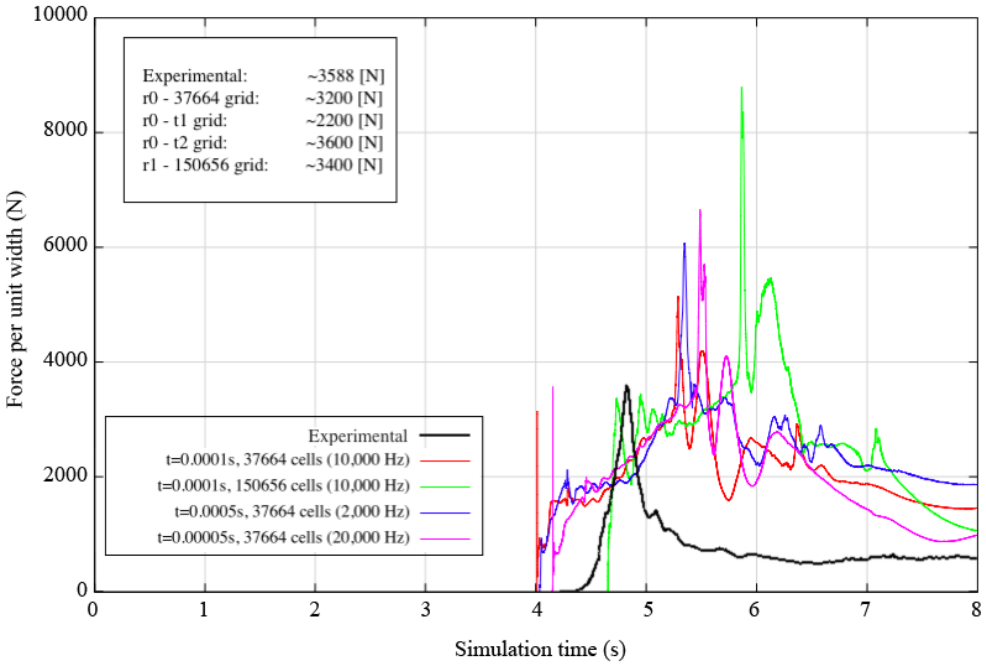

Figure 4.37. Computational LWF result vs. experimental.

In the case of LWF simulation the results gave better correlation to experimental force data, especially with the simulation time-step decreased and mesh refined. Refinement included cell division in both horizontal and vertical directions. For the refined mesh the results provided approximately very similar initial impact force value with a difference of about 5% (200 N). Also no initial overshoot peak was visible, contrary to the lower quality meshes with the same size of the time-step, 0.0001 sec.

Overall, it is hard to validate the result. The numerical model has closer representation to predicted experimental tsunami flow duration. However, the experimental data resemble only the load from a single solitary wave, which wavelength is not too significant. Short wavelength means relatively short lasting load buildup compared to a real tsunami wavelength.

This LWF model is better from TWB domain in the sense that the distance devoted to the bore development is much larger than the one in TWB. The flow distance was three times larger than the one in TWB with a bore height approximately 2.5 times larger.

The most refined mesh, which was run, had approximately 600,000 cells. Those results also depict, as the result of sustained water inflow, the forces are much larger after the initial bore impingement. The closest case in terms of initial impact force compared to the recorded experimental data was the case with refined mesh of 150,656 cells and 0.0001 sec time-step (10,000 Hz). The volume of fluid field for this particular run is presented in Figure 4.38. All of the cases with refined meshes depict a large force build-up after the initial impact. Results indicate there is not enough data and there is further need for more accurate experimental studies to verify the computational models. Numerical results also confirm high-pressure fluctuations over a very small time scale, much larger than 1000 Hz [39].

The number of computationally tested cases does not provide a definite answer in terms of numerical model definition. A more advanced study should be performed.

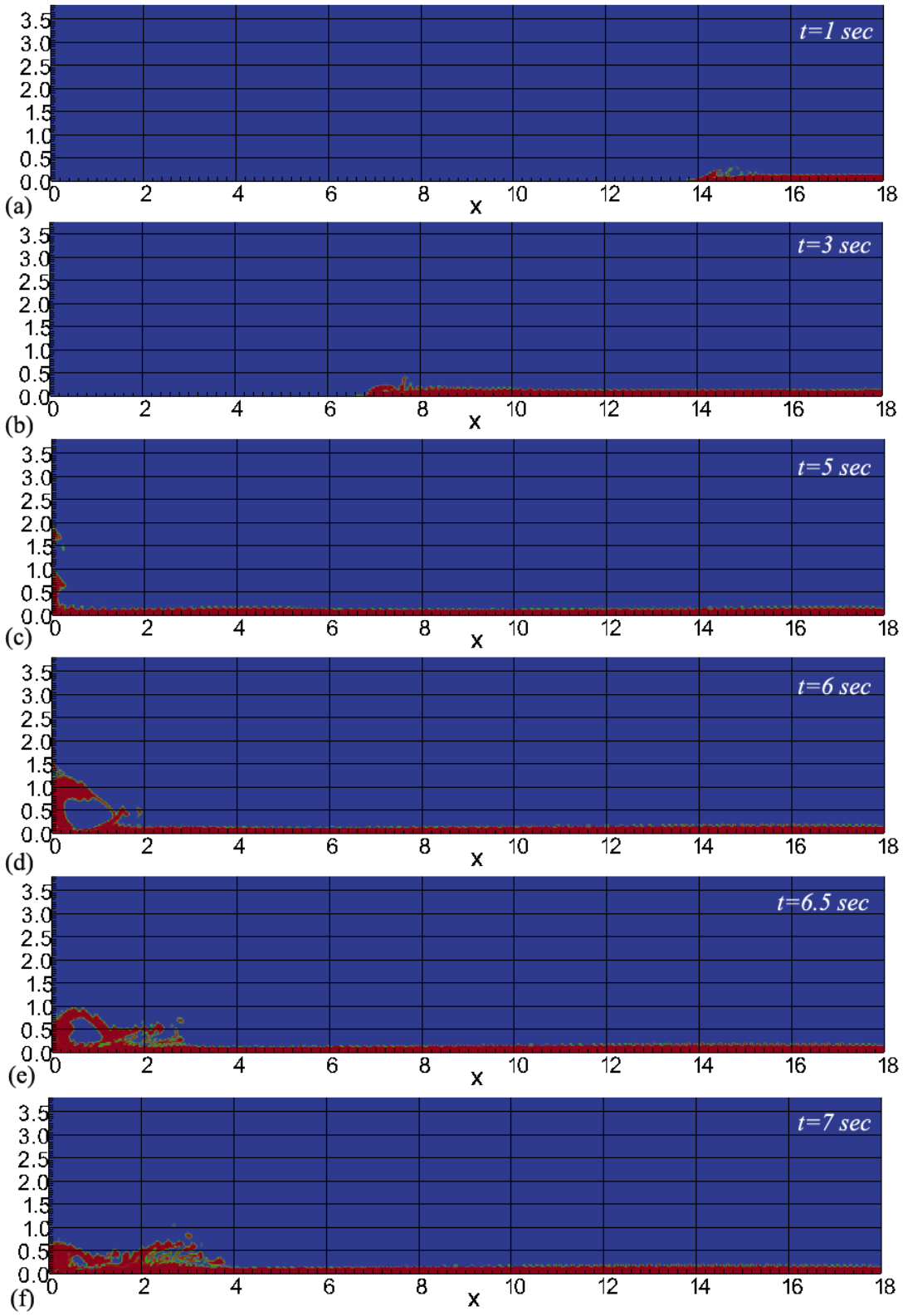

Figure 4.38. Volume of fluid, 150,656 cells, 0.0001 sec time-step (10,000 Hz) with 12.7 cm bore height with 4.35 m/s approach velocity.

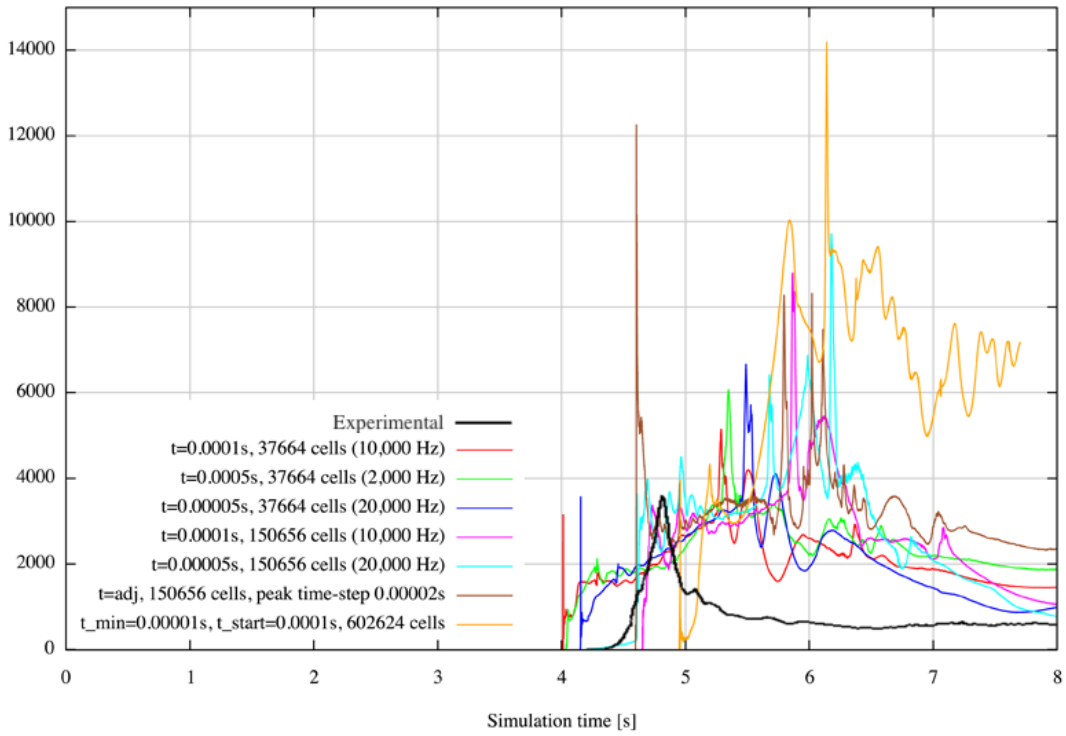

Figure 4.39. Computational LWF flat reef domain results.

4.4.3.4 Non-slip vs. slip wall boundary

With inflow boundary domain a test was run to compare non-slip vs. slip wall boundary effects. For the really fast approaching bore, an argument can be made that the wall functions should not play an important role in the bore advance and development. The test indicated that this is not true and that frictional effects matter, where lack of a wall function generates faster advancing bores, therefore, generating higher wall forces. The shape of the bore in both of the cases was almost the same, with non-slip case resembling a bit steeper bore front and slower advancement, Figure 4.40.

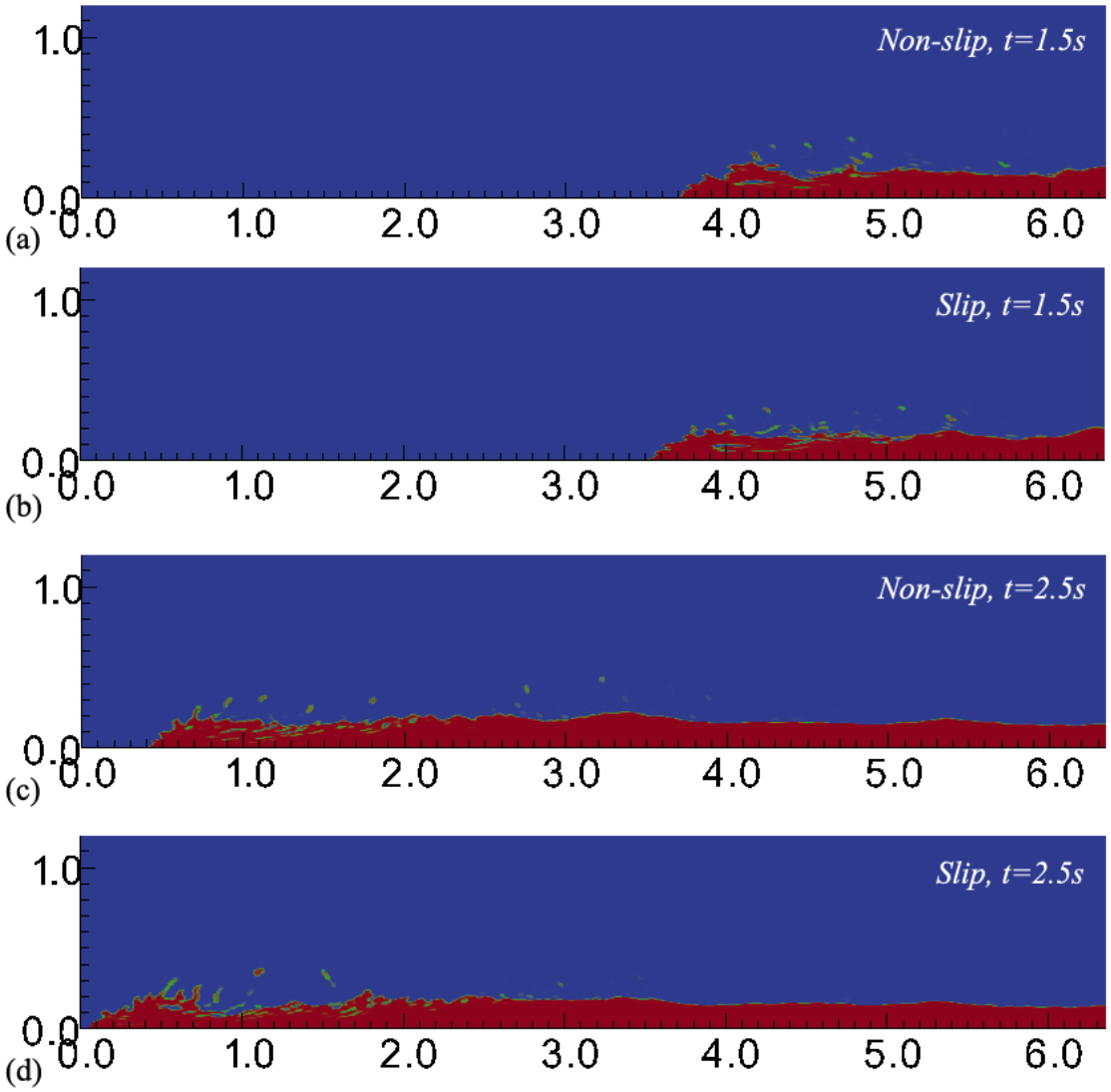

Figure 4.40. Non-slip vs. slip tank bottom wall boundary.

4.4.5 Variable inflow boundary

The variable inflow boundary domain is very similar to the setup described in the above section. The main difference is in the definition of the inflow boundary, which is still constant along the height, but can vary with time. To limit discrepancies between experimental setup and numerical model, the experimental ADV recording was used for the inflow velocity time-history, Figure 4.41. It should be noted that the bore front advancement velocity extracted from video did not equal the ADV measurements. Usually, the video extracted velocities were slightly higher. This characteristic confirms highly turbulent nature of the bore.

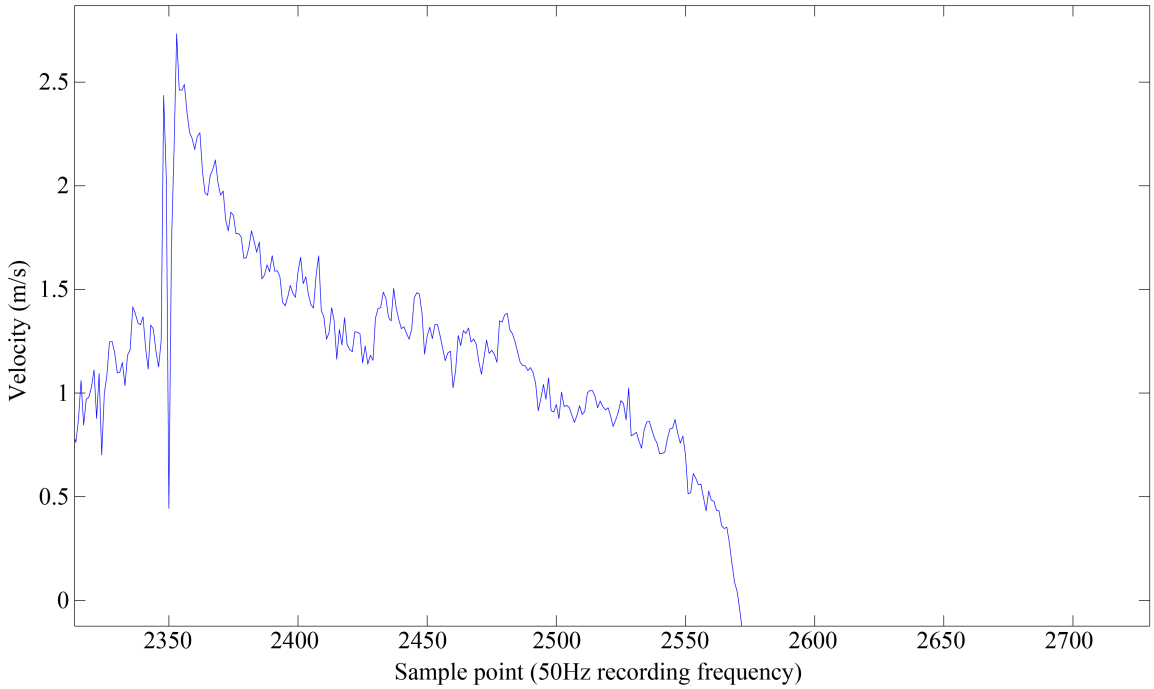

Figure 4.41. Sample LWF ADV recording at the location of bore inflow.

A few different configurations were tested. The first configuration was defined based on the observation of bore formation and flow development in the wave break TWB model. The previous simulations indicated that the still water level does not pick up the incoming bore velocity immediately, but instead with some delay. Therefore, in the model, the section of the inflow boundary corresponding to the bore jump had a velocity equal to the ADV measurement. The 'standing water' section of the inflow boundary had a similar time-history, but with a delay of 1 sec. This way, the constant height inflow was maintained, but with delayed still water level movement, Figure 4.42, case 1. The second model had both sections defined by the same ADV history starting equally at the very beginning of the simulation, Figure 4.42, case 2. The third case had still water portion not having any assigned inflow value; it remained still. The top part of the inflow had a constant inflow velocity of 3.8 m/s, which equaled to the bore velocity extracted from movie recording for one of the trials for 106 cm solitary wave, Figure 4.42, case 3. The fourth model had a constant velocity of 3.8 m/s along the whole bore height, Figure 4.42, case 4. The last model was similar to the third one with the difference in bore jump velocity, which equaled to the maximum peak value observed in the initial ADV

recording and was 2.7 m/s, Figure 4.42, case 5. The recorded force time histories are presented in Figure 4.43. Immediately, it can be seen models 3 and 4 do not provide good results. The force values were significantly overestimated. This indicates that the use of the bore leading edge velocity along the whole bore height is not correct and yields unrealistic results. The result for the third domain had an initial peak force with a similar value to the experimental result, but then built up to a value about three times higher. This result resembles characteristics similar to Figure 4.39, section 4.4.3.3., constant inflow boundary. It indicates that the constant velocity flow sustained for a long period of time might yield much higher forces than the one for single solitary wave tested experimentally. A zoomed portion of the results is presented in Figure 4.44. Two of the best results are for models 1 and 5. Case 5 response is similar to case 3, with the difference in velocity magnitude. Both models reach the same level of the experimentally measured wall force. However, the force rise does not overlap with the one observed in experiments. Also the velocity time history and magnitude differ quite significantly. Shifting the time scale discrepancy and plotting both domain forces on top of each other we can see quite a good correlation to experimental values, Figure 4.45. The differences in the domain 1 can occur because of the reduced dimension of the problem to two-dimensional scale. In reality, the flow is highly three-dimensional. In the model we removed one dimension and additionally we only use the flow velocity measurement just for one ADV point, whereas in reality the velocities are highly variable among the whole domain. Reducing the flow velocity to a single measured value or time-history is a large simplification, which still yields good results. Summarizing, the best predictions were from cases 1 and 5. Whenever it is possible to use the velocity recording during the impact case 1 should predict sufficient force time-history. In real conditions, it is not the case and there is no time-history data available. Instead, the average bore velocity could be estimated. One of the possible solutions is the use of [89], however, the application requires further research.

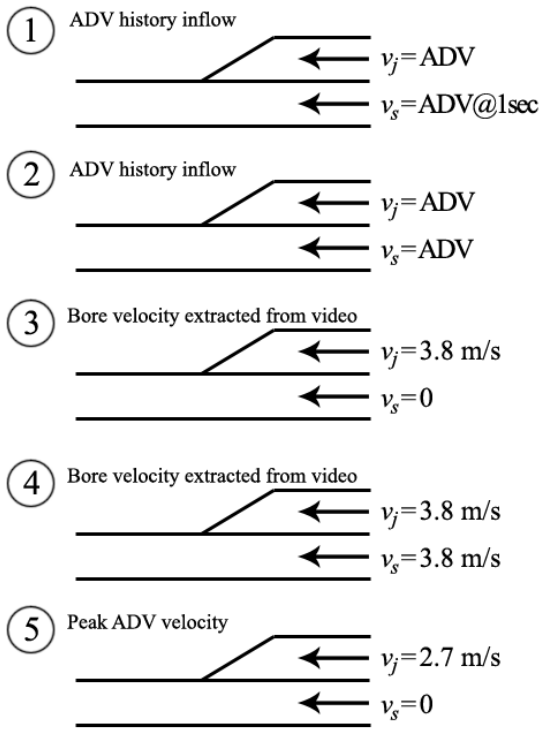

Figure 4.42. Different tested inflow boundary conditions.

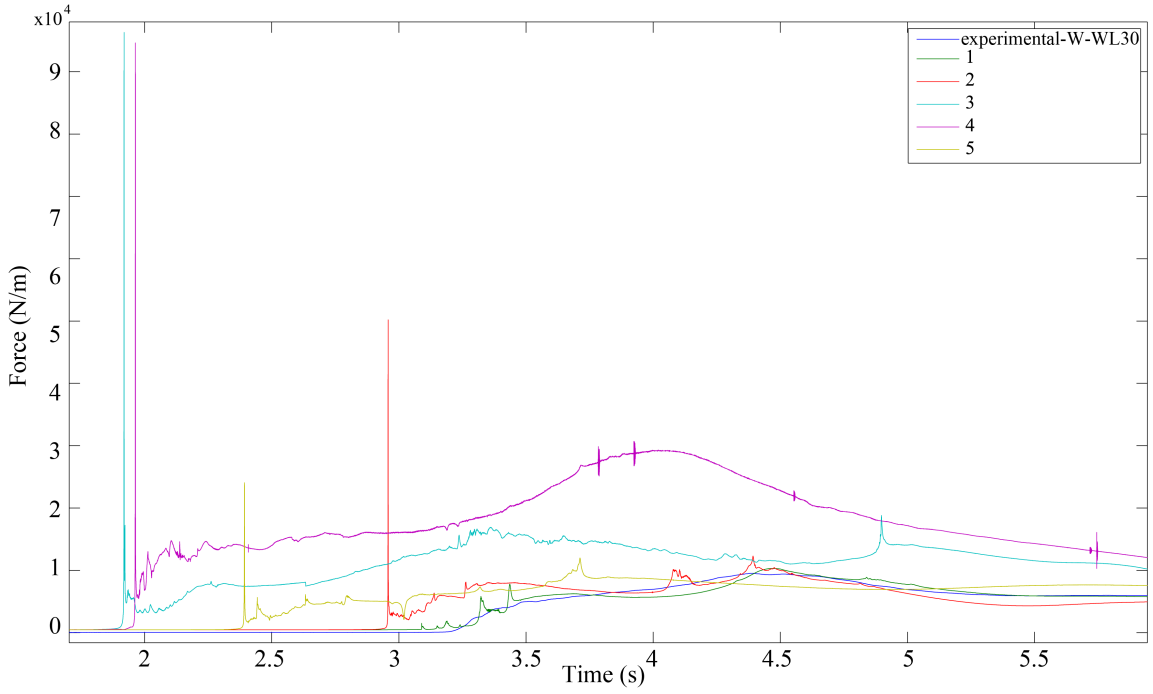

Figure 4.43. Variable boundary inflow: comparison of results.

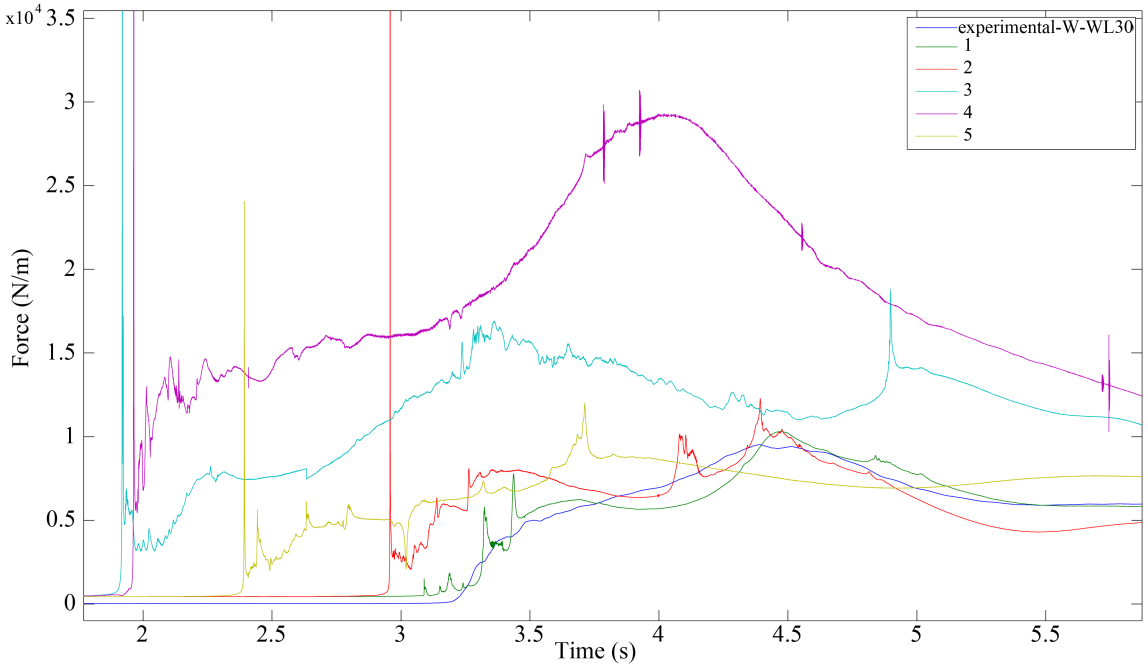

Figure 4.44. Variable inflow boundary: comparison of results; enlarged vertical scale from Figure 4.43.

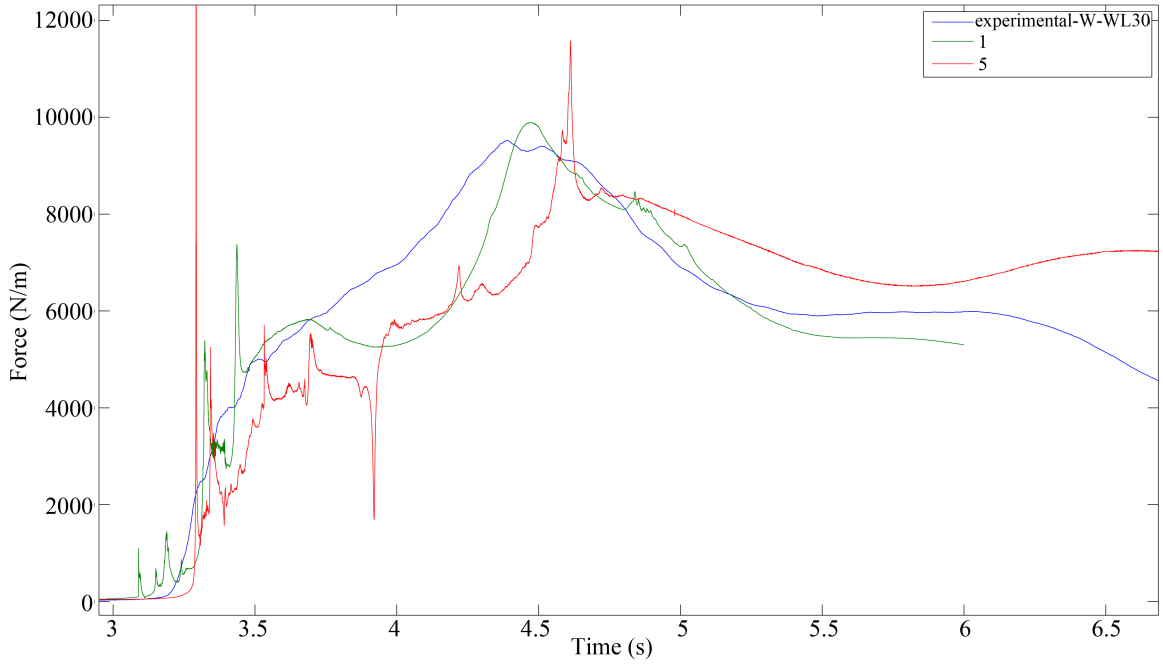

Figure 4.45. Variable inflow boundary: comparison of results, domain 1 and 5; enlarged vertical scale and shifted time scales from Figure 4.43.

4.4.6 Dam break

The dam break scenario is possibly the most robust approach. It is defined by a reservoir of water initially retained by a gate. When the gate is removed, the water collapses transferring into a fast flowing bore, which is essentially the same as experimentally created tsunami bore [71]. In experimental conditions, it does not involve direct wave breaking. The second, knowing the dam height, the water column collapse provides correct bore height and expected bore velocity. In computational terms, the disadvantage of this model is the domain size. It results in increased computational effort as compared to the domain with inflow boundary condition. To reproduce a long lasting tsunami bore a large water reservoir is required. Additionally, the larger the desired bore height the higher the water run up upon the wall structure, which for bores resulted from higher waves will exceed the wall height. In such cases the domain must be extended vertically, to accommodate water jet shooting up.

The simulations were run for the most severe case, i.e., the case with the biggest bore. The largest of the recorded LWF waves was 106 cm traveling on top of the 30 cm still water level. The higher still water level resulted in the least amount of friction and therefore the highest bore velocity.

4.4.6.1 Water reservoir definition

Stoker theory [86] provides equations for dam reservoir height, which are equivalent to hydraulic jump theory. The equations are derived from the relation of the initial dam height to the downstream water level.

From the conservation of mass and momentum the bore velocity can be defined [71]

$$v_j = \sqrt{g\frac{(h_j+d_s)}{d_s}\left(\frac{(h_j+d_s)+d_s}{2}\right)} \tag{4.25}$$

in which h_j is the known bore height and d_s is the still water level at front of the dam. The collapsing dam velocity is

$$v_d = v_j - \frac{gh_j d_s +}{4v_j}\left(1 + \sqrt{1 + 8\left(\frac{u_b}{\sqrt{gd_s}}\right)^2}\right) \tag{4.26}$$

with the wave propagation speed

$$c_d = \sqrt{gd_s}\sqrt{\frac{1}{2}\left(\sqrt{1 + 8\left(\frac{v_j}{\sqrt{gd_s}}\right)^2} - 1\right)} \tag{4.27}$$

From Stoker's characteristic relationships [86], in the water dam fall region, the dam height can be calculated by

$$h_d = \frac{1}{4g}(v_d + 2c_d)^2 \tag{4.28}$$

Knowing the desired bore speed and height, the dam height h_d can be calculated. The length of the dam can be arbitrary depending on the need of the simulation and defines the time length of water flow maintaining the same bore height until the reservoir empties.

4.4.6.2 Dam break computational results

For the tested condition, 106 cm wave with 30 cm standing water, the experimental bore velocity was 3.27 m/s and the experimental jump height was 40.6 cm. For the given values, the required dam height from equation (4.28) was 122 cm, which was used as a computational dam height.

Two domains were tested, as shown in Figure 4.46 and Figure 4.47. The small domain was 15 m long with 5 m long reservoir and 10 m downstream length for the bore development. The second domain, named large, was 40 m long with 20 m long reservoir and equal length left for the bore formation. Both domains were 3.2 m high in bore development zone with 4 x 4 m square at the end of the bore flow, where the instrumented wall was placed. Each of the domains had two different meshes. For the small domain the basic and refined grid had 116,191 (Figure 4.46) and 464,764 cells, respectively. The higher resolution mesh was a refinement of the basic mesh, splitting each of the quadrilateral elements in four. For the large domain the basic grid had

295,484 cells (Figure 4.47) with refinement having 1,181,936 cells. The resolution of the large grid within the length of the small domain from the wall, 15 m, was designed in such a way that the mesh resolutions between large and small were comparable.

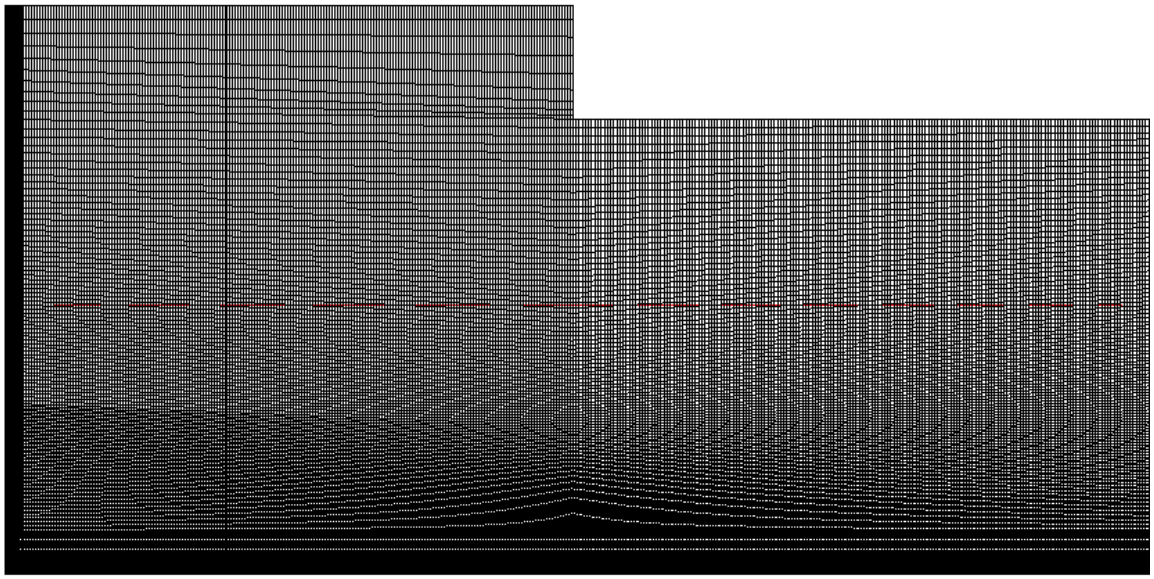

Figure 4.46. Small (15 m) grid impact zone, 116,191 cells. 9 m portion from the wall.

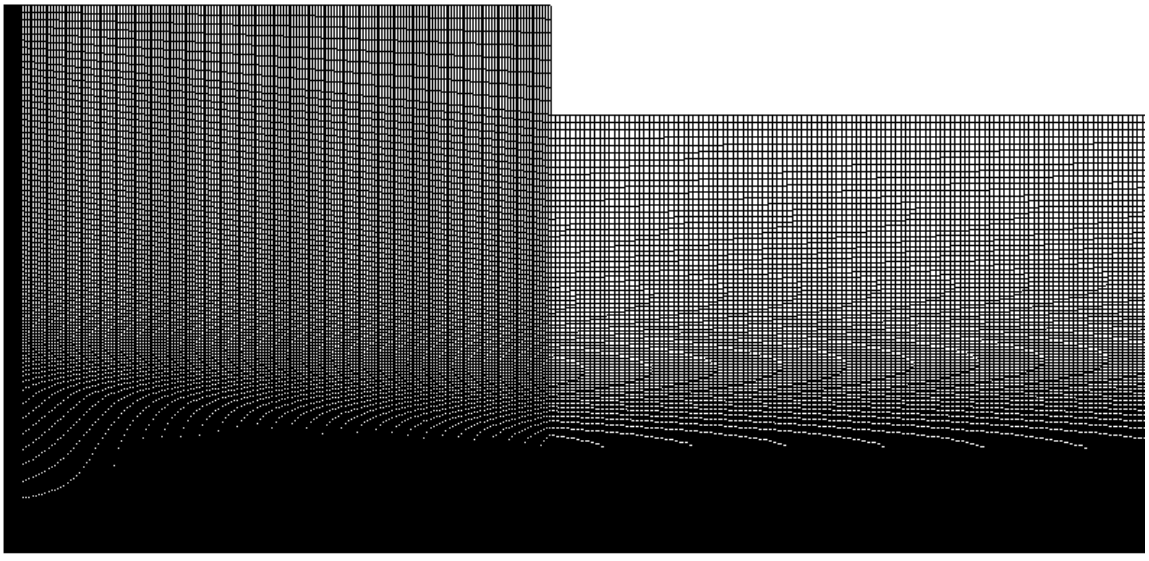

Figure 4.47. Large (40 m) grid impact zone, 295,484 cells. 9 m portion from the wall.

The volume of fluid time frames are presented in Figure 4.48–4.51. In the figures, the first frame in each of the plots depicts the initial setup of the domain. On the right side

the water reservoir is defined. The left side of the tank defined the instrumented wall. Sequential frames in each of the figures depict water column collapse, bore formation, its advancement, and finally wall impingement. The last frame depicts water return right after the wall impact. In this frame, the bore inflow is still maintained just the water accumulating at the wall recedes back on top of the incoming flow.

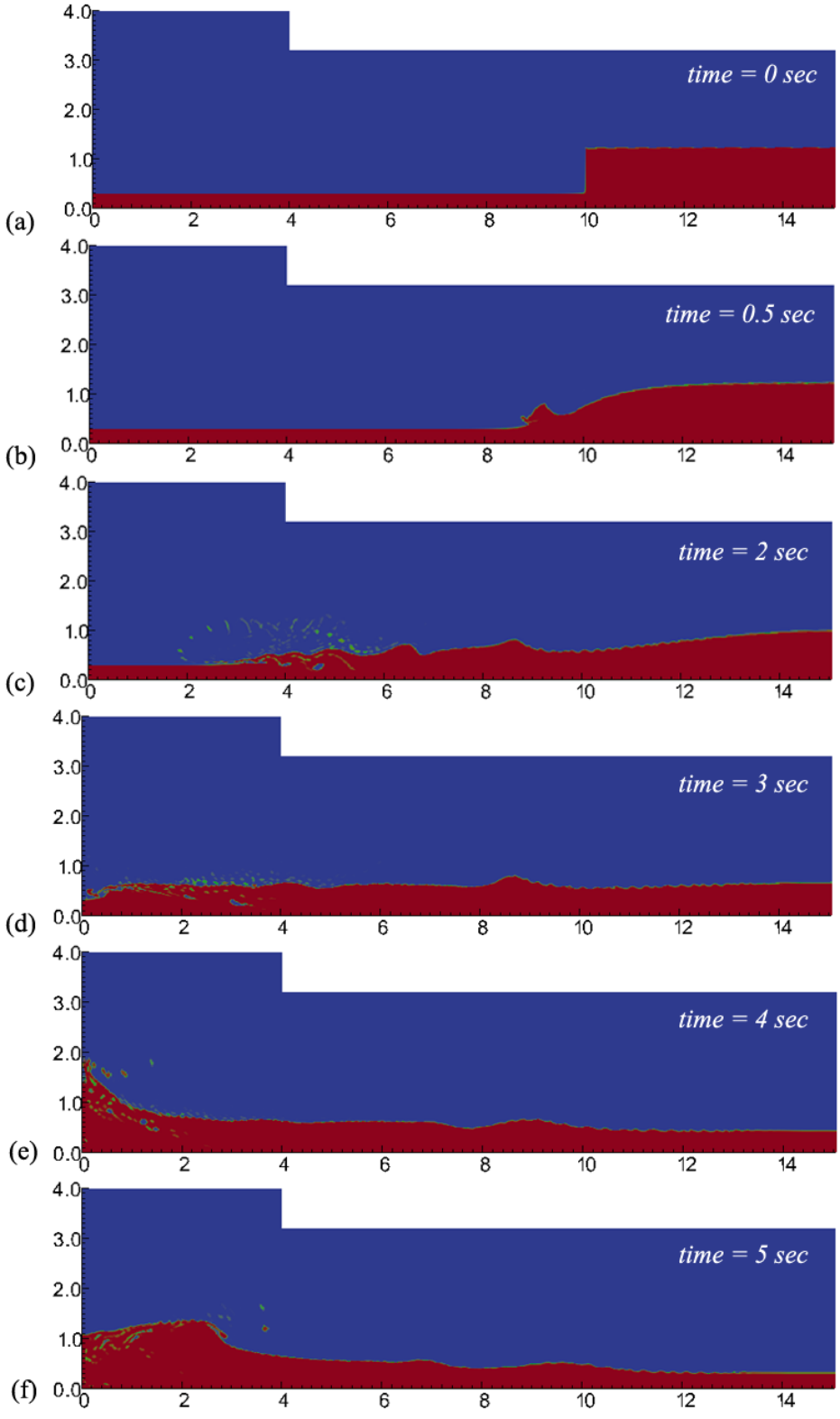

Figure 4.48. Small (15 m) grid: 116,191 cells, volume of fluid time frames.

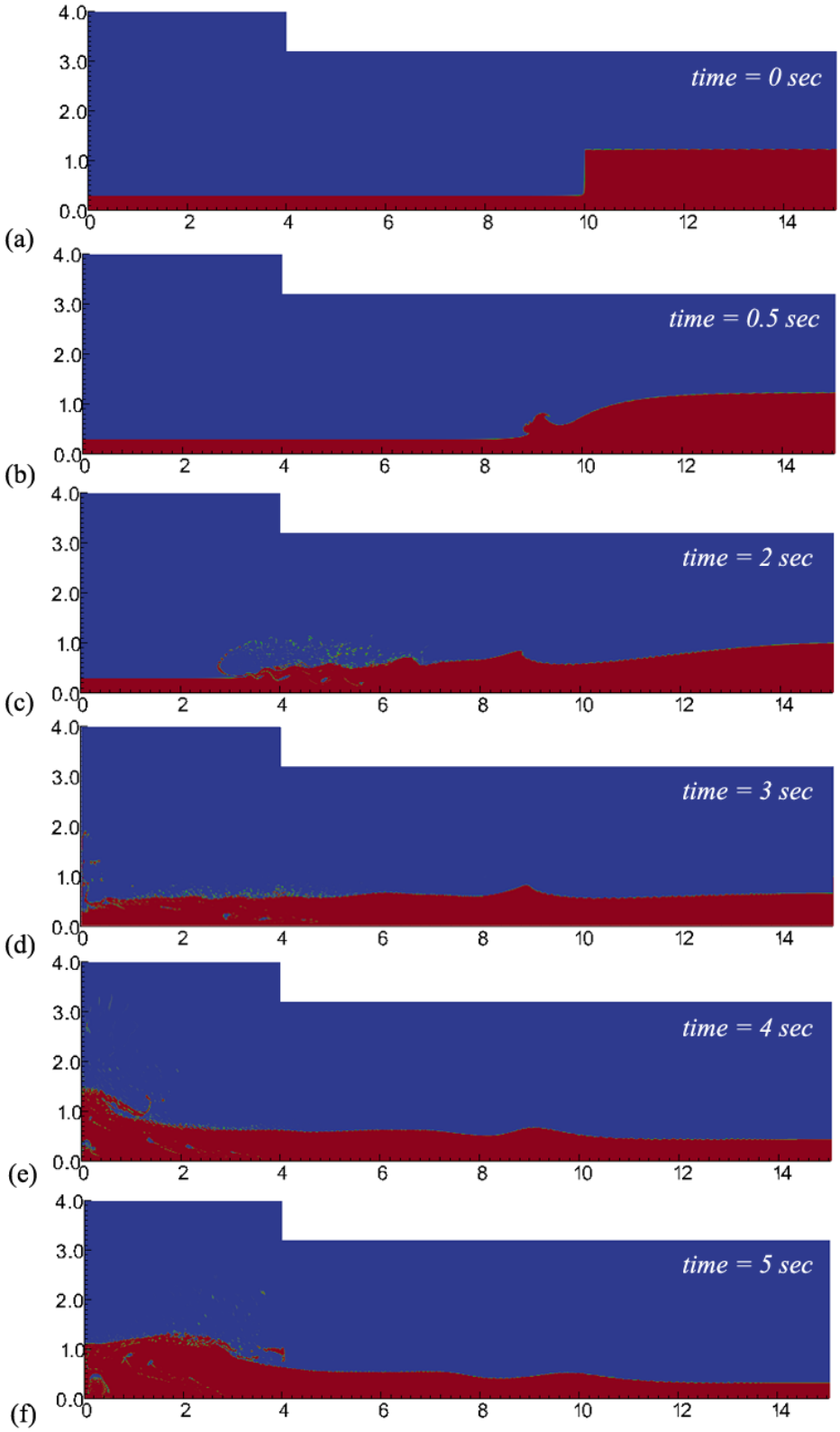

Figure 4.49. Small (15 m) grid: 464,764 cells, volume of fluid time frames.

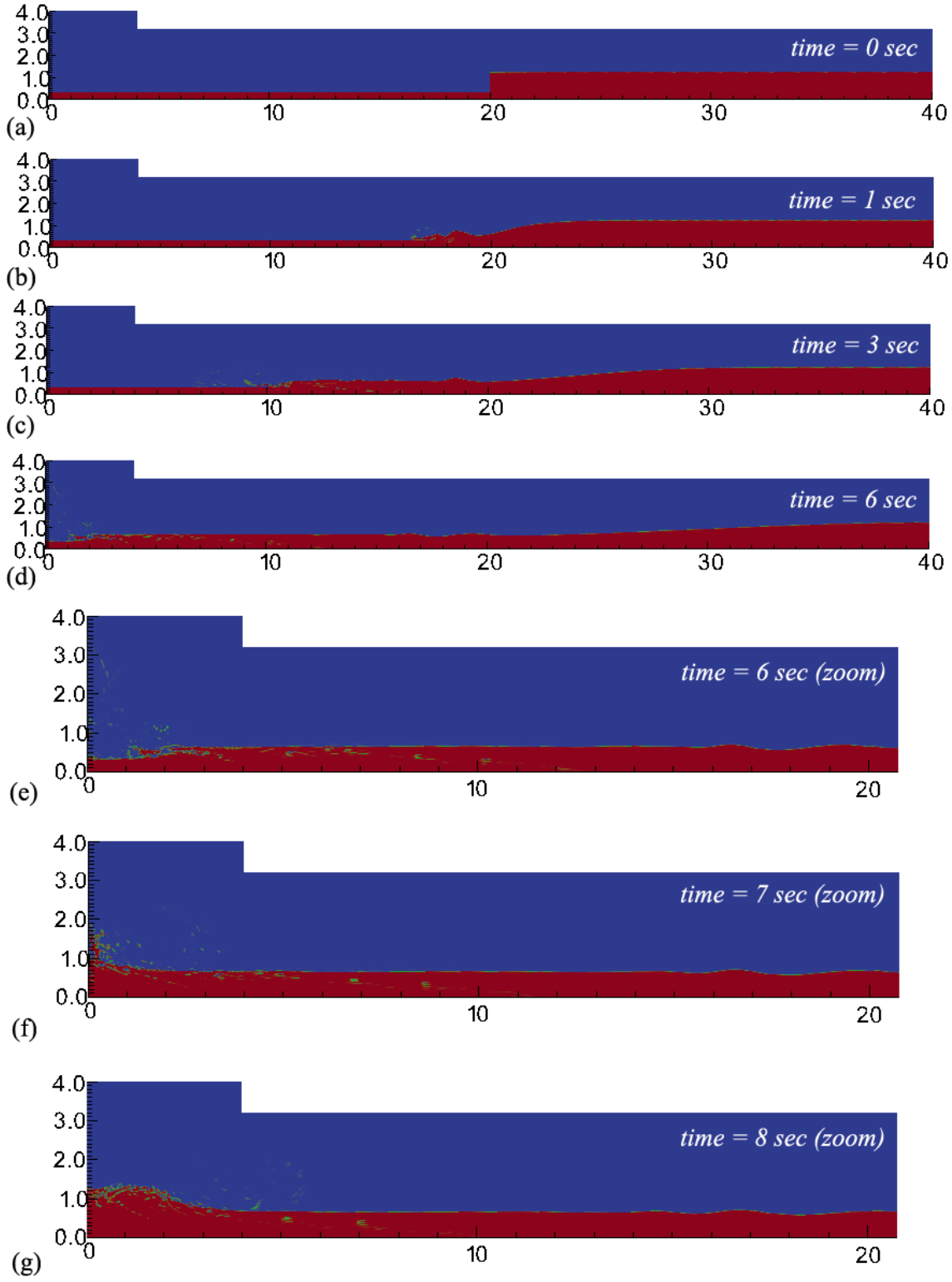

Figure 4.50. Large (40 m) grid: 295,484 cells, volume of fluid time frames.

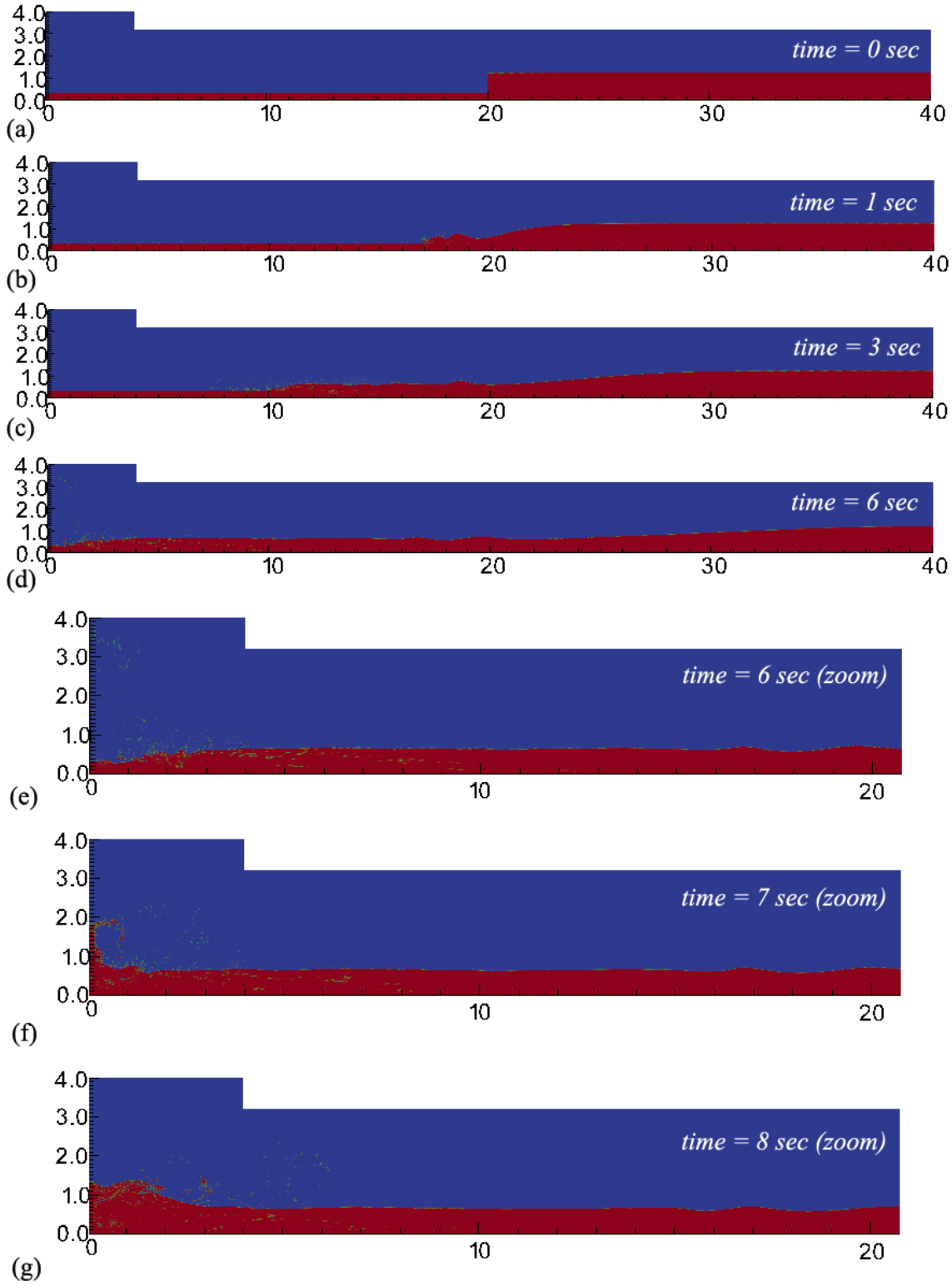

Figure 4.51. Large (40 m) grid: 1,181,936 cells, volume of fluid time frames.

For each of the figures, the loads experienced at the wall are shown in Figure 4.52–4.55. Figure 4.52 presents all of the results from described meshes. Figure 4.53 depicts results comparison for two different meshes for the large domain. Figure 4.54 depicts results comparison for two different domains with coarse grids. Ultimately, Figure 4.55 compares the meshes with the highest cell resolution for both of the domains. Some of the simulations, before the impact, indicate some noise in the load time history. It can be assumed these are leading edge water particles advancing at the front of the bore flow. Compared to experiments the computational model is very sensitive, hence existence of those pre-impact forces. One of the coarse meshes did not exhibit these loads.

None of the simulations was able to predict exactly the same magnitude of the force experienced at the wall, as it was recorded during the experiments. Chapter 3 indicates, there was variability in experimental results among the same flow conditions, i.e. the same bore height resulting in different wall forces. Important is the fact that the time history shapes in large part coincided with experiments. In the problem, highly turbulent flows are experienced, therefore, small time history shape differences must be allowed. From the nature of turbulent flows, for different meshes, it is impossible to have the same repeated conditions in each of the simulations, as experimental results indicate it as well. It is assumed the model is valid and provides a way to estimate force time histories experienced by structures during tsunami bore impingement; however, the underestimated force results indicate, a more thorough study must be conducted with further attention to computational grids in regard to bore formation, so the wall forces could be estimated with more precision. It is possible, the three-dimensional effects could play an important role in the simulations; to confirm this hypothesis further study is required.

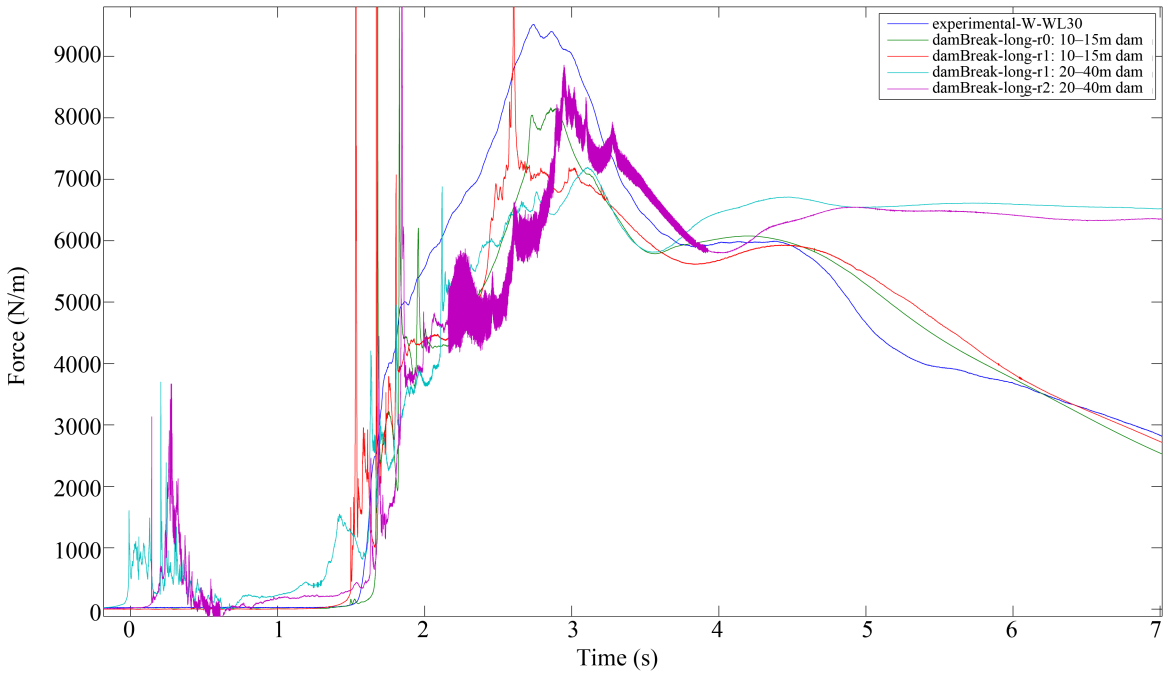

Figure 4.52. Comparison of results: large and small domains with different grids and experimental data.

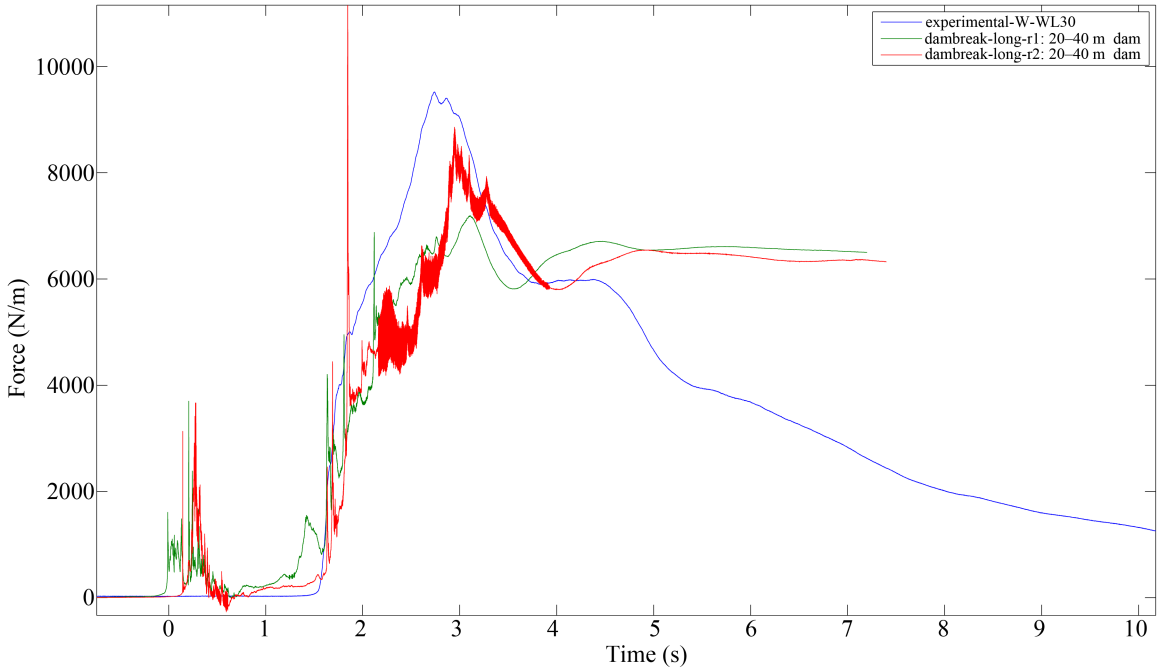

Figure 4.53. Comparison of results: large domain, two different grids and experimental data.

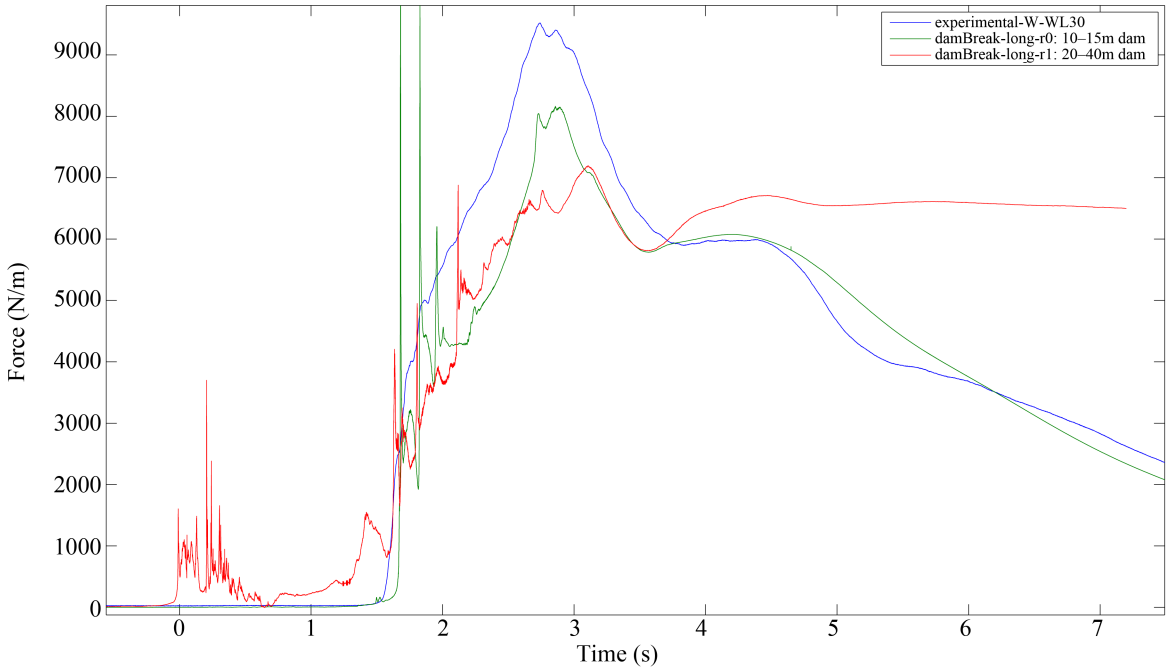

Figure 4.54. Comparison of results: small and large domain low quality grids and experimental data

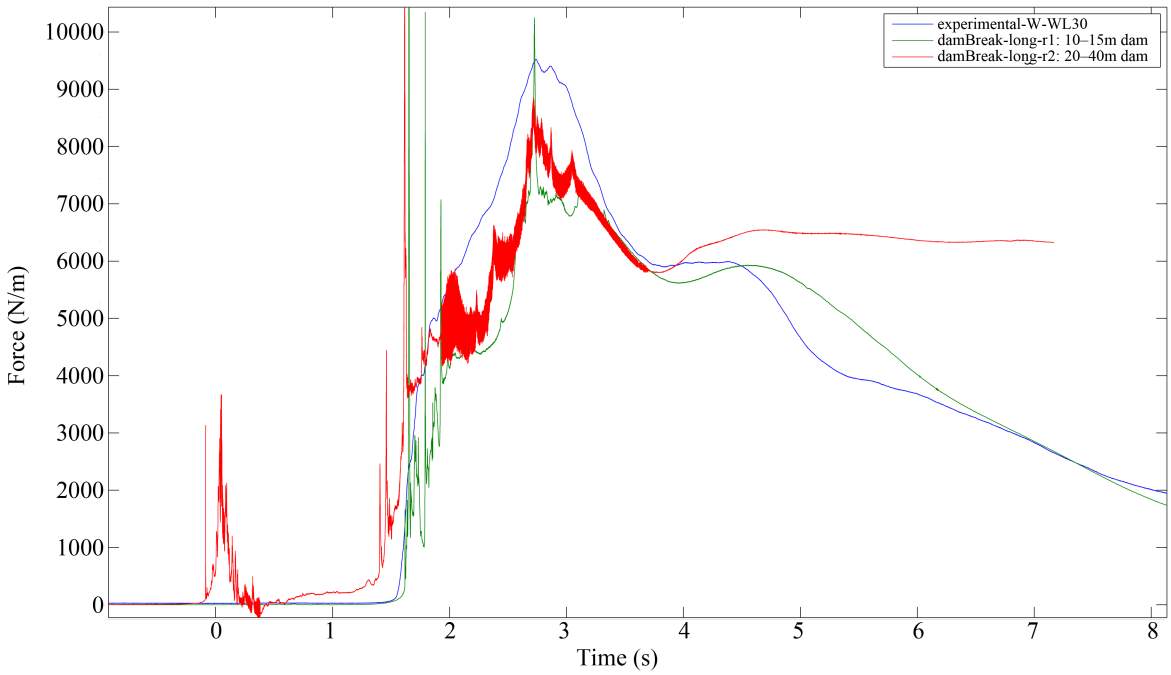

Figure 4.55. Comparison of results: small and large domain high quality grids and experimental data

4.5 Conclusions

The application of CFD to predict tsunami bore impact forces on a vertical wall has been investigated. A number of numerical tests were carried out to understand how best to simulate such an event. Three approaches to bore generation were investigated. The first simulated the actual experiments and the entire wave flume, in which a solitary wave was generated and caused to break at the beach-reef interface. A much smaller computational model involving just a section of the reef and an inflow velocity boundary condition to create the bore was also investigated. Finally, a dam break, where a water reservoir collapses and generates a bore similar in characteristics to the one created by a tsunami wave was simulated. This model also considered only a flat reef domain, but much longer than the inflow boundary condition.

The solitary wave model did not provide a good estimation of the wall force. The generated bores had different flow characteristics than those recorded during experimental tests. Nonetheless, the bore was created, which allowed to observe bore jet progress upon standing water level. Simulations revealed the initially still water level does not pick up the bore jet velocity instantaneously, but with some delay. During the delay period, the velocities of the bore were between 0 and 50% of the bore front velocity. For the available experimental data and numerically tested conditions, to accurately model wave breaking a more accurate study is required. In this particular case, the desired bore characteristics were not obtained. It is possible, the partial source of error comes from the interface-tracking scheme used in the volume of fluid method.

The inflow boundary model required only 1/3 of the previous domain length. This provided a significant reduction of computational effort. In this model it was assumed the bore height and velocity were known. The values used in the simulation were those recorded in previous TWB and LWF experiments. Different configurations were tested. The model that performed the best was the one with initially still water level and bore jet velocity that followed the experimental ADV recording, Case 1. The force time-histories and magnitudes were very similar to the experimental results. Such a model, however, in reality is hard to predict – the velocities are very random and ADV history is not enough to estimate a full-scale tsunami bore. Instead, simplified configurations were tested,

where the bore velocity was assumed constant along the whole height. The model that gave the best estimation was the one with still water level and constant inflow boundary along the height of the bore jet, where the inflow value of velocity equaled the maximum peak velocity extracted from ADV measurements, Case 5.

The dam break results matched experiments the best. The size of the domain was comparable to the full domain with a solitary wave. However, the length of the domain only depends on the time for which it is desired the load upon the wall should be sustained. The length of the water column defines the duration of the load at the wall.

The simulations revealed interesting bore flow characteristics. Some of the flow sustained for a long period of time revealed much higher loads following initial bore impact. This was a result of water load sustained for extended period of time, i.e. long dam or continuous boundary inflow.

All of the measured force results varied from each other. Those discrepancies are understandable and can be explained through highly fluctuating turbulent flow. Each of the grids provided different mesh resolutions and shapes. Hence, different turbulent scales across cells were used. The simulations also confirmed very high frequency pressure changes, larger than 1000 Hz. Simulations also gave insight that the solitary wave model possibly might not be sufficient to model full time-length tsunami bores, where the wave length is too short to provide accurate loads, where some of the peak loads could be missed. This indicates an additional area to extend in research.

In the solution process, if the computational effort is not an important factor, the dam break approach should be utilized. The predicted bore form was correct, with bore heights and velocities resulting in expected wall forces.

In cases where computational time is important, a reduced size domain with an inflow boundary can be used. The initial force build-up differs slightly from the one observed during the experiments, however, right after the initial impact, the maximum force measurement is very close to the expected result. The model allows use of much smaller domain size with high mesh resolution and provides acceptable results within a short time.

The turbulence model, which gave the closest force prediction is judged to be the κ–ω SST model. The model provided the most accurately predicted force time-histories in all of the considered tsunami bore models.

In general, the results showed quite high sensitivity to grid resolution with all the turbulence models. It is important to remember the grid resolution should be better in areas of interest, such as: wall zones, interfaces, areas of significant turbulence and bore formation, and most of all in the areas of instrumented specimens, where the pressure fluctuations upon impact are very large. Non-slip boundaries should be used, where appropriate wall treatment provides required surface friction to allow correct bore development. Additionally, in the cases with high water splash up, where water upon wall run-up might exit the computational domain, it should be assured the domain is extended, so the water volume stays within the domain.

Results presented herein do not present a verification of experimental results, but only set preliminary model definitions for the investigated tsunami bore generation techniques. The computationally tested cases do not provide a definite answer for the required mesh resolution and choice of a time step, which if chosen correctly should provide an accurate measure for tsunami bore force on a vertical wall. It is possible the three-dimensional effects play an important role in the fluid impact phenomenon. Large discrepancies in results indicate a more advanced study should be performed.

The proposed solution to the problem constitutes a foundation for future research and engineering applications for development of broken tsunami waves in near shore and coastal areas.

Chapter 5

Debris impact model

5.1 Overview

Impact from water-borne debris during tsunami and flood events pose a potential threat to structures. Debris impact forces specified by current codes and standards are based on rigid body dynamics, leading to forces that are dependent on total debris mass. However, shipping containers and other debris are unlikely to be rigid compared to the walls, columns and other structures that they impact. The application of a simple one-dimensional model to obtain impact force magnitude and duration, based on acoustic wave propagation in a flexible projectile, is explored. Based on small-scale experiments, the applicability of the model to predict actual impact forces is investigated.

5.2 Small scale debris impact experiment

Small-scale experiments were conducted to compare the one-dimensional (in-air) impact model with real impact data. The experimental setup was developed to represent direct, head-on impact by a projectile, Figure 5.1. The projectiles consisted of a standard rectangular steel tube 5.08 cm x 5.08 cm x 0.3175 cm, Figure 5.2. The projectile traveled along a guide system fabricated from steel angle sections, Figure 5.3. The rail guide, Figure 5.5, helped to obtain a direct impact. A 244 kN (55 kip) load cell (model MTS 661.23A–01) attached to a stiffened angle bracket represented the wall, Figure 5.4. A protective plate was bolted to the front of the load cell. The railing system was designed such that the impact occurred at the center of the load cell.

Four different length projectiles were used: 1, 2, 3, and 4 m long. Each projectile was instrumented with resistance-based strain gauges at three cross sections along the length: 5 cm from the front, in the middle, and 5 cm from the rear. At each instrumented cross-section, a strain gauge was placed on the front and backside of the tube. The strain sensors allowed the forces in the projectiles to be compared to the forces measured by the load cell, and to observe the wave propagation. Some trials for each projectile, however,

only recorded strains from the front two strain sensors. This allowed for a marginally higher recording frequency. Depending on the test configuration, data were recorded between 25 kHz and 50 kHz, with most of the data recorded around 30 kHz.

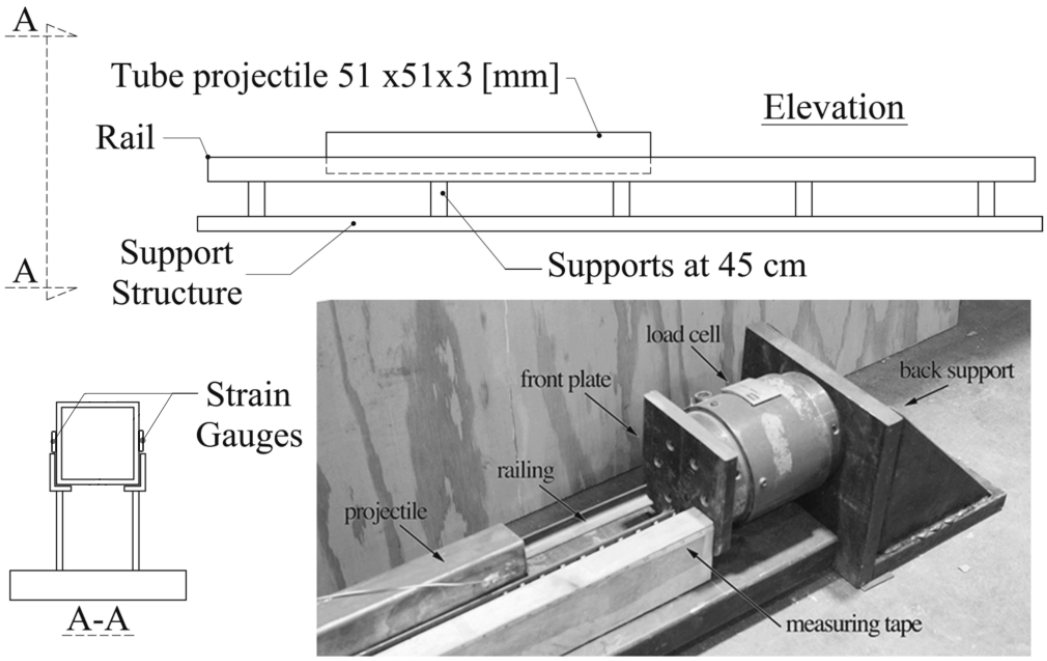

Figure 5.1. Experimental impact setup.

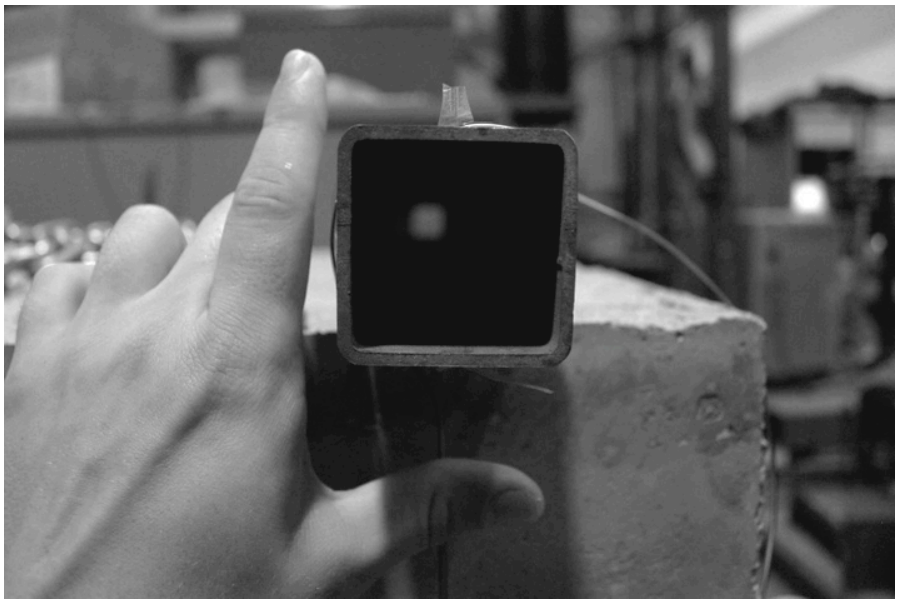

Figure 5.2. Tube section photo, 2x2x1/8 [in] / 5.08x5.08x0.3175 [cm].

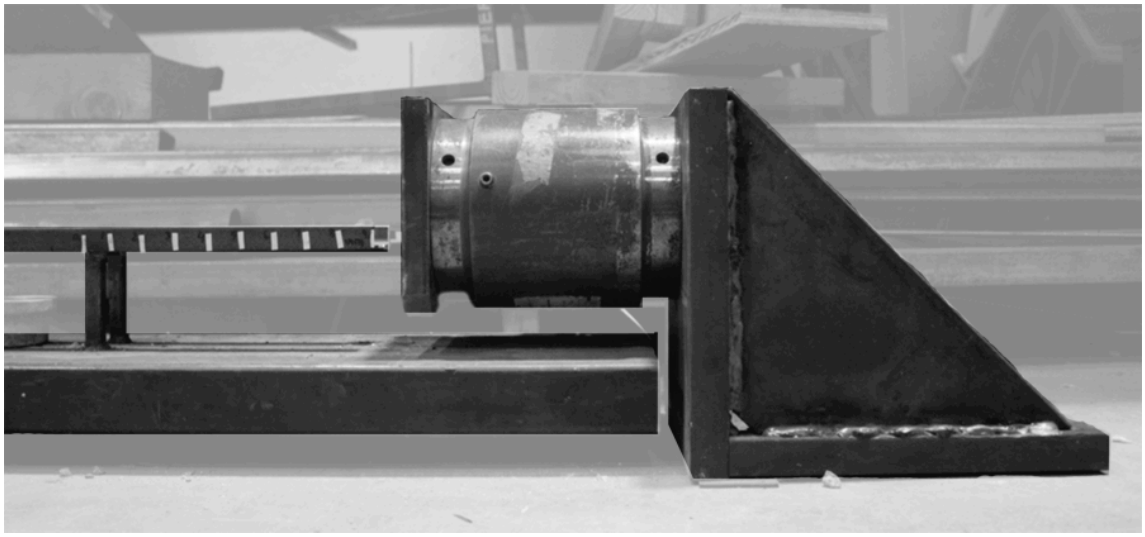

Figure 5.3. Experimental wall support: load cell in between front plate and angled support.

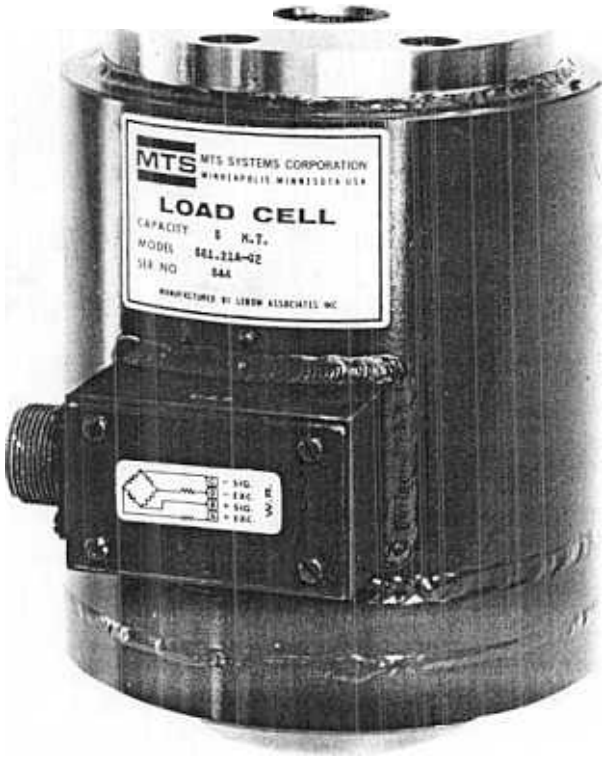

Figure 5.4. 244 kN (55 kip) load cell (model MTS 661.23A–01) [90].

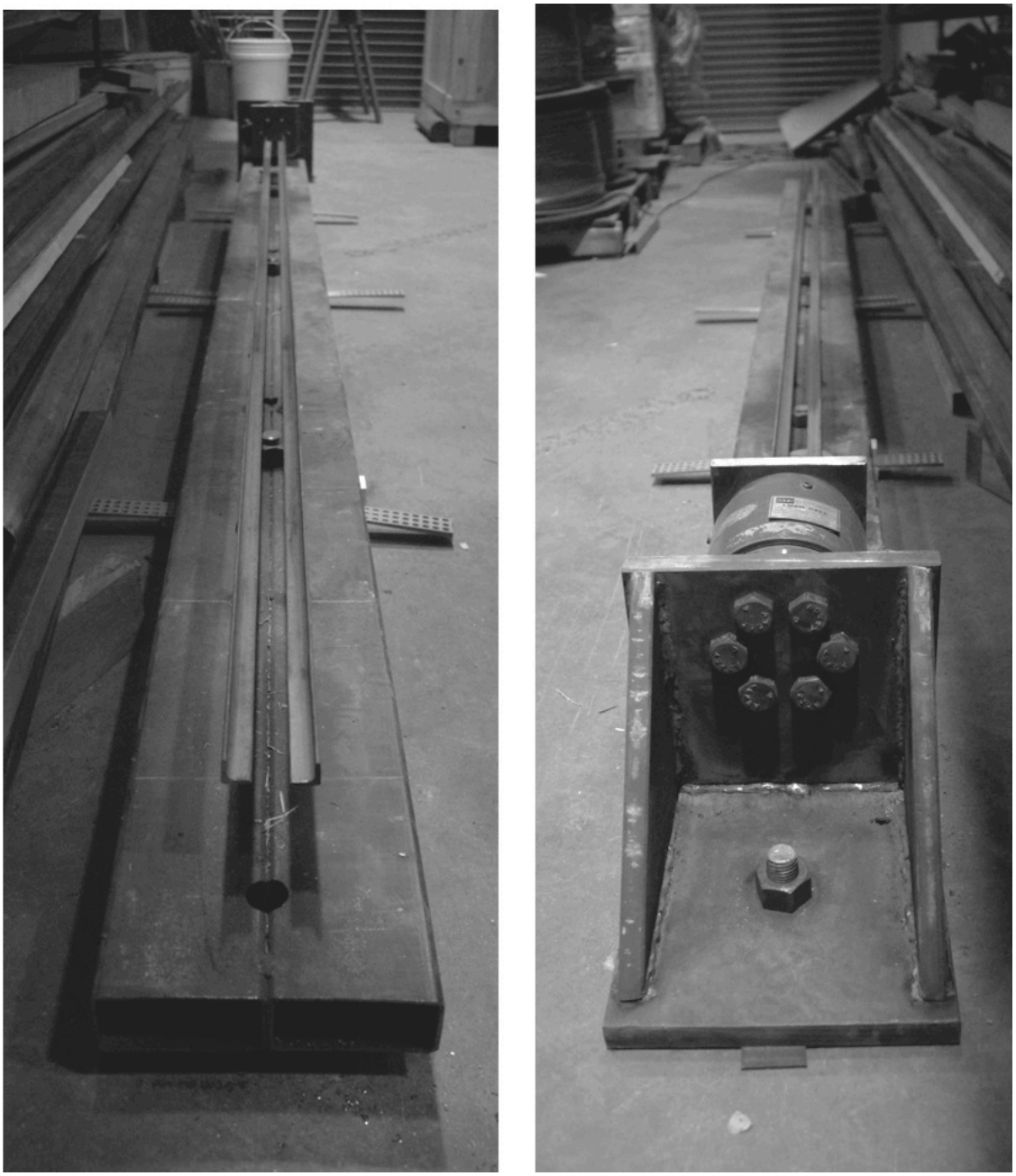

Figure 5.5. Railing system guiding the projectile impact:
left picture – the front view; right picture – back view from behind the load cell

The projectile was accelerated manually down the guide track. Impact velocity was determined through the use of high–speed video (1000 frames per second) and a fixed scale attached to the setup. The time stamp over a 2 cm length (i.e., when the debris was at 3 cm and 1 cm from the impact plate) was used to determine the impact velocity. The

location was determined with an accuracy of 0.5 mm and, based on the frame rate, the time stamp was determined with an accuracy of 0.5 msec. The error for the velocity measurements is therefore estimated at approximately ±6%.

The mass of the load cell was 14.916 kg, the 15 cm x 15 cm x 2 cm front plate had a mass of 3.376 kg, and the six screws that bolted the plate to the load cell were 0.082 kg total. Therefore, the total mass of the load cell setup, which was bolted to the back support, was 18.374 kg. The manufacturer-provided stiffness for the load cell is 2.97 x 10^6 kN/m (17 x 10^6 lbf/in).

In the following, the projectile properties are taken to be E_p = 210 GPa, A_p = 5.42 cm^2, and ρ_p = 7850 kg/m^3. The water-borne projectile is modeled as an elastic bar of length L_p pushed along by a semi-infinite horizontal column of fluid, as depicted in Figure 5.6.

5.3 Mathematical formulation

As an example, we will use a projectile approaching a wall structure with the velocity equal to the fluid velocity, Figure 5.6. We assume the projectile velocity equals the fluid velocity. It is a conservative assumption, which provides the highest possible velocity for the projectile.

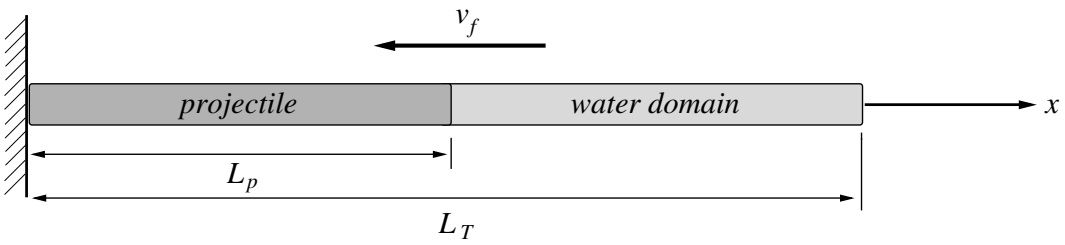

Figure 5.6. Projectile and water column

The projectile is propelled to the left with speed v_f. When the left end of the projectile hits the 'wall', an acoustic wave propagates from left to right. The one-dimensional wave equation governs the acoustic wave in both the projectile and the fluid

$$\frac{\partial^2 u(x,t)}{\partial t^2} - c^2 \frac{\partial^2 u(x,t)}{\partial x^2} = 0 \tag{5.1}$$

in which $u(x,t)$ is the displacement field and c is the speed of sound in the medium. In the projectile, the speed of sound is given by

$$c_p = \sqrt{\frac{E_p}{\rho_p}} \tag{5.2}$$

in which E_p is the Young's modulus, A_p is the cross–sectional area, and ρ_p is the mass density. The water is characterized by the speed of sound c_f, mass density ρ_f, and the bulk modulus $K_f = c_f^2 \rho_f$.

The solution to equation (5.1) is

$$u(x,t) = f_1(x - c_p t) + f_2(x + c_p t) \tag{5.3}$$

in which f_1 and f_2 are arbitrary wave propagation functional relationships of $x - c_p t$ and $x + c_p t$. Equation (5.3) represents a pair of displacement waves propagating in the positive and negative direction respectively, Figure 5.7.

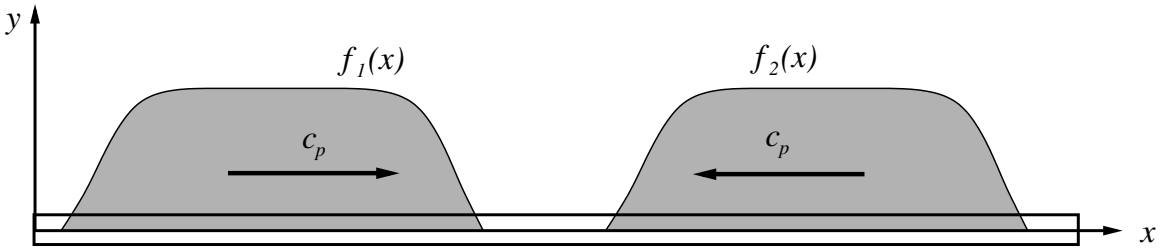

Figure 5.7. f_1 and f_2 are wave propagation functions.

The function defining the shape of any wave propagating through a uniform bar is controlled by the conditions imposed at the ends of the bar. The waveform within a bar is generated by the requirements of equilibrium and compatibility at the boundaries.

5.4 Impact without water

First consider the case of the projectile hitting a rigid wall with no fluid. In that case the initial conditions are

$$u(x,0) = 0, \quad \dot{u}(x,0) = -v_f \tag{5.4}$$

and the boundary conditions are

$$u(0,t) = 0, \qquad u_{,x}\left(L_p,t\right) = 0 \tag{5.5}$$

To impose the zero displacement at the left end, one can write for a differential segment the constraint at impact

$$-v_f dt - \varepsilon_p dx = 0 \tag{5.6}$$

in which ε_p is the strain in the projectile and $dx = c_p dt$ is the differential segment through which the stress wave has propagated. Equation (5.6) results in

$$\varepsilon_p = -\frac{v_f}{dx/dt} = -\frac{v_f}{c_p} \tag{5.7}$$

The force in the projectile at $x = 0$ (i.e., the impact force on the wall) is then given by

$$F = -\frac{E_p A_p}{c_p} v_f \tag{5.8}$$

or

$$F = -v_f A_p \sqrt{E_p \rho} = -\rho A_p c_p v_f \tag{5.9}$$

in which A_p is the structural area of the projectile and ρ is the density of the projectile. Equation (5.8) is a well-known result [91-93] and implies that the error in force based on the measured velocities will have a similar error as the velocites. Note that this force does not depend on the total projectile mass, as is assumed in equations (2.8)–(2.10). The impact force is constant as the stress wave propagates down the projectile until it reaches the free end at time $t_L = L_p/ c_p$. It is then reflected back to maintain the stress free condition at $x = L_p$. Hence, the force in the projectile is

$$F = \begin{cases} -\frac{E_p A_p}{c_p} v_f H(c_p t - x), & 0 \le t \le t_L \\ -\frac{E_p A_p}{c_p} v_f H[2c_p(t_L - t) - x], & t_L \le t \le 2t_L \end{cases} \tag{5.10}$$

in which H is the Heaviside step function. At time $2t_L$ the reflected wave has reached the wall. The force would then become tensile, except this means the projectile separates from the wall and the impact is over. Hence, the constant force of impact is given by equation (5.8) and its duration, t_D, is $2t_L$.

Note that, if the contact stiffness in equation (2.10) equals $\frac{EpAp}{Lp}$, the equation equals equation (5.8). Similarly, when $\Delta t = t_L$, equation (2.9) becomes equal to equation (5.8) multiplied by a factor of $\pi/2$ =1.57.

5.5 Non–dimensional formulation

At this point it is worthwhile to nondimensionalize the formulation. Length variables are nondimensionalized by L_p, such that $\bar{x} = x/L_p$ and $\bar{u} = u/L_p$. Nondimensional time is $\bar{t} = t/t_L = tc_p/L_P$, while nondimensional force $\bar{F} = F/\left(-\frac{E_p A_p}{c_p} v_f\right)$. The result is to nondimensionalize velocity by c_p. The wave equation becomes

$$\frac{\partial^2 \bar{u}}{\partial \bar{t}^2} - \frac{\partial^2 \bar{u}}{\partial \bar{x}^2} = 0 \tag{5.11}$$

with initial conditions

$$\bar{u}(\bar{x}, 0) = 0, \quad \dot{\bar{u}}(\bar{x}, 0) = -\bar{v}_f \tag{5.12}$$

and boundary conditions

$$\bar{u}(0, \bar{t}) = 0, \qquad \bar{u}_{,\bar{x}}(1, \bar{t}) = 0 \tag{5.13}$$

5.6 Contact stiffness without water

Now consider the case where there is a Hertzian-type contact stiffness between the projectile and the wall (alternatively, the wall can be viewed as flexible but massless). The stiffness is represented by a simple linear spring of stiffness k_c. The nondimensional

stiffness is defined as $\bar{k} = k_c/(E_p A_p/L_p)$. The initial conditions are unchanged, but the boundary condition at the left is

$$\bar{k}\bar{u}(0,\bar{t}) - \bar{u}_{,\bar{x}}(0,\bar{t}) = 0 \tag{5.14}$$

which simply states that the force in the contact spring is equal to the force in the projectile at the contact point.

The solution can be represented fairly simply using the well-known separation of variables and modal superposition method. That is, the solution is of the form

$$\bar{u}(\bar{x},\bar{t}) = \sum_{n=0}^{\infty} \phi_n(\bar{x})\, Y_n(\bar{t}) \tag{5.15}$$

For the given initial and boundary conditions, the solution is

$$\bar{u}(\bar{x},\bar{t}) = -\bar{v}_f \sum_{n=0}^{\infty} \frac{\dot{Y}_n(0)}{Z_n} \sin(Z_n\bar{t})\, \phi_n(\bar{x}) \tag{5.16}$$

in which

$$\dot{Y}_n(0) = \frac{4}{2\,Z_n\left(\frac{Z_n^2}{\bar{k}^2}+\frac{1}{\bar{k}}+1\right) - \frac{2\,Z_n}{\bar{k}}\cos(2\,Z_n) + \left(\frac{Z_n^2}{\bar{k}^2}-1\right)\sin(2\,Z_n)} \tag{5.17}$$

and

$$\phi_n(\bar{x}) = \sin(Z_n\bar{x}) + \frac{Z_n}{\bar{k}}\cos(Z_n\bar{x}) \tag{5.18}$$

Z_n are the eigenvalues determined from

$$Z_n \tan(Z_n) = \bar{k} \tag{5.19}$$

Knowing $\omega_n = \frac{Z_n c_p}{L_p} = \frac{Z_n}{t_L}$, where $t_L = \frac{L_p}{c_p}$ we can write $Z_n t = \omega_n \bar{t}$ with $\bar{t} = \frac{t}{t_L}$, hence

$$u(x,t) = v_f t_L \sum_{n=0}^{\infty} \frac{1}{Z_n} \dot{Y}_n(0) \sin(Z_n\bar{t})\, \phi_n(x) \tag{5.20}$$

and

$$u(0,t) = \frac{v_f t_L}{\bar{k}} \sum_{n=0}^{\infty} \frac{1}{Z_n} \dot{Y}_n(0) \sin(Z_n\bar{t}) \tag{5.21}$$

Therefore

$$F(0,t) = F\sum_{n=0}^{\infty} \dot{Y}_n(0)\sin(Z_n\bar{t}) \tag{5.22}$$

If $\bar{F} = F(0,t)/F$ then the nondimensional force on the wall can be determined as

$$\bar{F}(0,\bar{t}) = \sum_{n=0}^{\infty} \dot{Y}_n(0)\sin(Z_n\bar{t}) \tag{5.23}$$

A convergence study showed that the first 50 terms of the series provides a maximum force within 0.001 of the limiting maximum force, for values of $\bar{k}$ that were tested. The results for different $\bar{k}$ values are presented in Figure 5.8. For a rigid contact stiffness, $\bar{F} = 1$ and the nondimensional duration is 2. The results show that for $\bar{k} = 40$, the response is nearly the same as for rigid contact. As $\bar{k}$ decreases, the duration increases and the maximum impact force eventually begins to decrease, compared to the impact force with rigid contact.

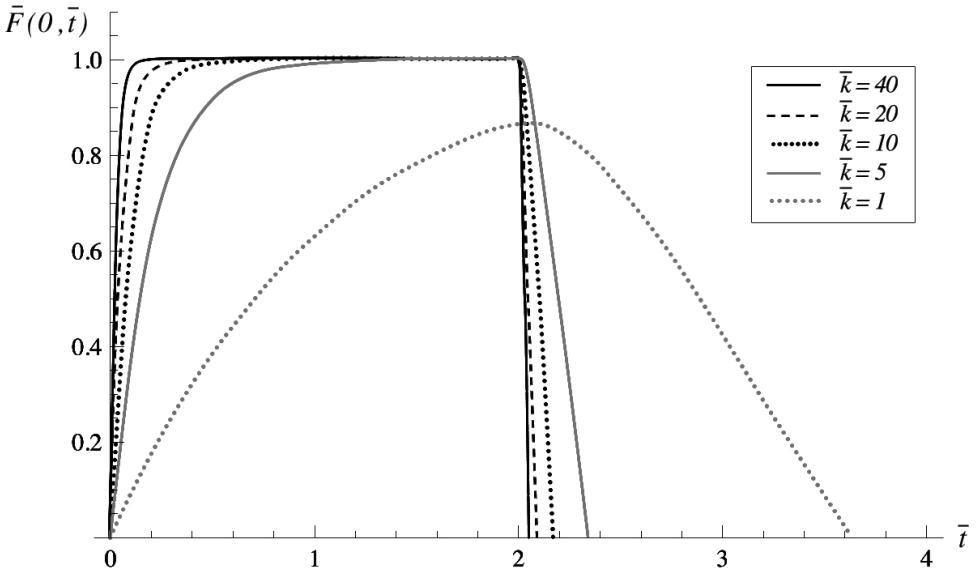

Figure 5.8. Nondimensionalized force vs. time for different values of stiffness ratio $\bar{k}$

Based on the load cell stiffness and the area and modulus of the projectile, $\bar{k}$ in the experiments varied from 26 for the 1 m projectile to 104 for the 4 m projectile. It was anticipated that the results would be similar to the rigid wall response.

5.7 Fluid-driven impact

To estimate the influence of the water on the impact force, the water is modeled as an infinitely long column of water behind the projectile, Figure 5.6, or at least sufficiently long such that during the time of interest acoustic waves in the water propagate only in the $+x$ direction. The water is confined to the column, and hence there is only one-dimensional wave propagation. This is a conservative assumption, as it will overestimate the influence of the fluid on the impact force. The water and projectile are assumed to have the same initial velocity, $-v_f$. The fluid pressure is defined by $p = K\varepsilon_v$, where ε_v is the volumetric strain. However, in this case $\varepsilon_v = \partial u/\partial x$ in the fluid.

At the interface between the projectile and the fluid, the velocities of the projectile and fluid must be equal, which in this case means the displacements are equal. Similarly, the force in the projectile at $\bar{x} = 1$ must be equal to the integrated pressure in the fluid. Some projectiles, such as a shipping container, will have an area A_f exposed to the fluid that is much different than the 'structural' area A_p that contributes to the stiffness E_pA_p. The nondimensional interface area is defined as $\bar{A} = A_f/A_p$. The compatibility equation for force can then be written as

$$\bar{u}_{p,\bar{x}} = \bar{c}^2\bar{\rho}\bar{A}\bar{u}_{f,\bar{x}} \tag{5.24}$$

in which $\bar{c} = c_f/c_p$ and $\bar{\rho} = \rho_f/\rho_p$.

The fluid will not feel the impact until the stress wave reaches the interface at time $\bar{t} = 1$. At that time, part of the wave will be transmitted to the fluid and part will be reflected back from the interface. The interface can be replaced by reflection and transmissibility coefficients, R and T, respectively, that give the proportions of the wave that are reflected by the fluid interface and transmitted to the fluid. Expressions for the coefficients are obtained by imposing the interface conditions. In the first interval $0 < \bar{t} < 1$ wave propagates towards the fluid, Figure 5.9.

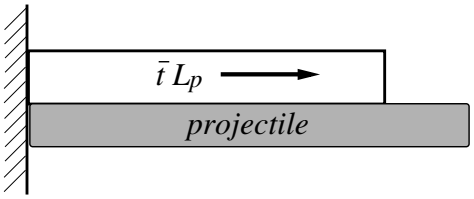

Figure 5.9. Force propagation: first time interval; $0 < \bar{t} < 1$.

From the continuity condition at the interface we can define

$$u_p = \int_0^{L_p} \varepsilon_p dx \tag{5.25}$$

and

$$u_f = \int_0^t v_f dt - \int_0^{c_f(t-t_L)} \varepsilon_f dx \tag{5.26}$$

By comparing the two displacements, we can see the continuity condition is satisfied, i.e. $u_p = u_f$.

At the second time interval, $1 < \bar{t} < 2$, the wave reflects and returns, Figure 5.10.

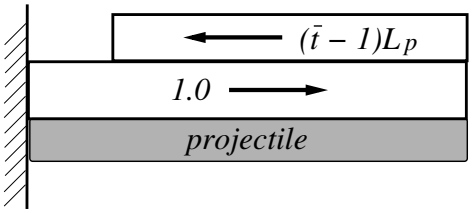

Figure 5.10. Force propagation: reflected wave return path, $1 < \bar{t} < 2$.

Defining displacements for the second interval

$$u_p = \underbrace{v_f t_L}_{\substack{response\ from \\ the\ first\ interval \\ 0<t<t_L}} + \int_{L_p - c_p(t-t_L)}^{L_p} R \frac{v_f}{c_p} E_p A_p \frac{1}{E_p A_p} dx \tag{5.27}$$

$$u_f = v_f t - \int_0^{c_f(t-t_L)} \frac{v_f}{c_p} E_p A_p (1+R) \frac{1}{E_f A_f} dx \tag{5.28}$$

Equating both displacements, the magnitude of the reflection coefficient can be obtained as

$$R = \frac{A_f c_f \rho_f - A_p c_p \rho_p}{A_f c_f \rho_f + A_p c_p \rho_p} \tag{5.29}$$

or in non-dimensional terms

$$R = \frac{\bar{A}\,\bar{c}\,\bar{\rho} - 1}{\bar{A}\,\bar{c}\,\bar{\rho} + 1} \tag{5.30}$$

and $T = 1 + R$. Note that $-1 \leq R \leq 1$. When the fluid is air, then R = –1 and all the wave is reflected back; this is the case discussed in section 5.4. When the projectile and the fluid are the same material and $\bar{A} = 1$, $R = 0$ and there is no reflection. In this case the impact force is $\bar{F} = 1$ and it lasts for infinity. In general, however, the wall will feel the reflected wave at $\bar{t} = 2$. The force it feels at that time is $(1 + R)$. The reflected wave is again reflected at the wall. For a rigid wall, the reflection is 100% and the force after reflection is $(1 + 2R)$. If $R < 0$, the fluid does not increase the magnitude of the impact force, and if $R > 0$, the fluid will increase the impact force. Hence, it appears that it may be possible to use R to quantify the effect of the so-called 'added mass', in the sense of how much the fluid increases the impact force.

By considering the waves propagating back and forth, the following series for the force at the wall can be obtained:

$$\bar{F} = 1 + 2R + 2R^2 + 2R^3 + 2R^4 + 2R^5 + 2R^6 + 2R^7 + 2R^8 + \cdots \tag{5.31}$$

The first term in the geometric series is the initial impact force, $1 + 2R$ is the force starting at $\bar{t} = 2$, $1 + 2R + 2R^2$ is the force starting at $\bar{t} = 4$, etc. Clearly, the sequence should stop when $\bar{F} \leq 0$, at which point separation occurs. If $R \leq -0.5$, separation occurs at $\bar{t} = 2$. If $R > -0.5$, separation never occurs and hence the duration of impact increases. The asymptotic value of equation (5.31) is $\bar{A}\,\bar{c}\,\bar{\rho}$. Especially when the fluid increases the force, it is unlikely the above formula is applicable beyond a cycle or two, after which three-dimensionality effects in the water will likely predominate. Any amplification in the force as a result of the fluid is likely limited to $(1 + 2R)$ or more likely much less.

Typical debris will be either steel (e.g., shipping containers) or wood (logs and telephone poles). If it is assumed that for seawater $\rho_f = 1025\ kg/m^3$ and $c_f = 1560\ m/s$, and for steel $\rho_p = 7850\ kg/m^3$ and $c_p = 5960\ m/s$, then $\bar{\rho} = 0.13$ and

$\bar{c} = 0.26$. For wood with $\rho_p = 550\ kg/m^3$ and $c_p = 3500\ m/s$, $\bar{\rho} = 0.54$ and $\bar{c} = 0.45$. For the water to increase the duration of impact, $R > -0.5$. From equation (5.30), this implies $\bar{A}\bar{c}\bar{\rho} > 1/3$. This corresponds to $\bar{A} > 9.8$ for a fully submerged steel projectile and $\bar{A} > 1.4$ for a fully submerged wood projectile. If a log or telephone pole is half-submerged, the nondimensional area would be around 0.5, and therefore for woody debris it is likely that the fluid will not increase the impact duration or force (even if it were fully submerged). However, for typical shipping container dimensions, the container end area is approximately 800 times the structural area, i.e., the area of the longitudinal beams at the four corners. The draft for empty and full 12 m shipping container is 0.12 and 1 m, respectively. Although the formulation depends on the draft, R may be greater than 0.8 and the impact duration will increase and the maximum impact force might be up to 2.5 to 3 times (based on $1 + 2R$) to what it would be in-air. In addition, separation will not occur. Note that this is a conservative estimate.

5.8 Experimental results and comparison with proposed approach

Twelve trials were run for each of the four projectile lengths. Of the 48 trials, not all the data recorded properly in 4 trials, resulting in 44 trials with a full complement of data. During the trials, the force in the load cell and strains in the projectiles were measured, Figure 5.11 presents the load cell force-time history results for five trials using the 2 m projectile. All twelve trials had very similar time histories. For clarity in the figure, only five trials are presented. The remainder of the results for all the other tests is included in Appendix A. The measured forces have been non-dimensionalized by the theoretical impact force from equation (5.8). As illustrated, the various trials produced repeatable results with similar histories and maximums. This behavior is typical of the other trials conducted. Variations between the cases shown may be related to uneven impact against the front plate due to, e.g., the moderate lateral tolerances in the guide rail, the manual acceleration of the projectile, and/or fabrication tolerance of the tube face.

The analytical impact force time history due to the projectile impacting a rigid wall is compared to the measured reaction force in Figure 5.11. As illustrated the proposed model provides a good approximation of the expected maximum impact force and

duration. The gradual increase in impact force, as compared to the sudden jump in the 1-D model, may be caused by uneven contact surfaces between the projectile and the front plate on the load cell, resulting in a finite contact stiffness. It should also be noted that the theory gives the impact force, whereas the experiments measured the force in the load cell. Analysis of the free-vibration response of the load cell after impact revealed that the first natural period of the load cell and support bracket combination was approximately 4 ms for the 1, 2 and 3 m projectiles and 3.6 ms for the 4 m projectile (reassembling the test setup between these two sets of experiments led to the change in period). The oscillations in the measured forces during impact that are observable in Figure 5.11 have a period of approximately 0.20 – 0.22 ms, well below the first natural period of the load cell.

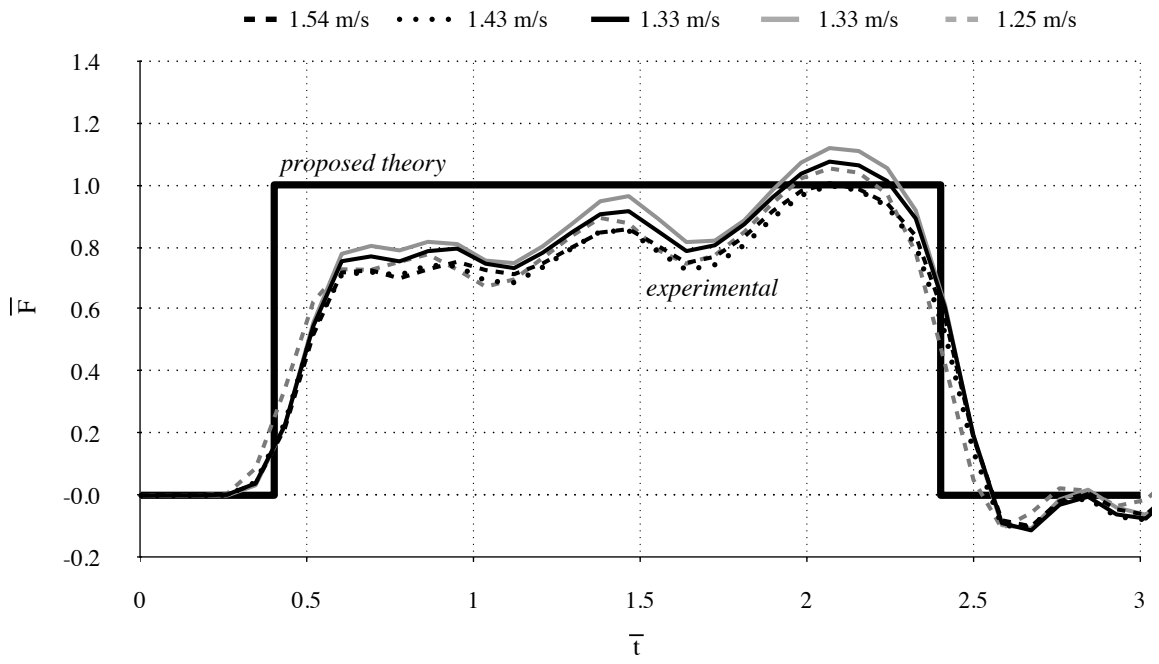

Figure 5.11. Normalized load cell histories for 2 m projectile

The gradual rather than abrupt increase in impact force is consistent with other impact experiments [94]. To represent a more gradual impact demonstrated by the experimental forces, results for the model with a contact stiffness were obtained for the 2 m projectile. To match the slope in the force time history, a value of $\bar{k} = 6.0$ was used. Results are compared in Figure 5.12. The dotted black line represents one of the experimental trials (2 m long projectile with 1.67 m/s velocity) and the black solid line shows the calculated force.

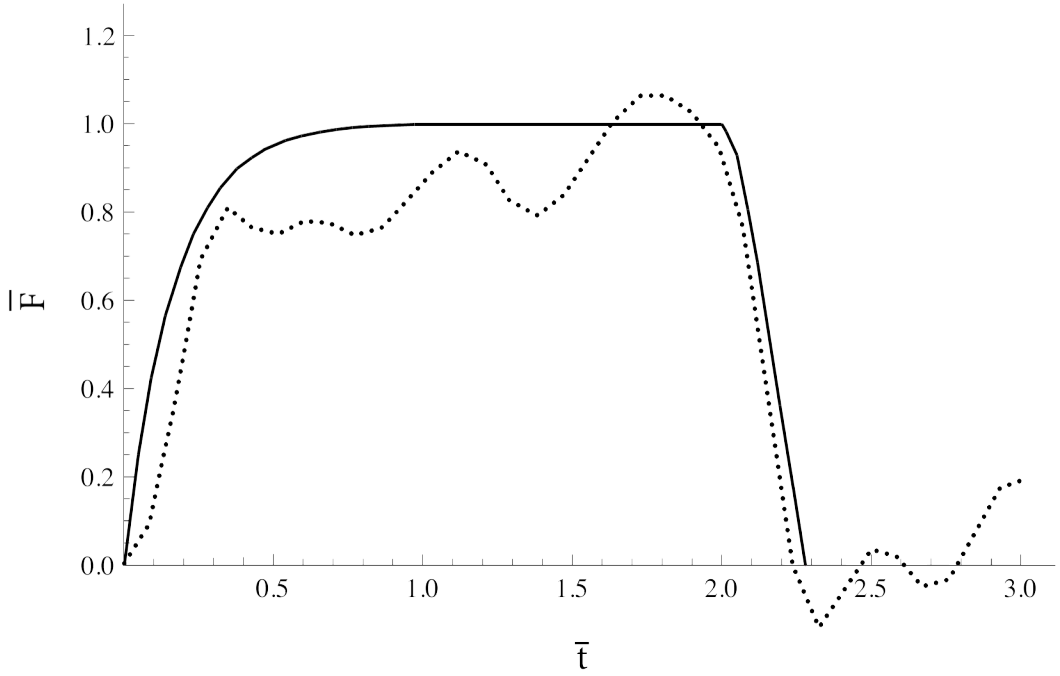

Figure 5.12. Response with contact stiffness $\bar{k}$ = 6.0: dotted black line is experimental data; solid black line is calculated result.

The nondimensionalized maximum force in the load cell versus impact velocities for recorded cases is shown in Figure 5.13. These results agree with the proposed one-dimensional analytical model ($\bar{F} = 1$). The variation in the measured impact force relative to the theoretical force ranges from 0% to 27%. For the 1 m, 2 m, 3 m, and 4 m projectiles, the average errors were 20%, 5%, 2% and 11%, respectively. The largest discrepancy occurred for the 1 m projectile, the reason for which is unclear; it could be that the smaller mass was insufficient to ensure full contact with the plate after the impact. The magnitude of error for the 4 m projectile is due likely to the specimen length, which was longer than the rail guide. To provide physical scale, it is noted that the impact force from eq. (9) is 22 kN at 1 m/s and 44 kN at 2 m/s. Consistent with theory, the impact force does not depend on the total mass of the projectile.

It is interesting to compare these results with the predicted values from equation (2.9). When equation (2.9) is nondimensionalized with equation (5.8), and Δt is taken to be t_L, equation (2.9) is increased by π/2, or approximately 1.57. However, ASCE 7 suggests Δt = 0.03 s, whereas for the 2 m projectile Δt = 0.00077 s. A shipping container would have

a Δt three to six times longer. Therefore, following ASCE 7 may underpredict the actual impact force.

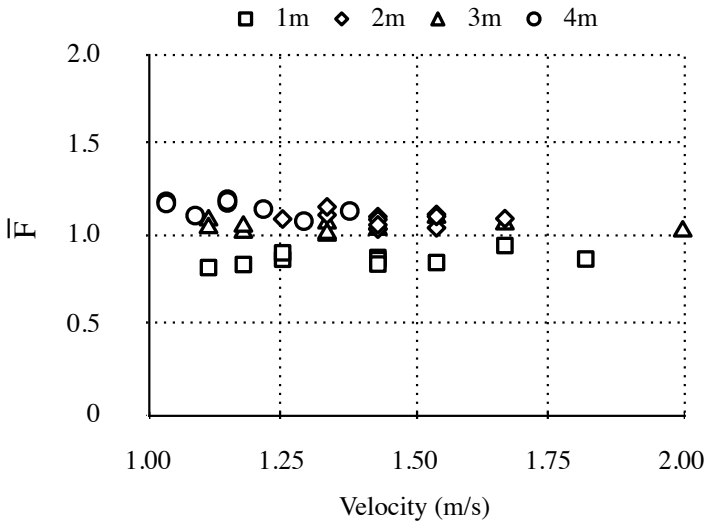

Figure 5.13. Normalized measured impact force versus impact velocity

The model accuracy for impact duration was examined for each case. The non-dimensional durations are shown in Figure 5.14. From the force time histories, such as shown in Figure 5.11, the duration of impact was determined as follows. The start time was defined as the point where the force recording exceeded at least 1% of the maximum recorded force value. The end time was defined as the point at which the force becomes zero. In some cases, the force did not reach zero. Instead, for a very short duration of time, the force decreased to a very low value followed by a rise. In those cases, end time was defined as the time at minimal peak force in the sustained force plateau. The measured time durations were nondimensionalized by t_L. For a 1 m projectile, 2 t_L is approximately 0.387 ms. This value can be multiplied by the projectile length to obtain the factors for other lengths. The results agree reasonably well with the one-dimensional analytical model ($\bar{t}_D = 2$), although the actual durations are consistently longer. This is due likely to the gradual, initially uneven contact.

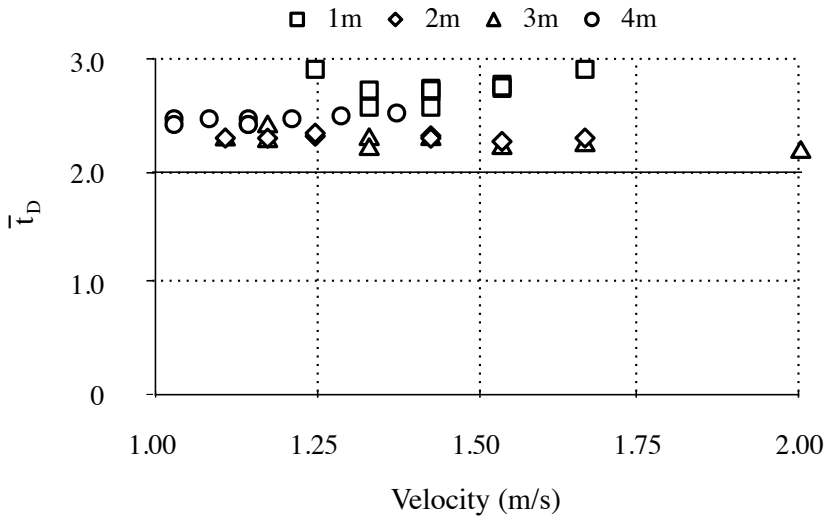

Figure 5.14. Load duration versus impact velocity for different length projectiles

The force time histories, such as in Figure 5.11, were integrated to obtain the total force impulse as a result of impact. These values are compared with the theoretical value of 2.0, Figure 5.15. Even though the theoretical duration underpredicts the experimental value, the theoretical value for impulse overpredicts the impulse. Hence, the theoretical model is conservative in terms of impulse.

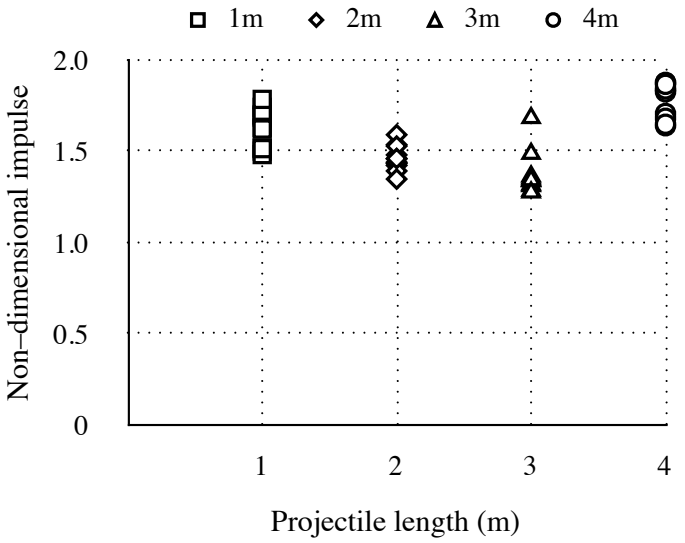

Figure 5.15. Impulse calculated for nondimensionalized time and force quantities

The strain recordings were used to extract the propagation speeds in each of the projectiles. For each of the projectiles, two trials with 6 strain sensors were used to verify the speed of sound. For each of the strain gauge locations, the strain increase time stamp was extracted and, based on the projectile length, the propagation speeds were calculated. The extracted values resulted in approximately c_p = 5600 m/s, which is within the range of values for steel provided in the literature. The average strain time histories at two sections for the 2 m projectile with six strain gauges and 1.54 m/s velocity are shown in Figure 5.16.

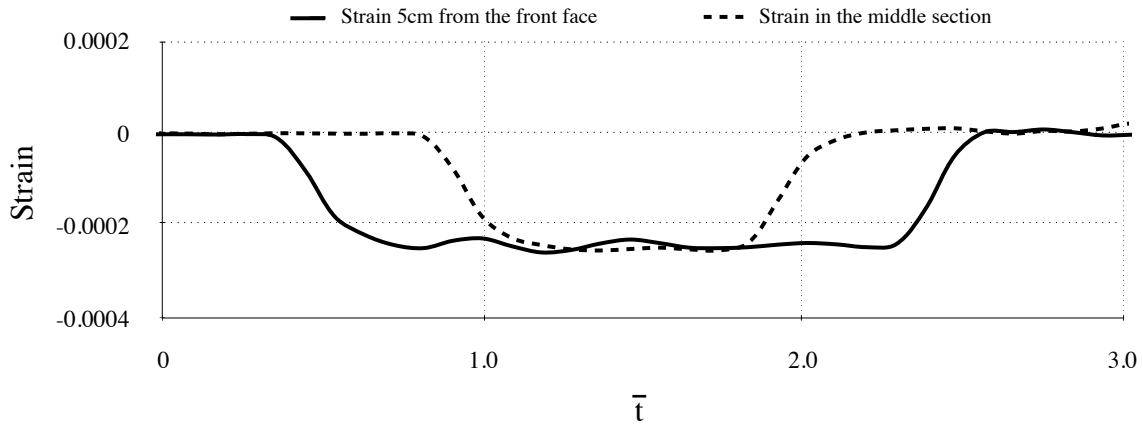

Figure 5.16. Sample strain time history for one of the trials

Forces can be calculated from the measured strains by multiplying by E_pA_p. The agreement of these forces with the measured forces, however, varied widely, with errors between nearly 0% and 100% (although the maximum errors were only obtained for 2 trials for the shortest projectile). The reasons for the wide variation are unclear. A likely reason for the discrepancies is that the two strain sensors are not sufficient to track the strain distribution along the cross sectional perimeter of the tubes. This indicates that more strain gauges around the cross section should be used. For both the load cell forces in Figure 5.11 and the strains in Figure 5.16, the times to reach the first maximum after initial impact were similar. This would imply that the gradual rise in impact force shown in the load cell is due not to the dynamics of the load cell, but to the impact between the projectile and the front plate.

5.9 Summary

A simple one-dimensional analytical model has been developed to estimate the force time history imparted to structures subjected to longitudinal impact from debris. Based on results from a small scale experimental program, the model gives good agreement for both the maximum impact force and the duration of impact. It also confirms that for the impact scenario considered herein, the maximum impact force does not depend on the total mass of the debris. The analytical model has been enhanced to include the acoustic waves in a water column behind the projectile.

Chapter 6

Conclusions

6.1 Lateral load on a vertical wall

Based on data from a previous experimental laboratory study to quantify the lateral load applied to a vertical wall when subjected to different size tsunami bores, a method is proposed to predict the peak lateral force on the vertical wall given only the incoming jump height, h_j, and the standing water depth, d_s.

The following conclusions are made. The hydrodynamic forces on the wall are much larger than typical lateral design forces. Non-structural walls will likely break away under these loads, thereby reducing the tsunami load on the structural frame. Nonetheless, structural walls must be able to resist the tsunami loads so that they continue to support the building gravity loads. The proposed design equation provides a good estimate of the experimental force for various bore heights and standing water depths. The average error for a particular standing water level was generally around 10%. This is an improvement over prior expressions found in the literature. Although the design equation was developed for scaled model results, it can be used for prototype scale following Froude scaling. The proposed design equation assumes that the main impact force comes from the incoming jet of water, described here as a 'jump height'. While such an approach might not resemble the actual impact phenomena, for design purposes it appears to be sufficient. The dry bed condition should be investigated further.

Computational model investigation was also shown and can be used as a guideline for future numerical study. Different bore generation techniques were investigated and the most accurate approaches were proposed. Further investigation of viability of such approach should be devoted to large-scale study, i.e. an assembly of different members including whole structures.

6.2 Fluid driven debris impact

In the latter part of the dissertation, a simple one-dimensional analytical model has been developed to estimate the force time history imparted to structures subjected to longitudinal impact from debris. The model is based on stress propagation in a one-dimensional bar. Based on results from a small-scale experimental program, the model gives good agreement for both the maximum impact force and the duration of impact. In addition the method provides a conservative estimate of impulse energy. It is clear that real impact does not involve immediate and full contact between the debris and the structure. The result is that the sudden impact, which would otherwise occur, is actually a gradual impact that builds up to the maximum impact force. As shown, addition of a 'contact stiffness' can replicate this behavior. The results indicate that the model provides an accurate estimation of the peak impact force and its duration. It also confirms that for the impact scenario considered herein, the maximum impact force does not depend on the total mass of the debris, as is often assumed in code provisions based on rigid body impact. For large and heavy debris, such as shipping containers, this may be an important point. The results are also useful to aid in the design of larger scale impact experiments, such as with full scale shipping containers, so as to quantify impact forces that might be experienced in the field.

The analytical model has been enhanced to include the acoustic waves in a water column behind the projectile. This model indicates that the fluid may increase the force and/or duration of the impact and the parameters that control this. Only the small time-scale acoustic response of the impact event has been considered here. Further work should also consider the longer time-scale gravity waves induced by the impact event, including the free surface. The model is currently under further development [96].

List of References

[1] L.C. Reese, H. Matlock, 1968, 'Structural damage from tsunami at Hilo, Hawaii', Journal of the Hydraulics Division, Proceedings of the American Society of Civil Engineers, HY 4, pp. 961-982.

[2] J.P. Eaton, D.H. Richter, W.U. Ault, 1961, 'The tsunami of May 23, 1960, on the Island of Hawaii', Bulletin, Seismological Society of America, 51, pp. 135-157.

[3] J.T. Kozak, C.D. James, 2008, Historical depictions of the 1755 Lisbon earthquake, http://nisee.berkeley.edu/lisbon/, February 28, 2011.

[4] Wikipedia, 2008, 1755 Lisbon earthquake, http://en.wikipedia.org/wiki/1755, February 28, 2011.

[5] G. Pararas-Carayannis, 1997, The great Lisbon earthquake and tsunami of 1 November 1755, http://www.drgeorgepc.com/Tsunami1755Lisbon.html, February 28, 2011.

[6] J.D. Ramsden, 1993, Tsunamis: Forces on a vertical wall caused by long waves, bores, and surges on a dry bed, Ph.D. dissertation, California Institute of Technology, Pasadena, California, USA.

[7] B.H. Choi, E. Pelinovsky, K.O. Kim, J.S. Lee, 2003, 'Simulation of the transoceanic tsunami propagation due to the 1883 Krakatau volcanic eruption', Natural Hazards and Earth System Sciences, 3, pp. 321-332.

[8] M. Nakao, 'The great Meiji Sanriku tsunami, June 15, 1896 at the Sanriku coast of the Tohoku region', Institute of Engineering Innovation, School of Engineering, The University of Tokyo.

[9] G. Pararas-Carayannis, 1999, 'Analysis of mechanism of the giant tsunami generation in Lituya Bay on July 9, 1958', Science of Tsunami Hazards, 17, pp. 193-206.

[10] B.W. Wilson, A. Torum, 1964, 'The tsunami of the alaskan earthquake', Evaluation TM No. 25 USACE, Coastal Engineering Research Center.

[11] H. Kanamori, K. Masayuki, 1993, 'The 1992 Nicaragua earthquake: a slow tsunami earthquake associated with subducted sediments', Nature, pp. 714 - 716.

[12] T. Lay, H. Kanamori, C.J. Ammon, M. Nettles, S.N. Ward, R.C. Aster, S.L. Beck, S.L. Bilek, M.R. Brudzinski, R. Butler, H.R. De Shon, G. Ekstrom, K. Satake, S. Sipkin, 2005, 'The great Sumatra-Andaman earthquake of 26 December 2004', Science, 308, pp. 1127-1133.

[13] A. Ghobarah, M. Saatcioglu, I. Nistor, 2006, 'The impact of the 26 December 2004 earthquake and tsunami on structures and infrastructure', Engineering Structures, 28, pp. 312-326.

[14] I.N. Robertson, L. Carden, H.R. Riggs, S. Yim, Y.L. Young, K. Paczkowski, D. Witt, 2010, 'Reconnaissance following the September 29, 2009 tsunami in Samoa', Research Report UHM/CEE10-01, University of Hawaii, Honolulu.

[15] H. Yeh, I.N. Robertson, J. Preuss, 2005, 'Development of design guideline for structures that serve as tsunami vertical evacuation sites.', Washington, Division of Geology and Earth Resources, Report 2005-4.

[16] R.G. Bea, T. Xu, J. Stear, R. Ramos, 1999, 'Wave forces on decks of offshore platforms', Journal of Waterway, Port, Coastal, and Ocean Engineering, ASCE, 125, pp. 136-144.

[17] P. Broughton, E. Horn, 1987, 'Ekofisk Platform 2/4C: re-analysis due to subsidence', Proceeding of Institute of Civil Engineering 1, pp. 949-979

[18] G. Cuomo, M. Tirindelli, W. Allsop, 2007, 'Wave-in-deck loads on exposed jetties', An International Journal for Coastal Harbour and Offshore Engineers, 54, pp. 657-679.

[19] S.L. Douglass, Q. Chen, J.M. Olsen, B.L. Edge, D. Brown, 2006, 'Wave forces on bridge decks', Report for U.S. Department of Transportation, Federal Highway Administration, Office of Bridge Technology.

[20] J.A. French, 1969, 'Wave uplift pressures on horizontal platforms', W.M. Keck Laboratory of Hydraulics and Water Resources, California Institute of Technology, Pasadena, California, USA.

[21] P. Kaplan, 1992, 'Wave impact forces on offshore structures: re-examination and new interpretations', 24th Offshore Technology Conference, Houston, Texas, USA, pp. 79-83.

[22] P. Kaplan, J.J. Murray, W.C. Yu, 1995, 'Theoretical analysis of wave impact forces on platform deck structures', Proceedings of the 14th International Conference on Offshore Mechanics and Arctic Engineering, I-A, pp. 189-198.

[23] R.W.K. Shih, K. Anastasiou, 1992, 'A laboratory study of the wave-induced vertical loading on platform decks', Proceeding of Institution of Civil Engineers, Water, Maritime and Energy, Thomas Telford, London, 96, 1, pp. 19-33.

[24] H. Wang, 1970, 'Water wave pressure on horizontal plate', Journal of the Hydraulics Division, American Society of Civil Engineers, 96, pp. 1997-2017.

[25] H. Árnason, 2004, Interaction between an incident bore and a free-standing coastal structure, Ph.D. dissertation, Department of Civil and Environmental Engineering, University of Washington, Seattle.

[26] FEMA, 2008, 'Guidelines for design of structures for vertical evacuation from tsunamis', FEMA P646, Federal Emergency Management Agency, National Earthquake Hazard Reduction Program.

[27] Y. Fukui, M. Nakamura, H. Shiraishi, Y. Sasaki, 1963, 'Hydraulic study on tsunami', Coastal Engineering in Japan, 6, pp. 67-82.

[28] J.D. Ramsden, 1996, 'Forces on a vertical wall due to long waves, bores, and dry-bed surges', Journal of Waterway, Port, Coastal, and Ocean Engineering, pp. 134-141.

[29] J.D. Ramsden, F. Raichlen, 1990, 'Forces on a vertical wall caused by incident bores', Journal of Waterway, Port, Coastal, and Ocean Engineering, 116, pp. 592-613.

[30] H. Yeh, 2006, 'Maximum fluid forces in the tsunami runup zone', Journal of Waterway, Port, Coastal, and Ocean Engineering, American Society of Civil Engineers, pp. 496-500.

[31] H. Yeh, 2007, 'Design tsunami forces for onshore structures', Journal of Disaster Research, 2, 6 pp.

[32] H.R. Riggs, I. Robertson, K.F. Cheung, G. Pawlak, Y.L. Young, S. Yim, 2008, 'Experimental simulation of tsunami hazards to buildings and bridges', Proceedings of National Science Foundation Engineering Research and Innovation Conference, Knoxville, Tennessee, USA, 8 pp.

[33] OSU, 2008, Oregon State University, O. H. Hinsdale Wave Research Laboratory, http://wave.oregonstate.edu.

[34] P. Kaplan, 1987, 'Analysis and prediction of flat bottom slamming impact of advanced marine vehicles in waves', International Shipbuilding Progress, 34, pp. 44-53.

[35] R.L. McPherson, 2008, Hurricane induced wave and surge forces on bridge decks, Master of Science, Ocean Engineering, Texas A&M University.

[36] AASHTO, 2008, 'Guide specifications for bridges vulnerable to coastal storms', American Association of State Highway and Transportation Officials, Washington, DC.

[37] E.S. Chan, W.K. Melville, 1988, 'Deep-water plunging wave pressures on a vertical plane wall', Proceedings of the Royal Society of London, Series A, Mathematical and Physical Sciences, 417, No. 1852, pp. 95-131.

[38] M.J. Cooker, D.H. Peregrine, 1990, 'Violent water motion at breaking-wave impact', Proceeding of 22nd Coastal Engineering Conference, Delft, Netherlands, pp. 164-176.

[39] D.H. Peregrine, 2003, 'Water-wave impact on walls', Annual Review of Fluid Mechnics, 35, pp. 23-43.

[40] R.H. Cross, 1967, 'Tsunami surge forces', Journal of the Waterways and Harbors Division, Proceedings of the American Society of Civil Engineers, pp. 201–231.

[41] E. Cumberbatch, 1960, 'The impact of a water wedge on a wall', Journal of Fluid Mechanics, 7, pp. 353-373.

[42] R. Asakura, K. Iwase, T. Ikeya, T. Kaneto, N. Fujii, M. Omori, 2000, 'An experiment study on wave force acting on on-shore structures due to overflowing tsunamis', Proc. Coastal Engineering, JSCE, 47, pp. 911-915 (in Japanese).

[43] D.J. Wood, D.H. Peregrine, 1998, 'Two and three-dimensional pressure-impact models of wave impact on structures', Proceeding of Coastal Engineering Conference, Copenhagen, Denmark, pp. 1502-1515.

[44] K. Fujima, F. Achmad, Y. Shigihara, N. Mizutani, 2009, 'Estimation of tsunami force acting on rectangular structures', Journal of Disaster Research, 4, pp. 404-409.

[45] Y. Nouri, I. Nistor, D. Palermo, 2010, 'Experimental investigation of tsunami impact on free standing structures', Coastal Engineering Journal, 52, pp. 43–70.

[46] P. Lukkunaprasit, N. Thanasisathit, H. Yeh, 2009, 'Experimental verification of FEMA P646 tsunami loading', Journal of Disaster Research, 4, pp. 410-418.

[47] NRC, 2004, 'Preventing earthquake disasters: The grand challenge in earthquake engineering: A Research Agenda for the Network for Earthquake Engineering Simulation (NEES)', The National Academies Press, Washington, D.C.

[48] R.B. Haehnel, S.F. Daly, 2002, 'Maximum impact force of woody debris on floodplain structures', US Army Corp of Engineers, Engineer Research and Development Center, Report no. ERDC/CRREL TR-02-2.

[49] R.B. Haehnel, S.F. Daly, 2004, 'Maximum impact force of woody debris on floodplain structures', Journal of Hydraulic Engineering, 130, pp. 112-120.

[50] H. Matsutomi, 2009, 'Method for estimating collision force of driftwood accompanying tsunamiinundation flow', Journal of Disaster Research, 4, pp. 435-440.

[51] G.-S. Yeom, T. Nakamura, N. Mizutani, 2009, 'Collision analysis of container drifted by runup tsunami using drift collision coupled model', Journal of Disaster Research, 4, pp. 441-449.

[52] G.R. Consolazio, R.A. Cook, M.C. McVay, D. Cowan, A. Biggs, L. Bui, 2006, 'Barge impact testing of the St. George Island causeway bridge', University of Florida, Gainesville, FL.

[53] G.R. Consolazio, D.R. Cowan, 2005, 'Numerically efficient dynamic analysis of barge collisions with bridge piers', Journal of Structural Engineering, 131, pp. 1256-1266.

[54] G.R. Consolazio, D.J. Getter, M.T. Davidson, 2009, 'A static analysis method for barge-impact design of bridges with consideration of dynamic amplification', University of Florida, Gainsville, FL.

[55] J.R. Arroyo-Caraballo, R.M. Ebeling, 2006, 'Glancing-blow impact forces by a barge train on a lock approach wall', Journal of Infrastructure Systems, 12, pp. 135-143.

[56] K. Kumagai, K. Oda, N. Fujii, 2006, 'Applicability of simulation model for drift behavior of containers due to tsunami', Techno-Ocean 2006/19th JASNAOE Ocean Engineering Symposium, Kobe, Japan, 6 pp.

[57] N. Mizutani, Y. Takagi, K. Shiraishi, S. Miyajima, T. Tomita, 2005, 'Study on wave force on a container on apron due to tsunamis and collision force of drifted container', Annual Journal of Coastal Engineering, 52, pp. 741-745.

[58] K. Oda, O. Okamoto, K. Kumagai, 2006, ‘Development of estimation method on drift and collision behaviors of debris caused by tsunamis’, 38th joint meeting U.S.-Japan panel on wind and seismic effects, May 15-20, National Institute of Standards and Technology, Gaithersburg, Maryland, USA, 7 pp.

[59] T. Hiraishi, K. Haruo, E. Saitoh, 2010, ‘Experimental study on impulsive force of drift body due to tsunami flow’, Journal of Earthquake and Tsunami, 4, pp. 127-133.

[60] ASCE, 2006, ‘Minimum Design Loads for Buildings and Other Structures: Flood commentary, Chapter C5 (Flood loads)’, American Society of Civil Engineers.

[61] FEMA, 2005, ‘Coastal Construction Manual’, Federal Emergency Management Agency, Washington, D.C.

[62] AASHTO, 2009, ‘Vessel collision design of highway bridges’, American Association of State Highway and Transportation Officials.

[63] USACE, 2004, ‘Barge impact analysis for rigid walls’, USACE, Washington, DC, Report no. ETL 1110-2-563.

[64] A.C.W.M. Vrouwenvelder, 1998, ‘Design for ship impact according to Eurocode 1, Part 2, "Ship collision Analysis"’, pp. 123–134.

[65] Y. Mikhaylov, 2009, Evaluation of prototypical reinforced concrete building performance when subjected to tsunami loading, M.Sc. thesis, Civil and Environmental Engineering, University of Hawaii at Manoa, Honolulu.

[66] W. Goldsmith, 1960, ‘Impact: The theory and physical behaviour of colliding solids’, Edward Arnold (Publishers) Ltd., London.

[67] J. Santo, I.N. Robertson, 2010, Lateral loading on vertical structural elements due to a tsunami bore, M.Sc. thesis, Research Report UHM/CEE/10-02, Civil and Environmental Engineering, University of Hawaii at Manoa, Honolulu.

[68] NEES, 2008, George E. Brown, Jr. Network for Earthquake Engineering Simulation (NEES), a National Science Foundation (NSF) - online data repository, https://nees.org/warehouse/project/624/.

[69] I. Robertson, H.R. Riggs, A. Mohamed, 2008, 'Experimental results of tsunami bore forces on structures', Proceedings of the 27th International Conference on Offshore Mechanics and Arctic Engineering, OMAE2008, June 15-20, Estoril, Portugal, 9 pp.

[70] I. Robertson, K. Paczkowski, H.R. Riggs, A. Mohamed, 2011, 'Tsunami bore forces on walls', Proceedings of the ASME 2011 30th International Conference on Ocean, Offshore and Arctic Engineering, OMAE 2011 June 19-24, 2011, Rotterdam, The Netherlands, 9 pp.

[71] A. Mohamed, 2008, Characterization of tsunami-like bores in support of loading on structures, M.Sc. thesis, Ocean and Resources Engineering, University of Hawaii at Manoa, Honolulu.

[72] G. Cuomo, R. Piscopia, W. Allsop, 2011, 'Evaluation of wave impact loads on caisson breakwaters based on joint probability of impact maxima and rise times', Coastal Engr, 1, pp. 9-27.

[73] S.-C. Hsiao, T.-C. Lin, 2010, 'Tsunami-like solitary waves impinging and overtopping an impermeable seawall: experiment and RANS modeling', Coastal Engineering in Japan, pp. 1–18.

[74] P. Lin, K.-A. Chang, P.L.-F. Liu, 1999, 'Runup and rundown of solitary waves on sloping beaches', Journal of Waterway, Port, Coastal, and Ocean Engineering, pp. 247–255.

[75] S.-C. Hsiao, T.-W. Hsu, T.-C. Lin, Y.-H. Chang, 2008, 'On the evolution and run-up of breaking solitary waves on a mild sloping beach', Coastal Engineering, pp. 975–988.

[76] I. Nistor, D. Palermo, A. Cornett, T. Al-Faesly, 2010, 'Experimental and numerical modeling of tsunami loading on structures', Proceedings of the International Conference on Coastal Engineering. No. 32, pp. 1-14.

[77] H.T.C. Pedro, K.-W. Leung, M.H. Kobayashi, H.R. Riggs, 2007, 'Numerical study of the wave impact on a square column using large eddy simulation.', Proceedings of the 26th International Conference on Offshore Mechanics and Arctic Engineering, OMAE2007, June 10-15, 2007, San Diego, California, USA, 7 pp.

[78] W.P. Jones, L.B. E., 1973, 'The calculation of low-Reynolds-number-phenomena with a two- equation model of turbulence', International Journal of Heat and Mass Transfer, 16, pp. 1119-1130.

[79] B.E. Launder, B.I. Sharma, 1974, 'Application of energy-dissipation model of turbulence to the calculation of flow near a spinning disc', Letters in Heat and Mass Transfer, pp. 131-138.

[80] V. Yakhot, Orszag, S.A., Thangam, S., Gatski, T.B. & Speziale, C.G., 1992, 'Development of turbulence models for shear flows by a double expansion technique', Physics of Fluids A: Fluid dynamics, 4, pp. 1510-1520.

[81] F.R. Menter, 1992, 'Improved two-equation k-w turbulence models for aerodynamic flows', NASA Technical Memorandum 103975.

[82] F.R. Menter, 1993, 'Zonal two equation k-w turbulence models for aerodynamic flows', AIAA Paper No. 93-2906, 24th Fluid Dynamics Conference.

[83] Fluent, http://www.ansys.com/products/fluid-dynamics/fluent/.

[84] OpenFOAM, http://www.openfoam.org.

[85] D.G. Goring, F. Raichlen, 1980, 'The generation of long waves in the laboratory', Proc. of the 17th International Conference of Coastal Engineers, pp. 763-784.

[86] J.J. Stoker, 1957, 'Pure and applied mathematics.', Interscience Publisher, INC.

[87] S. Hughes, 1993, 'Physical models and laboratory techniques in coastal engineering', World Scientific Publishing Ltd., Singapore.

[88] A. Horvath, C. Jordan, M. Lukasser, C. Kuttner, A. Makaruk, M. Harasek, 2009, 'CFD simulation of bubble columns using the VOF model: comparison of commercial and open source solvers with an experiment', Chemical Engineering Transactions, 18, 6 pp.

[89] V. Roeber, K.F. Cheung, H.M. Kobayashi, 2010, 'Shock-capturing Boussinesq\-type model for nearshore wave processes', Coastal Engineering, pp. 407–423.

[90] MTS, 1974, 'Product specification: Model-series 661.2X and 661.3X, fatigue resistant load cells', MTS Systems Corp., 8 pp.

[91] G. Szuladzinski, 2010, 'Formulas for mechanical and structural shock and impact', CRC Press, Taylor & Francis Group, Boca Raton, Florida.

[92] S.K. Clark, 1972, 'Dynamics of continuous elements', Prentice-Hall, Inc., Englewood Cliffs, New Jersey.

[93] R.W. Clough, J. Penzien, 1993, 'Dynamics of structures', Second edition ed., McGraw-Hill Inc., Unitied States of America.

[94] W. Johnson, 1972, 'Impact Strength of Materials', Edward Arnold, London.

[95] K. Paczkowski, H.R. Riggs, C.J. Naito, A. Lehman, 2011, 'A one-dimensional model for impact forces resulting from high mass, low velocity debris', International Journal of Impact Engineering (in preparation), 16 pp.

[96] H.M. Kobayashi, H.R. Riggs, R. Genest, K. Paczkowski, 2011, 'Hydroelastic impact models for water-borne debris', Journal of Engineering for the Maritime Environment (submitted), 22 pp.

Appendix A

In this section, the results for projectile impact upon steel load cell from Chapter 5 are presented. The results are for four projectile lengths: 1, 2, 3, and 4 m. In the figures, the naming convention is defined as follows: P stands for 'projectile' and the first digit after the projectile defines its length, i.e. P1 stands for 1m long projectile. The following number defines number of used strain sensors, i.e. P1_2 stands for 1m long projectile with two strain sensors. The last digid defines the trial number, i.e. P1_2_1 stands for 1m long projectile with two strain sensors, trial 1.

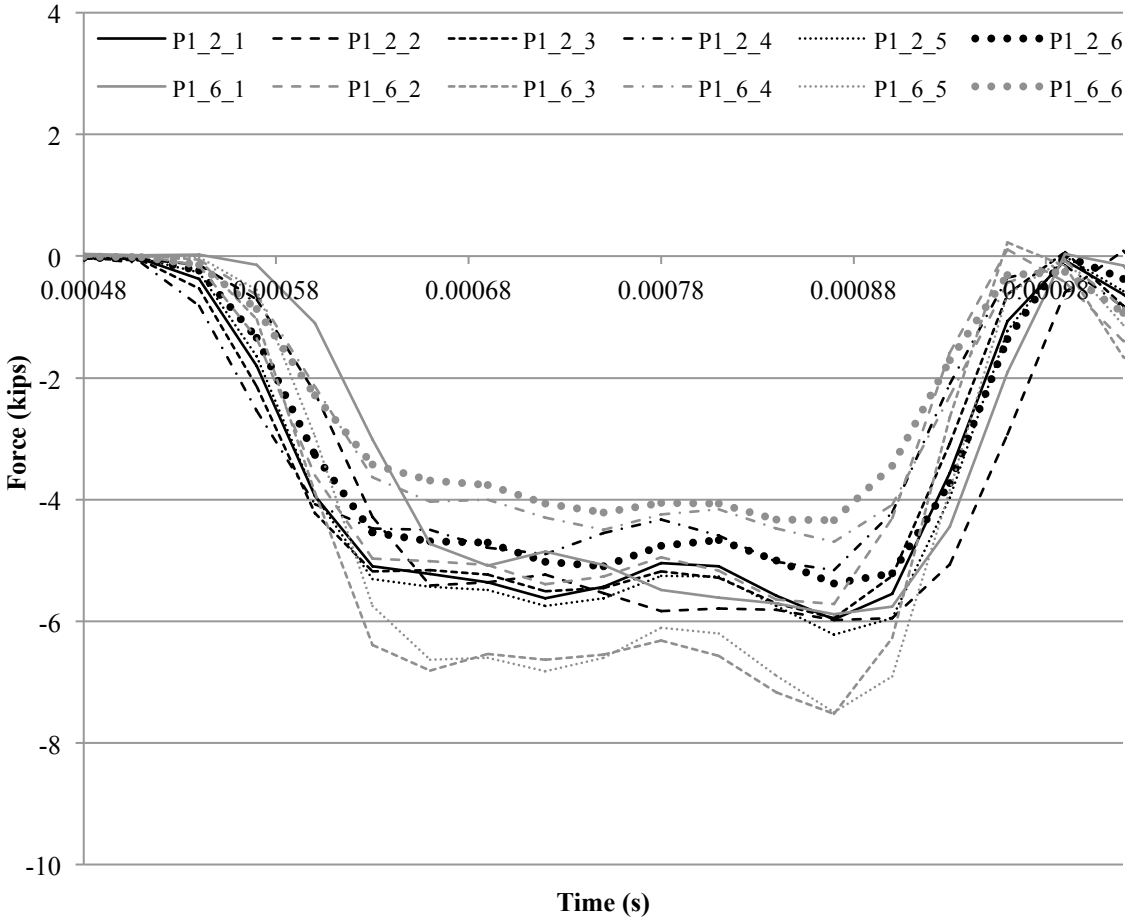

A. 1. Debris impact load-cell force time histories for; 1 m long projectile.

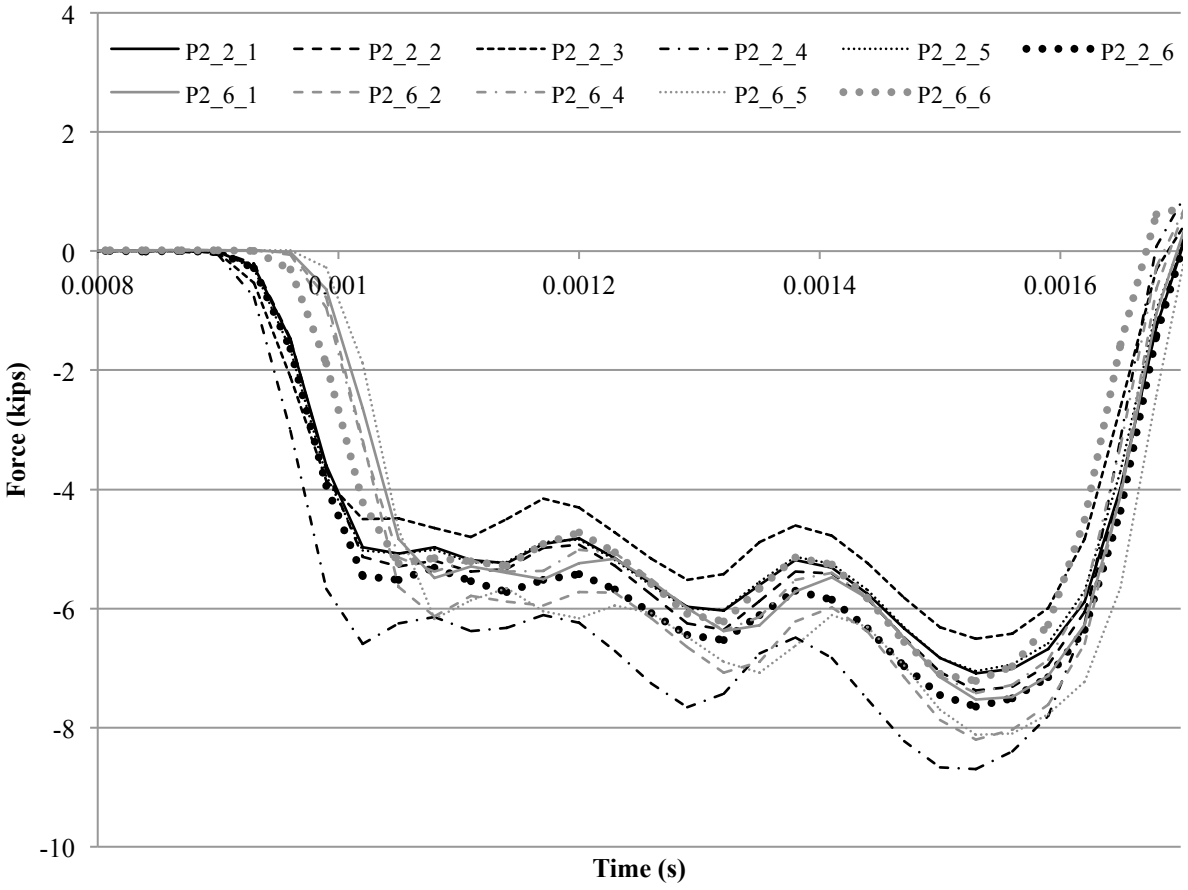

A. 2. Debris impact load-cell force time histories; 2 m long projectile.

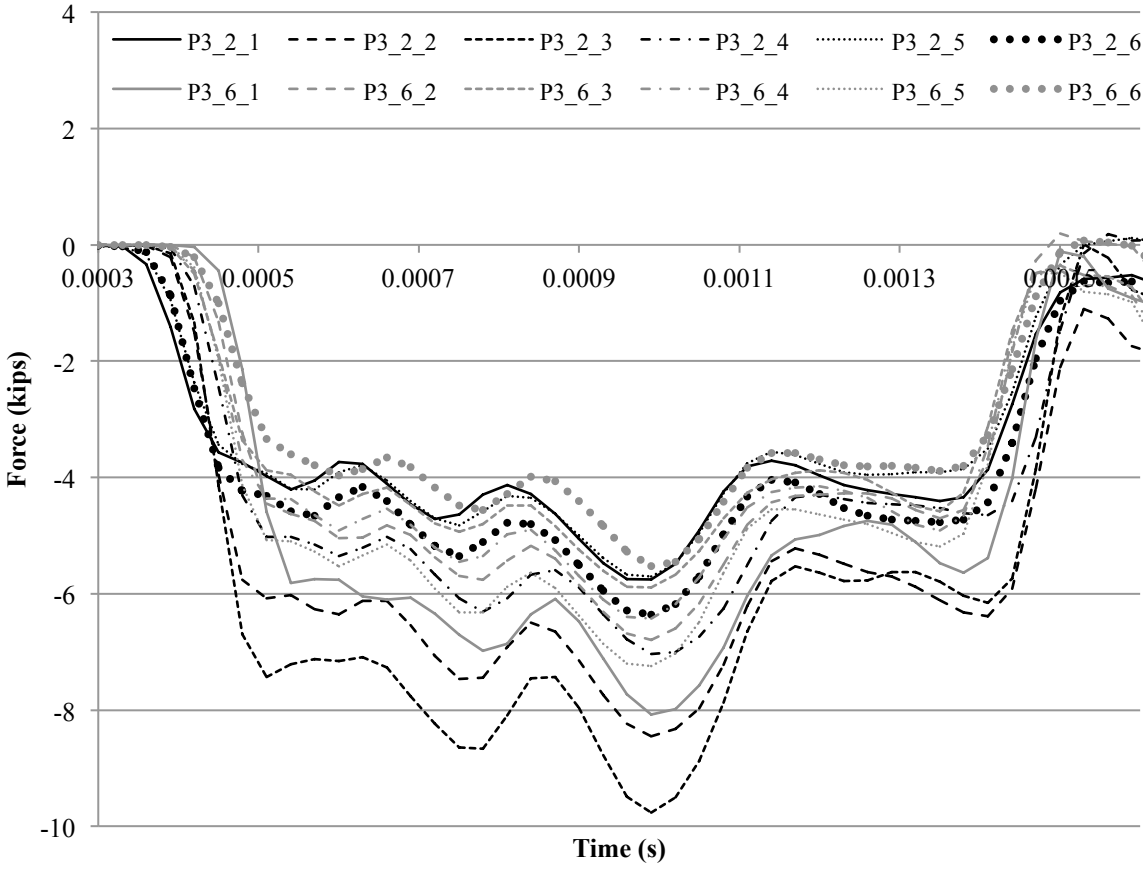

A. 3. Debris impact load-cell force time histories; 3 m long projectile.

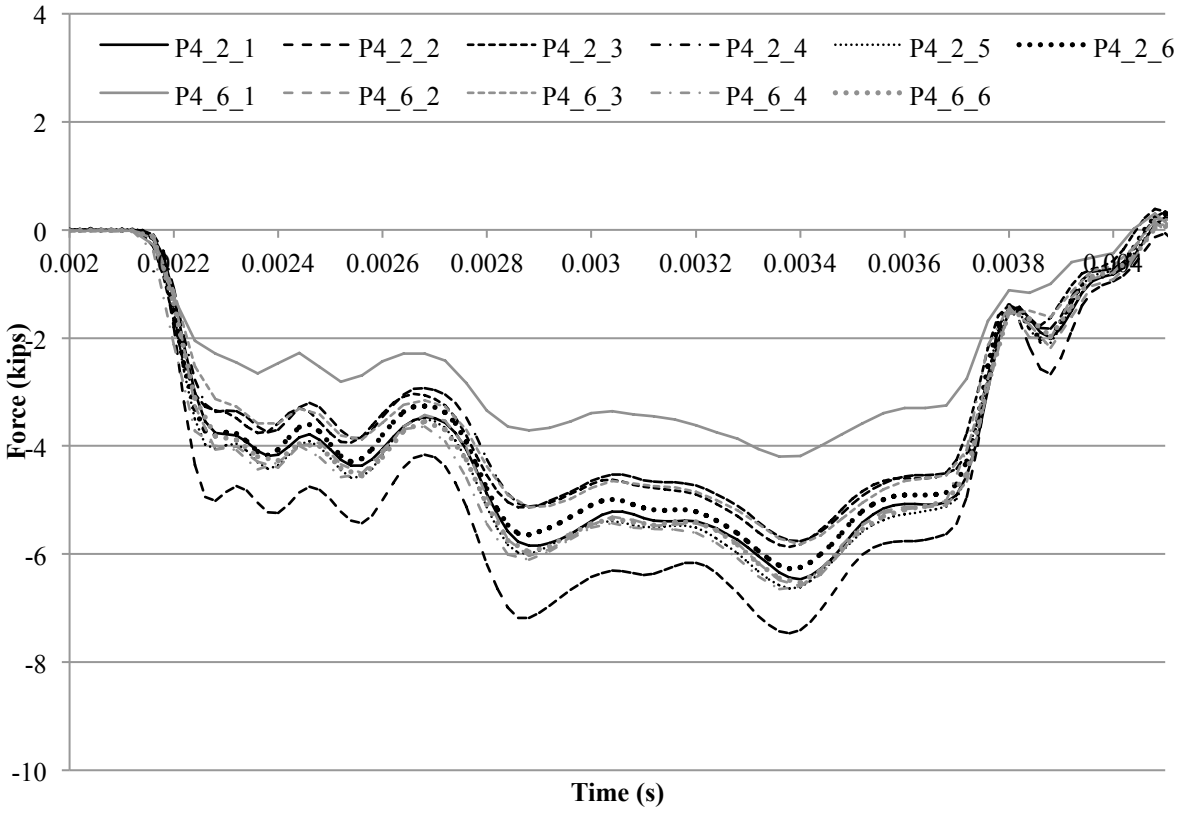

A. 4. Debris impact load-cell force time histories; 4 m long projectile.

Appendix B

The strain gauges were placed at three sections on both sides of each of the projectiles. There were two end sections (5 cm from the end of the each tube) and one section right in the middle. The setup involved overall number of six strain sensors. To increase the data acquisition frequency, additional trails were run which involved only two strain sensors at the end section closest to the impact surface. The strain gauges were numbered starting from the face of the impact tube. Facing the front tube surface, the numbering of strain gauges started from the left side of the tube. Hence, first section included strain gauges numbered as 1 and 2, mid section included 3 and 4, and very end section included strain sensors numbered 5 and 6. For each of the projectiles the runs were repeated at least three times. For brevity of results the trials were run six times for each of the projectiles with exception of few trials in which recording failed due to some technical difficulties. At first, the time histories for 2 strain sensors are presented followed by results for 6 strain sensors. In some of the cases not all the strain sensor plots are shown. Whenever plot is missing, it means the strain measurement was not good. Note that the vertical scales differ to increase the clarity of the plots.

1 m long projectile with 2 strain sensors

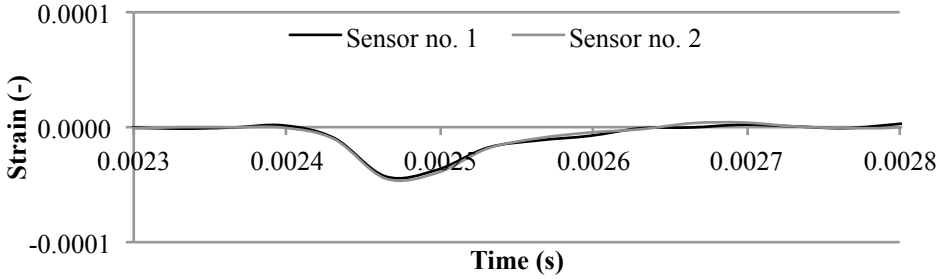

B. 1. Projectile strain time-history; 1 m long projectile, 2 strain sensors, Trial 1.

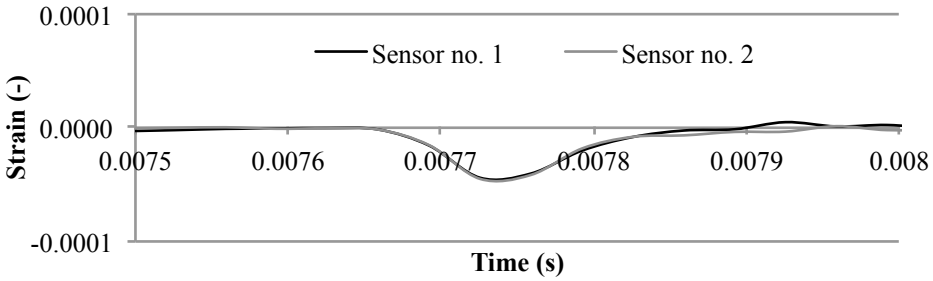

B. 2. Projectile strain time-history; 1 m long projectile, 2 strain sensors, Trial 2.

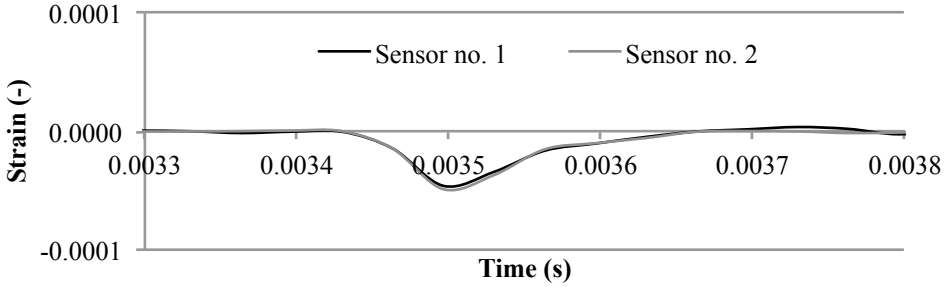

B. 3. Projectile strain time-history; 1 m long projectile, 2 strain sensors, Trial 3.

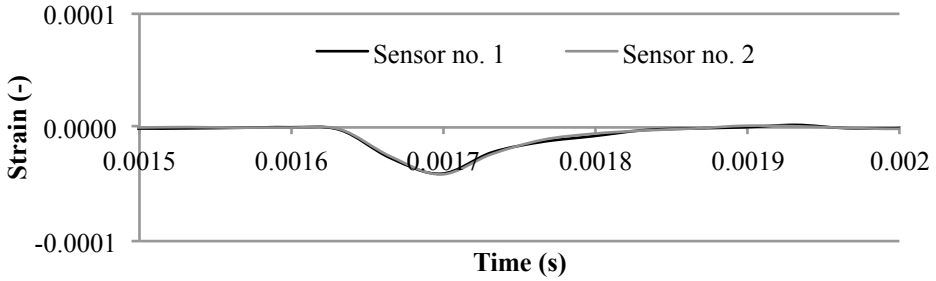

B. 4. Projectile strain time-history; 1 m long projectile, 2 strain sensors, Trial 4.

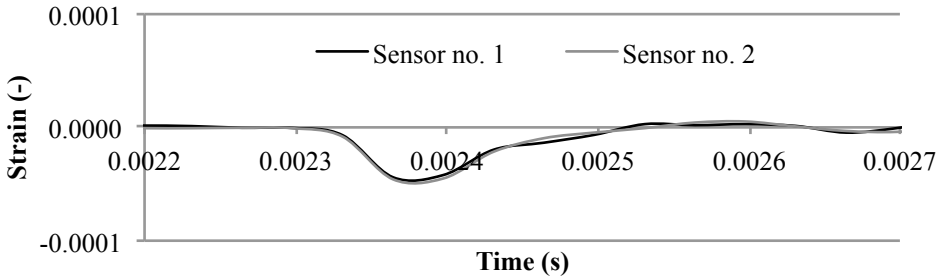

B. 5. Projectile strain time-history; 1 m long projectile, 2 strain sensors, Trial 5.

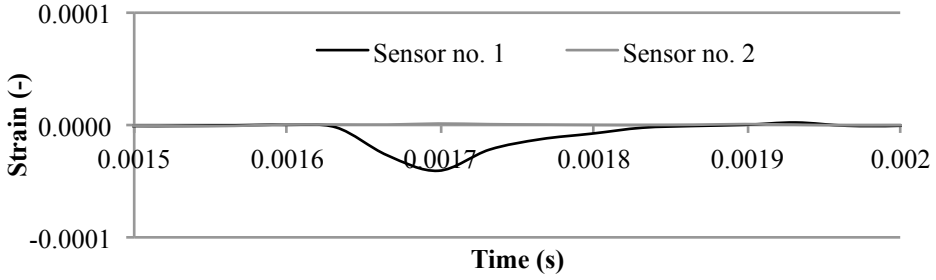

B. 6. Projectile strain time-history; 1 m long projectile, 2 strain sensors, Trial 6.

1 m long projectile with 6 strain sensors

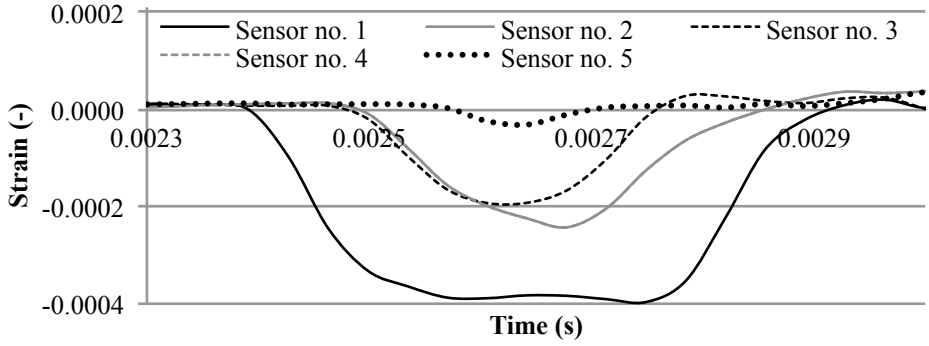

B. 7. Projectile strain time-history; 1 m long projectile, 6 strain sensors, Trial 1.

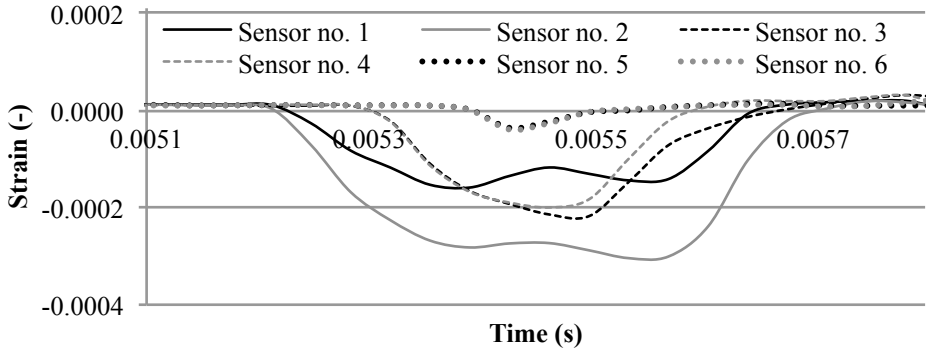

B. 8. Projectile strain time-history; 1 m long projectile, 6 strain sensors, Trial 2.

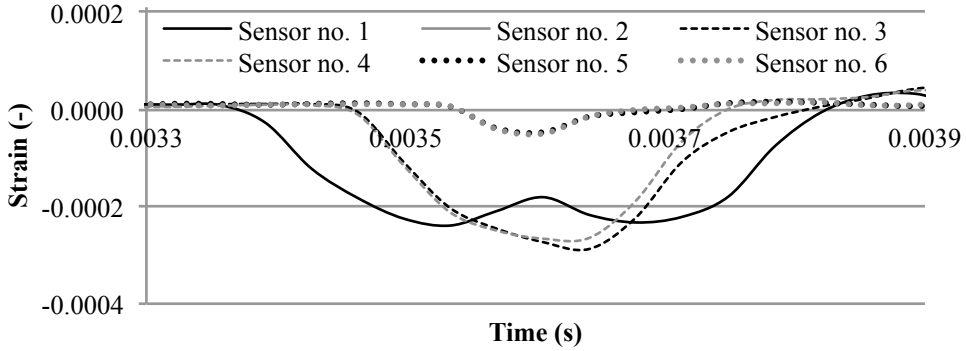

B. 9. Projectile strain time-history; 1 m long projectile, 6 strain sensors, Trial 3.

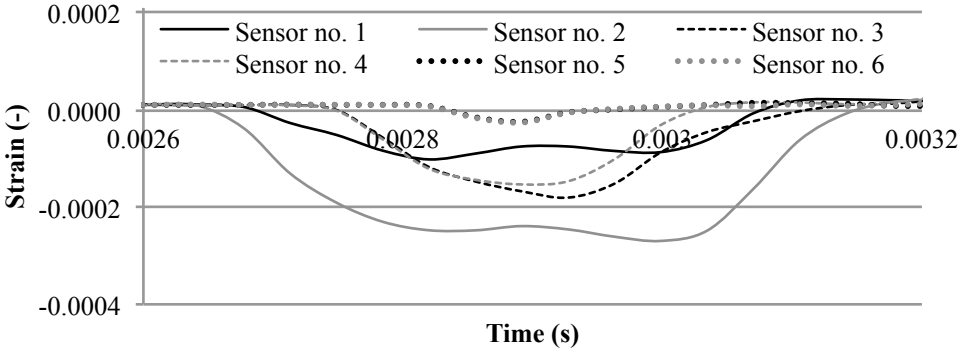

B. 10. Projectile strain time-history; 1 m long projectile, 6 strain sensors, Trial 4.

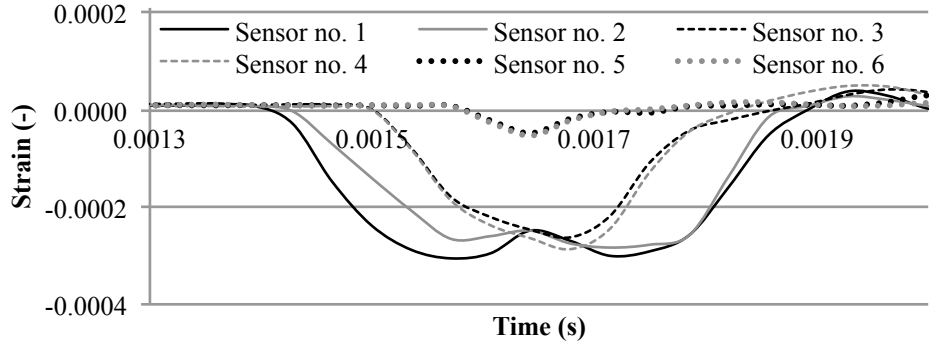

B. 11. Projectile strain time-history; 1 m long projectile, 6 strain sensors, Trial 5.

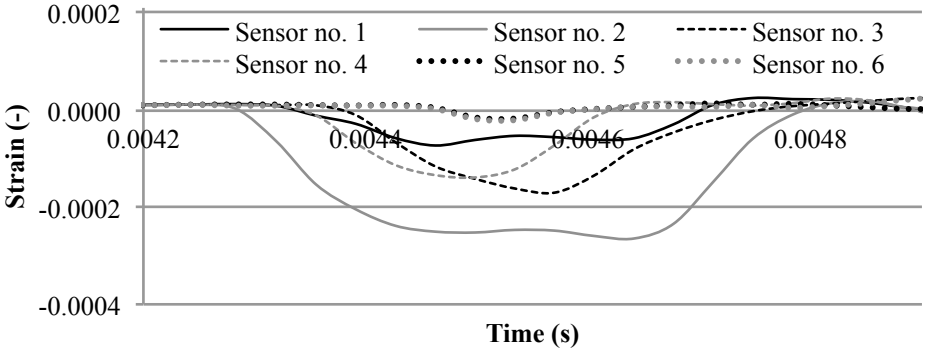

B. 12. Projectile strain time-history; 1 m long projectile, 6 strain sensors, Trial 6.

2 m long projectile with 2 strain sensors

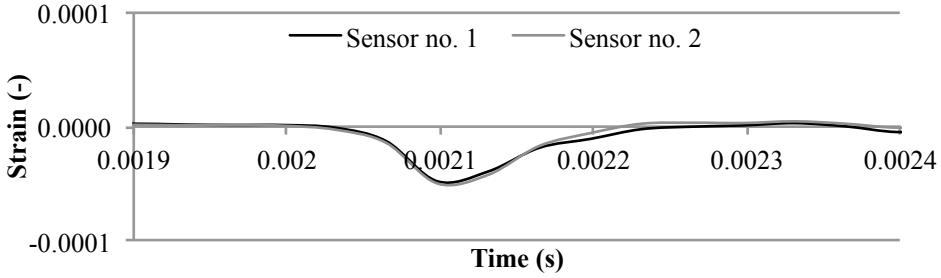

B. 13. Projectile strain time-history; 2 m long projectile, 2 strain sensors, Trial 1.

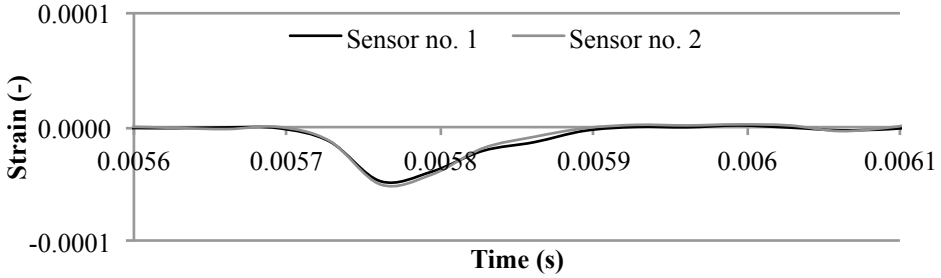

B. 14. Projectile strain time-history; 2 m long projectile, 2 strain sensors, Trial 2.

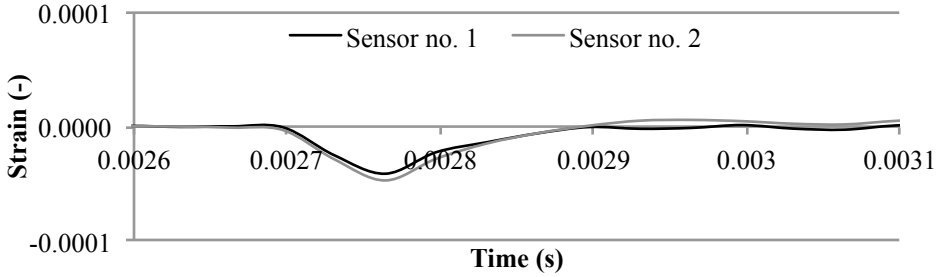

B. 15. Projectile strain time-history; 2 m long projectile, 2 strain sensors, Trial 3.

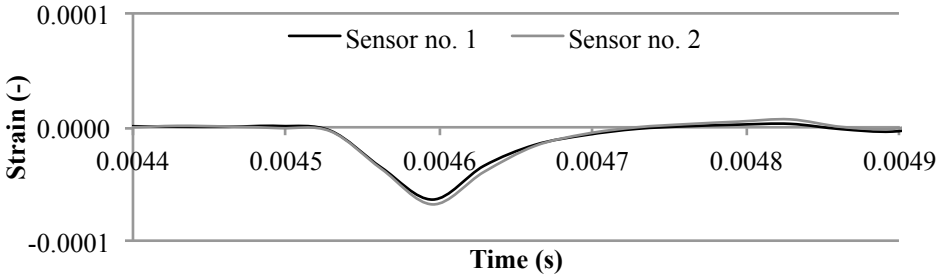

B. 16. Projectile strain time-history; 2 m long projectile, 2 strain sensors, Trial 4.

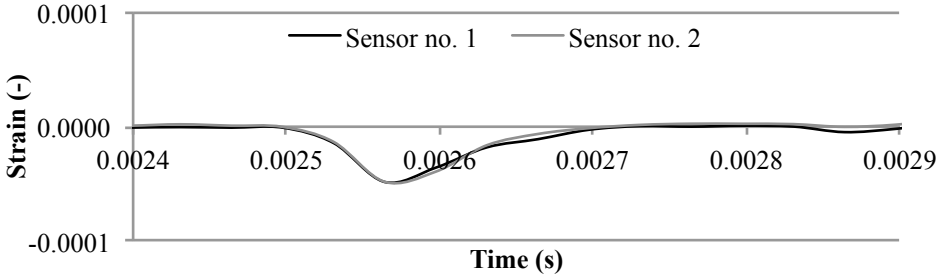

B. 17. Projectile strain time-history; 2 m long projectile, 2 strain sensors, Trial 5.

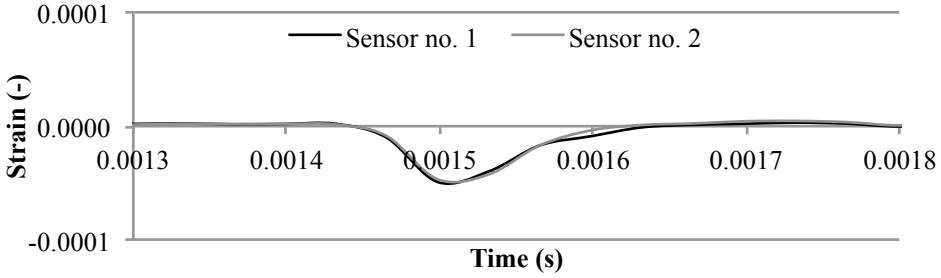

B. 18. Projectile strain time-history; 2 m long projectile, 2 strain sensors, Trial 6.

2 m long projectile with 6 strain sensors

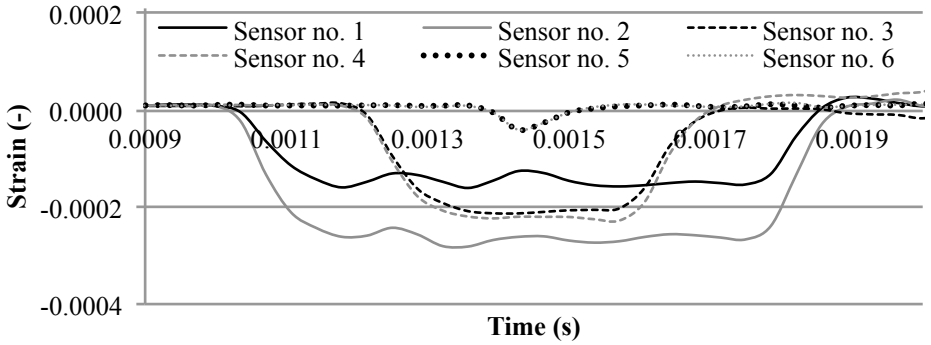

B. 19. Projectile strain time-history; 2 m long projectile, 6 strain sensors, Trial 1.

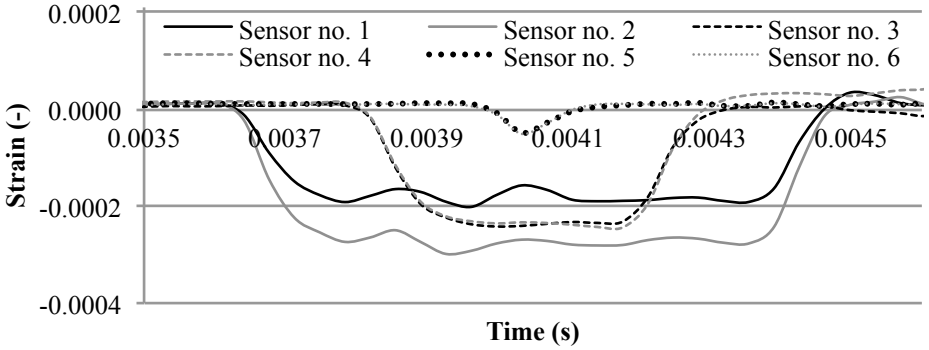

B. 20. Projectile strain time-history; 2 m long projectile, 6 strain sensors, Trial 2.

Trial 3 record experienced some technical difficulties. Data is not presented.

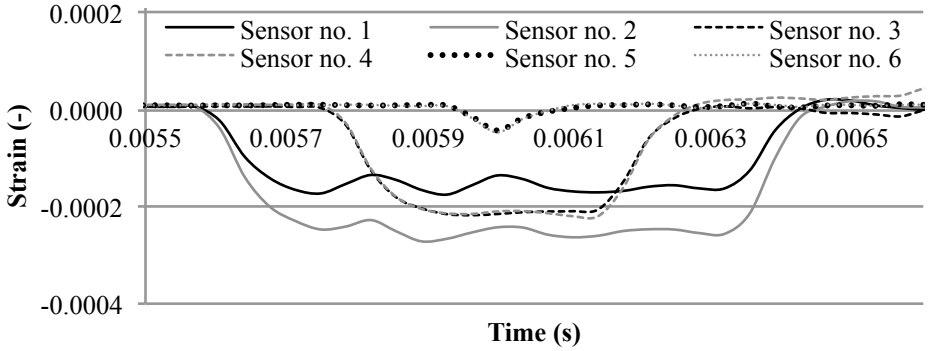

B. 21. Projectile strain time-history; 2 m long projectile, 6 strain sensors, Trial 4.

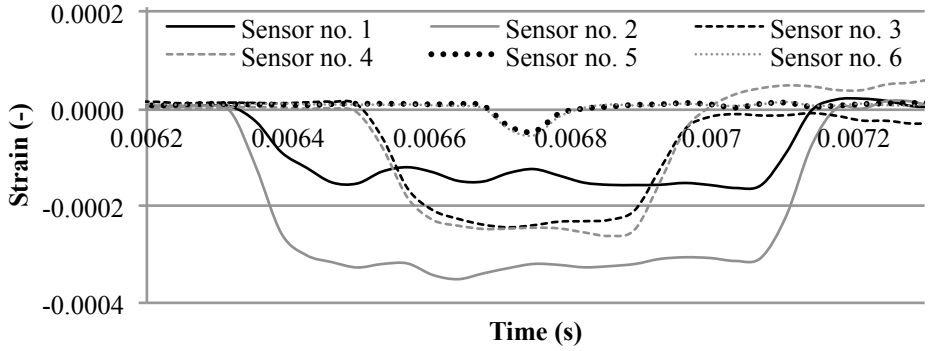

B. 22. Projectile strain time-history; 2 m long projectile, 6 strain sensors, Trial 5.

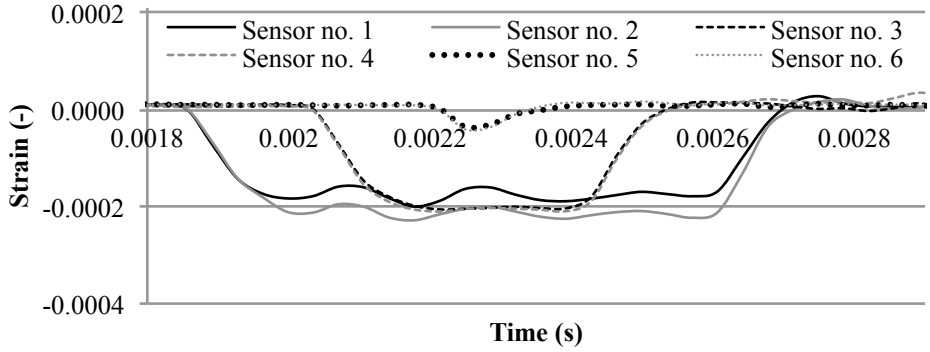

B. 23. Projectile strain time-history; 2 m long projectile, 6 strain sensors, Trial 6.

3 m long projectile with 2 strain sensors

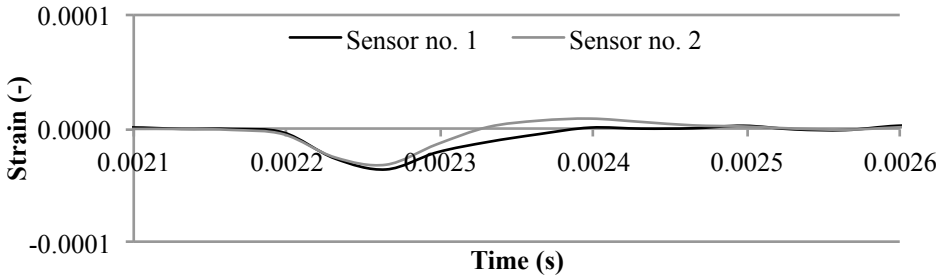

B. 24. Projectile strain time-history; 3 m long projectile, 2 strain sensors, Trial 1.

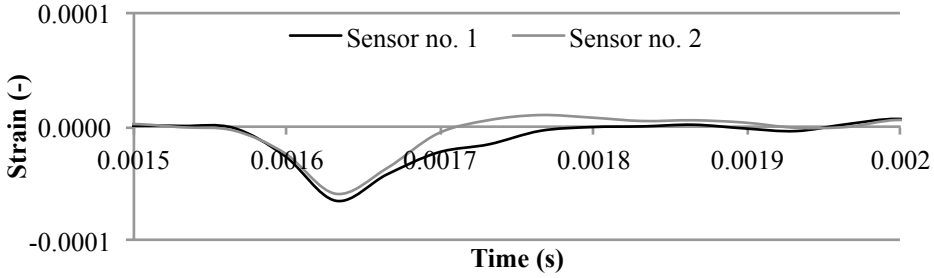

B. 25. Projectile strain time-history; 3 m long projectile, 2 strain sensors, Trial 2.

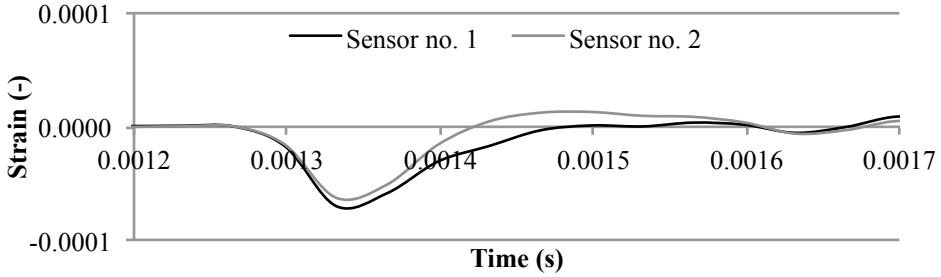

B. 26. Projectile strain time-history; 3 m long projectile, 2 strain sensors, Trial 3.

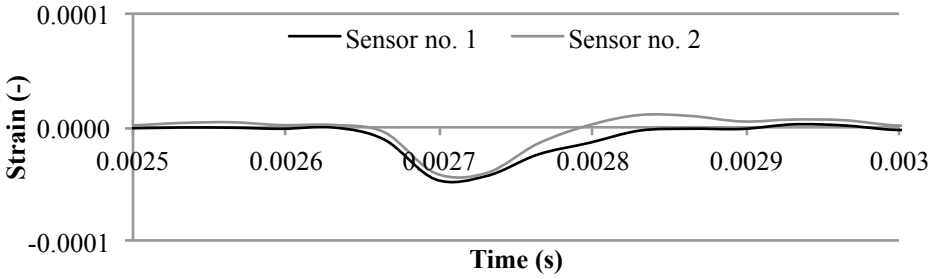

B. 27. Projectile strain time-history; 3 m long projectile, 2 strain sensors, Trial 4.

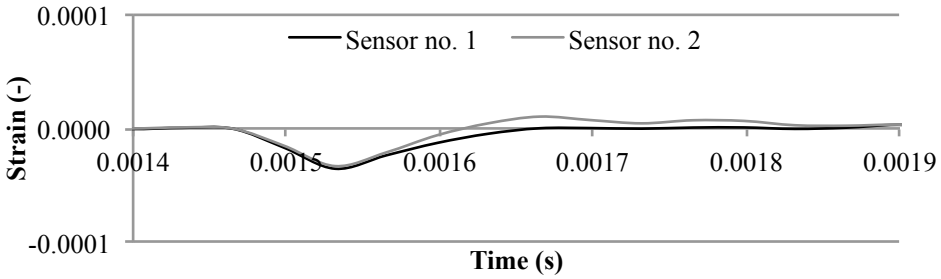

B. 28. Projectile strain time-history; 3 m long projectile, 2 strain sensors, Trial 5.

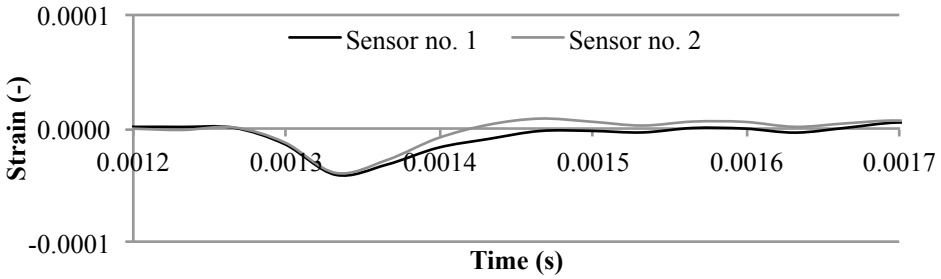

B. 29. Projectile strain time-history; 3 m long projectile, 2 strain sensors, Trial 6.

3 m long projectile with 6 strain sensors

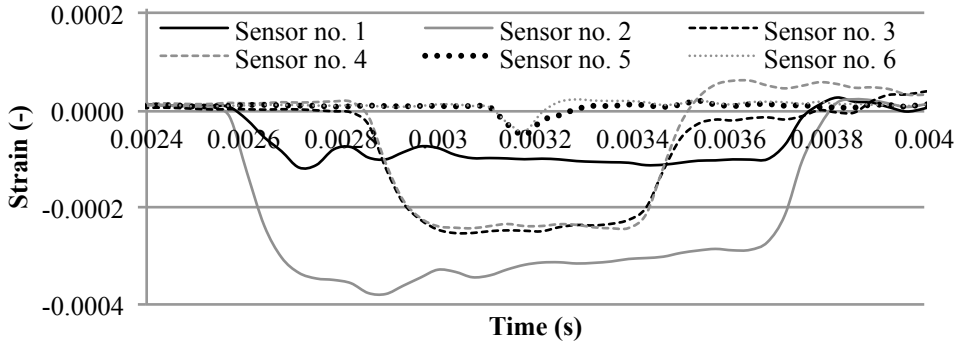

B. 30. Projectile strain time-history; 3 m long projectile, 6 strain sensors, Trial 1.

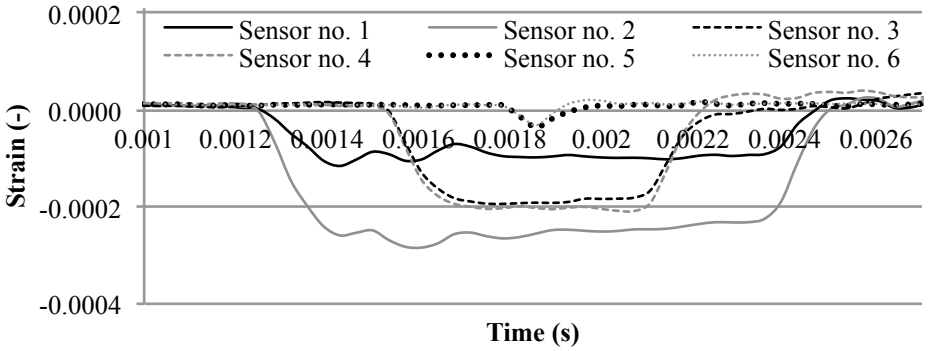

B. 31. Projectile strain time-history; 3 m long projectile, 6 strain sensors, Trial 2.

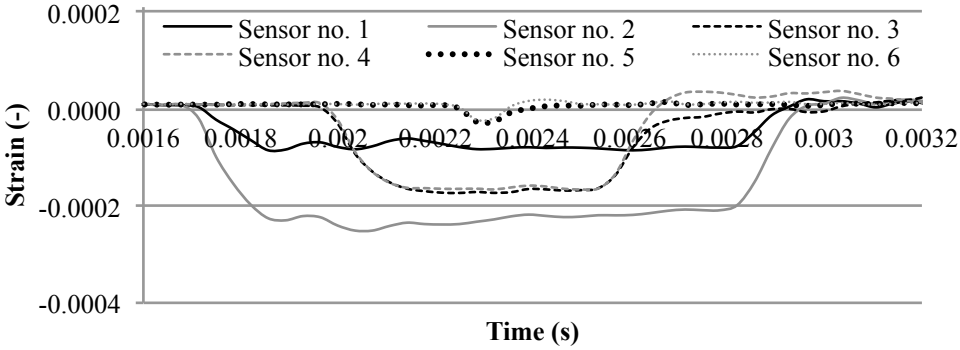

B. 32. Projectile strain time-history; 3 m long projectile, 6 strain sensors, Trial 3.

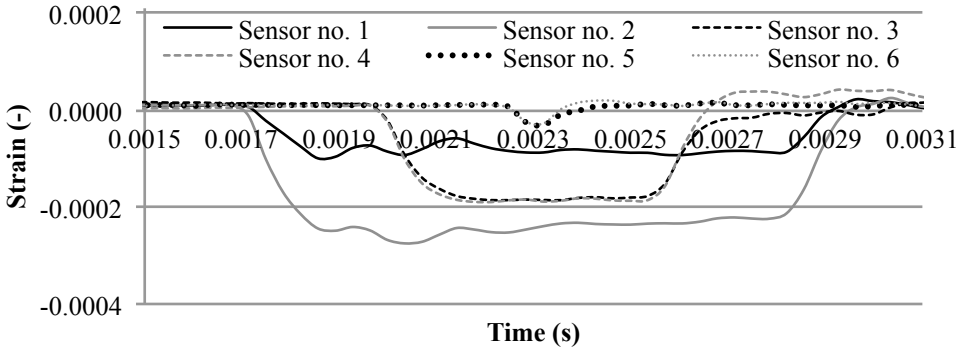

B. 33. Projectile strain time-history; 3 m long projectile, 6 strain sensors, Trial 4.

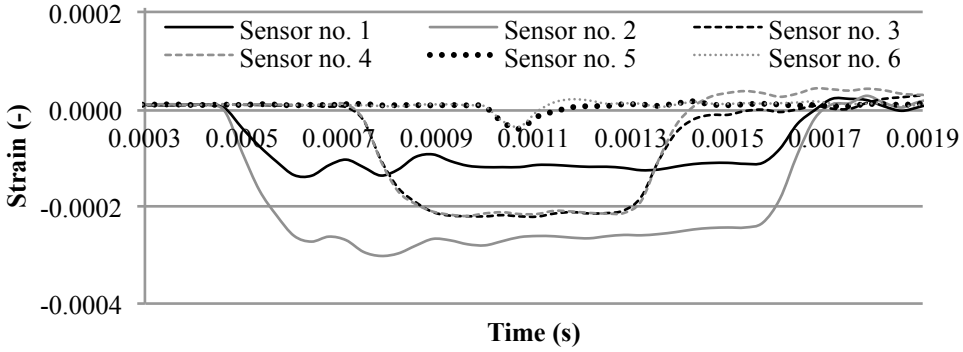

B. 34. Projectile strain time-history; 3 m long projectile, 6 strain sensors, Trial 5.

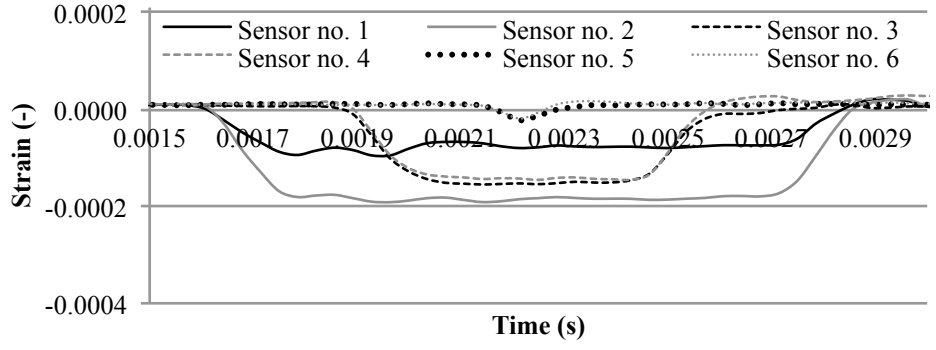

B. 35. Projectile strain time-history; 3 m long projectile, 6 strain sensors, Trial 6.

4 m long projectile with 2 strain sensors

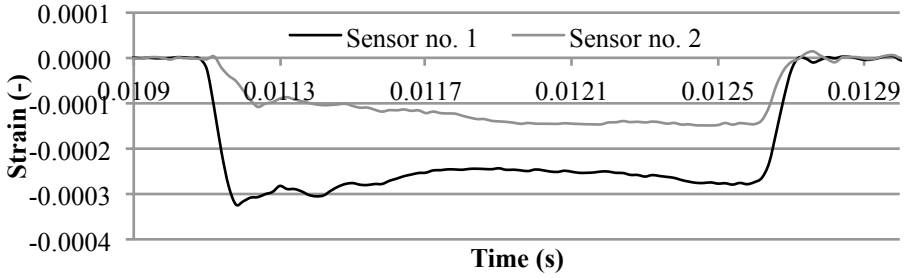

B. 36. Projectile strain time-history; 4 m long projectile, 2 strain sensors, Trial 1.

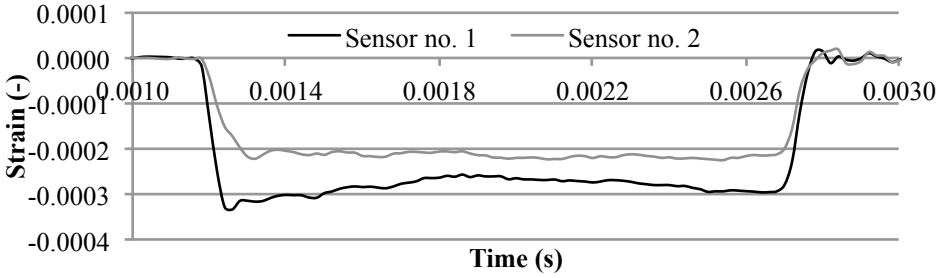

B. 37. Projectile strain time-history; 4 m long projectile, 2 strain sensors, Trial 2.

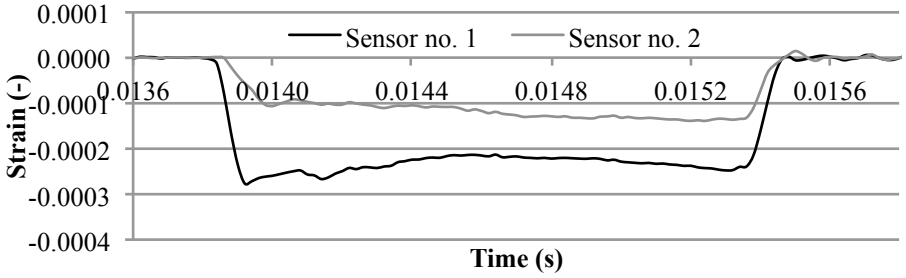

B. 38. Projectile strain time-history; 4 m long projectile, 2 strain sensors, Trial 3.

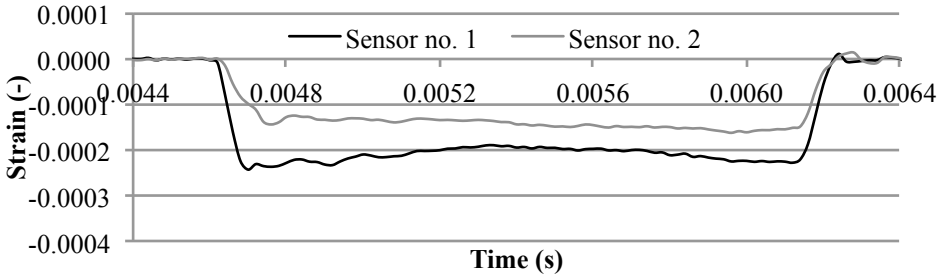

B. 39. Projectile strain time-history; 4 m long projectile, 2 strain sensors, Trial 4.

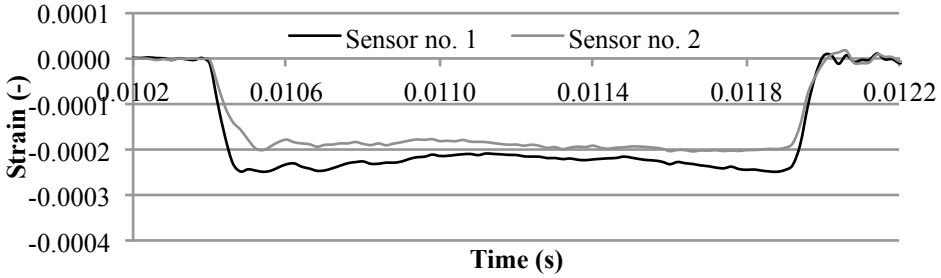

B. 40. Projectile strain time-history; 4 m long projectile, 2 strain sensors, Trial 5.

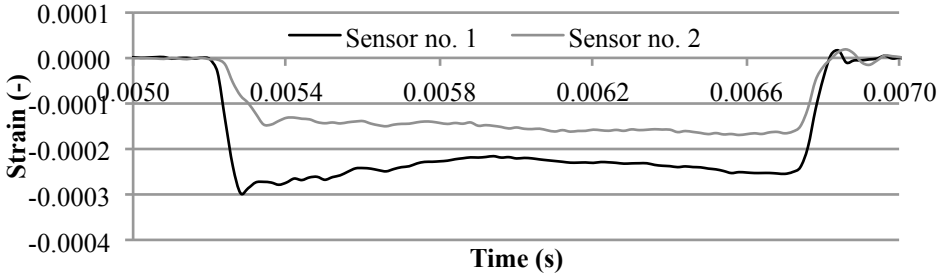

B. 41. Projectile strain time-history; 4 m long projectile, 2 strain sensors, Trial 6.

4 m long projectile with 6 strain sensors

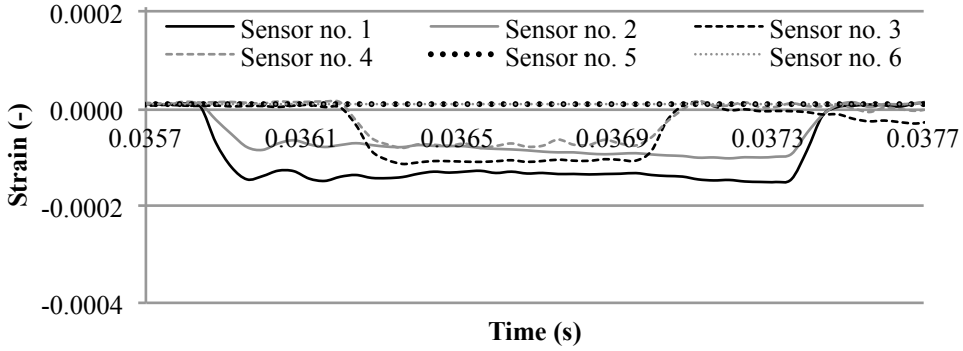

B. 42. Projectile strain time-history; 4 m long projectile, 6 strain sensors, Trial 1.

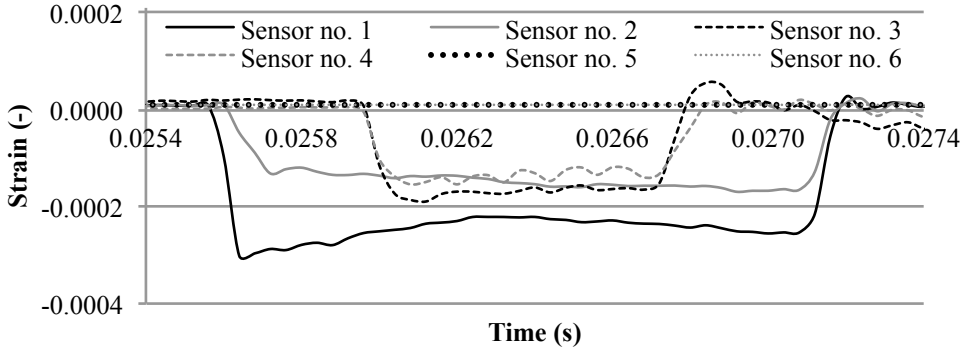

B. 43. Projectile strain time-history; 4 m long projectile, 6 strain sensors, Trial 2.

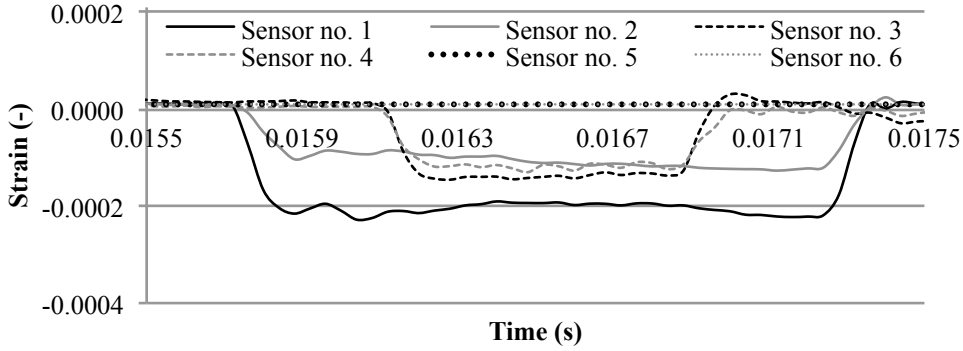

B. 44. Projectile strain time-history; 4 m long projectile, 6 strain sensors, Trial 3.

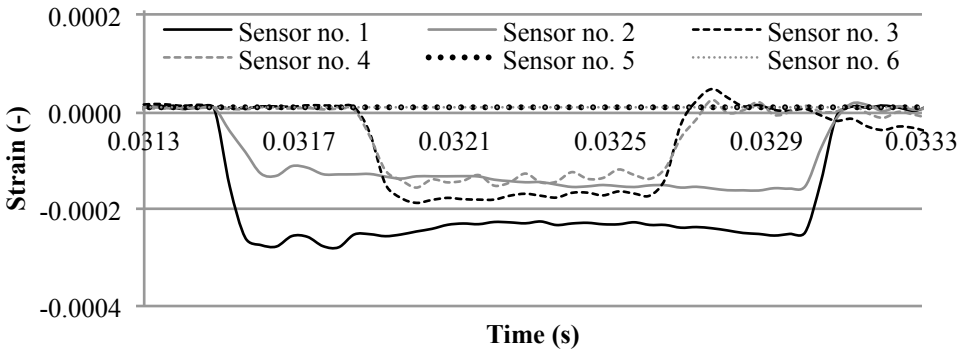

B. 45. Projectile strain time-history; 4 m long projectile, 6 strain sensors, Trial 4.

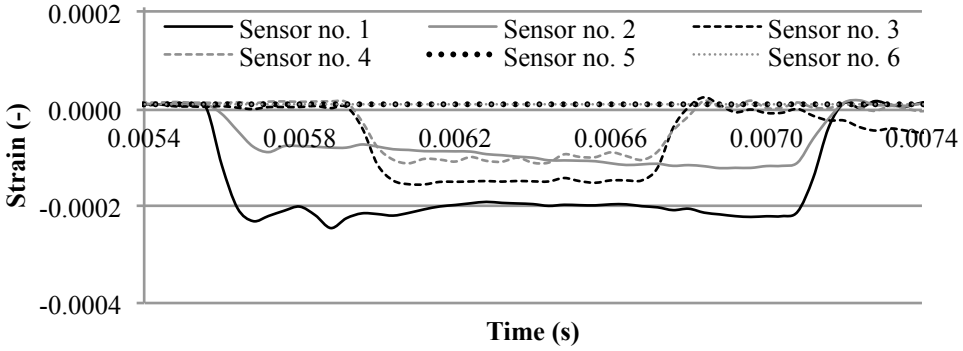

B. 46. Projectile strain time-history; 4 m long projectile, 6 strain sensors, Trial 5.

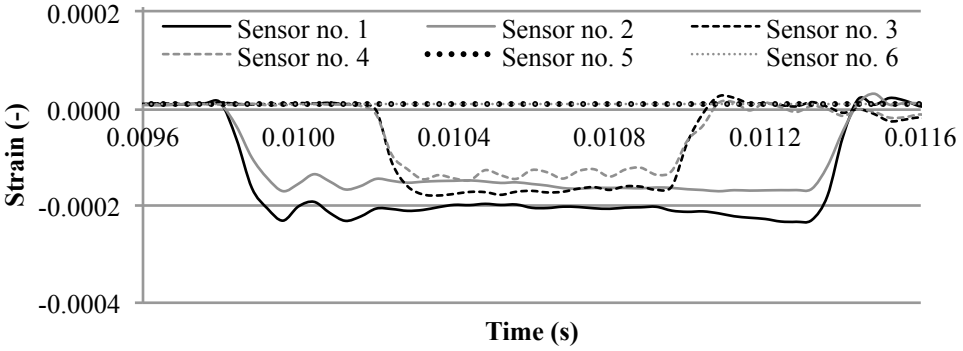

B. 47. Projectile strain time-history; 4 m long projectile, 6 strain sensors, Trial 6.